TECTONIC EVOLUTION OF THE LABYRINTH MOUNTAIN AREA, CASCADES CRYSTALLINE CORE, WASHINGTON: UNRAVELING INTERTWINED DEFORMATION, INTRUSION AND METAMORPHISM

by

GERRIT RIJK BULMAN

A THESIS

Submitted in partial fulfillment of the requirements for the
degree of Master of Science in the Department
of Geological Sciences in the Graduate School
of The University of Alabama

TUSCALOOSA, ALABAMA

2005

SDC
OE
LD
.B35
2005

Submitted by Gerrit Rijk Bulman in partial fulfillment of the requirements for the degree of Master of Science specializing in Geology.

Accepted on behalf of the Faculty of the Graduate School by the thesis committee:

[redacted]

Harold H. Stowell, Ph.D.
Chairperson

[redacted]

Nathan L. Green, Ph.D.

[redacted]

Douglas K. Tinkham, Ph.D.

[redacted]

Rona J. Donahoe, Ph.D.

[redacted]

Harold H. Stowell, Ph.D.
Department Chairperson

Oct 21 2005
Date

[redacted]

Ronald W. Rogers, Ph.D.
Dean of the Graduate School

12/6/05
Date

ACKNOWLEDGEMENTS

I wish to first acknowledge what is so often overlooked in scientific publications—that the perceived contribution of a work does not reflect the distribution one's efforts. If my efforts were proportional to the significance of the results, this thesis would focus on the finer points of calibrating Sm-Nd separation columns. That said, for guidance, patience, ready availability, encouragement, latitude, humor and friendship, I wish to thank Professor Harold Stowell.

For teaching me petrography, phase equilibria, lab techniques and humility on the trail, I thank Dr. Carlos Zuluaga. I wish to thank Dr. Doug Tinkham for introducing me to the Labyrinth Mountain area, for conveying his enthusiasm about the project and for helping me focus my research questions. Dr. Bob Miller, Dr. Scott Paterson, Ellen Stein, Dr. Delores Robinson, Dr. Rick Groshong, Dr. Geoff Tick and Dr. Andy Goodliffe each provided encouragement, advice and direction through numerous discussions. Many thanks to Dr. George Gehrels (University of Arizona) and to Dr. Drew Coleman (UNC Chapel Hill) for geochronologic analyses. Dr. Staci Loewy spent a week patiently teaching me how to run a thermal ionization mass spectrometer. And thanks to Betsy Graham for many helpful discussions on laboratory techniques and for taking time in the early mornings and on Saturdays to run calibration standards on the ICP-MS.

I wish to thank Dr. Bernard Evans for providing the petrology group with a wealth of data and samples from the Cascades—and his student, Gary Davidson, for leaving copious field notes. For field assistance, thanks to Cynthia Strickland, and for

pertrography assistance, thanks to Jeff Edelen. For field assistance and valuable discussions of structure, magmatism and U-Pb geochronology, I wish to thanks my good friend Joshua Schwartz. Dr. Nathan Green sparked my interest in garnet REE chemistry, inclusions and leaching experiments. Dr. Rona Donahoe provided an unbiased check on the expectations for my research plan and thesis, as well as a close reading of the final product. I wish to also acknowledge several of my peers—Ben García, Gang Wang, Michael Rasbury, Ryan Faerber and Sandy Keller—for technical assistance, five-minute refresher courses and empathy. This work would not have been possible without the continual technical and administrative support of Jim Donahoe, Betty Fagan, Debbie Frank, Pat Smith and Diane Norris.

For encouragement and for the occasional spur, I thank my loving wife Maura.

I wish to recognize generous financial support from the University of Alabama Department of Geological Sciences, the Geological Sciences Advisory Board (GSAB), the University of Alabama Graduate Council, the W. Gary Hooks Fund, the Johnson Fund for student travel, Amoco Oil Research Fund, the Geological Society of America, the Southeastern Section of the Geological Society of America, and the Cordilleran Section of the Geological Society of America.

This work is dedicated to two geologists without whom I'd not have experienced the past twenty years in the same way, two whose enthusiasm about geology and the outdoors I've been vividly reminded of while looking out from Jamaica's Blue Mountain peak, climbing in the basement of the Grand Canyon, resting on a Piedmont ridge and traversing glacial cirques in the Washington Cascades: Bob Schwartz and the late Wayne Brewer.

CONTENTS

ACKNOWLEDGEMENTS iii

LIST OF TABLES vii

LIST OF FIGURES viii

ABSTRACT x

I. INTRODUCTION 1

Tectonic Models 4

Geologic Setting 11

Integrated Geochronology-Petrology-Structural Geology 14

II. METHODS 22

Structural Analyses 22

Petrology 25

Sm-Nd Garnet Geochronology 29

U-Pb Zircon Geochronology 33

III. THE LABYRINTH MOUNTAIN PLUTON 35

Timing 42

Origin 42

IV. DEFORMATION AND MAGMA EMPLACEMENT 51

Fanning foliation 51

A magma emplacement model 60

The Nason Ridge Migmatitic Gneiss 70

Minotaur Lake Fault 79

V. METAMORPHISM 87

Isograds and metamorphic textures 87

Thermodynamic modeling 93

Timing of Garnet Growth 94

VI. DISCUSSION 104

Evaluating Tectonics Models 104

REFERENCES 111

APPENDIX A. STRUCTURAL DATA AND STATION LOCATIONS 120

APPENDIX B. PETROGRAPHY 138

EPILOGUE 148

LIST OF TABLES

Table

1. Anorthite content of plagioclase grains in the Labyrinth Mountain granodiorite pluton (Kbgg) 36

2. Major oxide compositions 37

3. Trace element data 38

4. Rare earth element data 39

5. Zircon uranium and lead isotope analyses, ages and uranium and thorium concentrations for sample 03NC126 43

6. Bulk compositions of pelitic samples used in thermodynamic modeling or geochronology 52

7. Outcrop-scale structural data 57

8. Fault plane data 82

9. Labyrinth Mountain pluton fracture data 83

10. Average garnet, plagioclase and biotite composition analyses for sample 03NC19A used in thermobarometry 95

11. Samarium and Neodymium isotope data for geochronology 97

12. Sample 03NC143: Inclusions within garnet and accessory matrix phases 103

LIST OF FIGURES

Figure

1. The Cascades crystalline core 2

2. Geologic map of the Nason terrane, Wenatchee block, Cascades crystalline core. 3

3. Isobars, Nason terrane 5

4. Map of structural data locations 23

5. Map of sample locations 26

6. Photomicrograph of Labyrinth Mountain granodiorite, sample 03NC126 40

7. Geochemical classification of granodiorite sills 41

8. U-Pb zircon ages for sample 03NCGB126 44

9. Nason terrane geochronology: U-Pb zircon and Sm-Nd garnet ages. 45

10. Comparison of zircon Th/U ratios as a function of U-Pb age 47

11. REE patterns and trace element plots 49

12. New mapping of the Labyrinth Mountain-Jove Peak area 53

13. Map of representative foliations 55

14. Map showing high temperature lineations 58

15. The Mount Stuart batholith structural aureole 59

16. Comparison of Chiwaukum Schist and Nason Ridge Migmatitic Gneiss foliations 61

17. Raft foliations and fold axes 65

18. X-Y plot foliation comparisons 66

19. Location 03NCGB126/04NCGB027 68

20. Raft structures 70

21. Intrusive dikes and sills 72

22. Stereonet plots of intrusives 75

23. Outcrop Map: Nason Ridge Migmatitic Gneiss, 04NCGB036 76

24. Outcrop Map: Nason Ridge Migmatitic Gneiss, 04NCGB035 77

25. Structural cross section from Jove Peak to Labyrinth Mountain 78

26. Minotaur Lake Fault rocks. 84

27. Map of representative dikes, sills, faults and joints in the Labyrinth Mountain/Minotaur Lake Fault area 85

28. Joint sets 86

29. Sample 03NC152: Photomicrograph (PPL) 88

30. A comparison of isograds and isobars in the southern Nason terrane 89

31. Garnet inclusion patterns 92

32. Sample 03NC19A: Peak assemblage stability field 98

33. Sm-Nd isochrons and garnet growth ages for samples 03NC143 and 03NC19A. 99

34. Loading constraints 106

ABSTRACT

Samarium-neodymium garnet geochronology, uranium-lead zircon geochronology and detailed structural and petrologic analyses place new constraints on the relationships between deformation, intrusion, metamorphism and loading in the southern Nason terrane, Cascades Crystalline core. Garnet leaching experiments result in high-precision Sm-Nd isochron ages for peak metamorphism of the Nason Ridge Migmatitic Gneiss synchronous with 90.6 ± 2.4 Ma emplacement the Labyrinth Mountain granodiorite pluton. Garnets in the pluton wall-rock thus likely grew in response to heating during magmatism. Intrusion and deformation in schist rafts and pluton wall-rock indicate that magmatism was active during NE-SW arc-normal contraction and was accommodated by wall-rock disaggregation, stoping, NE-SW shortening in the wall-rock and corresponding NW-SE extension. Peak metamorphic conditions preserved in the host rock at the time of the Labyrinth Mountain pluton emplacement are 6.6-8.4 kbar and 630-670 °C. This suggests that pressure increased at least 2.2 kbar after 93.5-96 Ma emplacement of the nearby Mount Stuart batholith. All data are compatible with SW-directed upper-crustal thrust-loading and mid-crustal folding prior to and synchronous with ca. 91 Ma magmatism and peak metamorphism. Microstructures evidence foliation development resulting from ductile shortening that locally postdates ca. 90-91 Ma garnet growth.

I
INTRODUCTION

Tectonic Models

Holocene glacial retreat from most of north central Washington has revealed exceptional three-dimensional exposure of well preserved metamorphic and igneous rocks in the Cascades crystalline core (Fig. 1 and Fig. 2). These rocks, exhumed during Cretaceous to Tertiary contraction, transpression and transtension (Paterson, Miller, Alsleben, Whitney, Valley and Hurlow 2004), offer a glimpse into mid-crustal deformational, magmatic and metamorphic processes at the core of a >500 km wide, Late Cretaceous, contractional, orogenic belt (Wyld, Umhoefer and Wright in press). Attempts at reconciling thermobarometric, geochronologic and structural data collected over decades with unifying frameworks for tectonic evolution have spawned intense debate. Relationships between deformation, magmatism and metamorphism have been the foundation of each unifying tectonic model, yet consensus has seldom been achieved. The advent of new analytical techniques and theoretical paradigms has stimulated new data collection, which, in turn, has forced reconsideration of established models.

Attendant to this cycle of data acquisition and model revision, however, is recognition of complexity. The purpose of this study is to construct a detailed chronology of Late Cretaceous deformation, intrusion and metamorphism, such that data must be compatible with processes understood at the local-scale before being attributed to

Figure 1. The Cascades crystalline core.
A) Tectonic setting of the Cascades crystalline core in the North American Cordillera (after Monger et al. 1982)
B) Map of the Cascades crystalline core showing major tectonic blocks, terranes and bounding faults (after Tabor et al. 1987). Nason Ridge Migmatitic Gneiss (NRMG); Wenatchee Ridge Gneiss (WRG); intrusives (black).

A

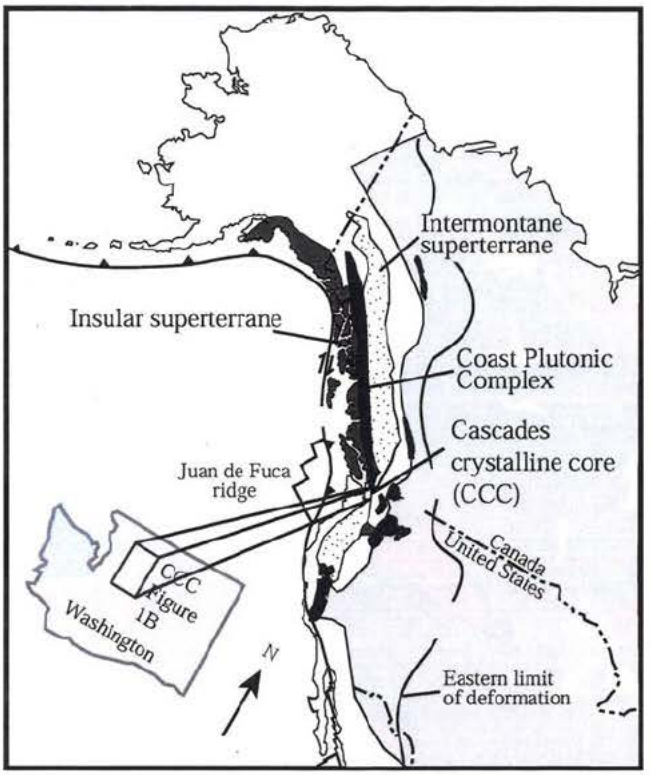

B

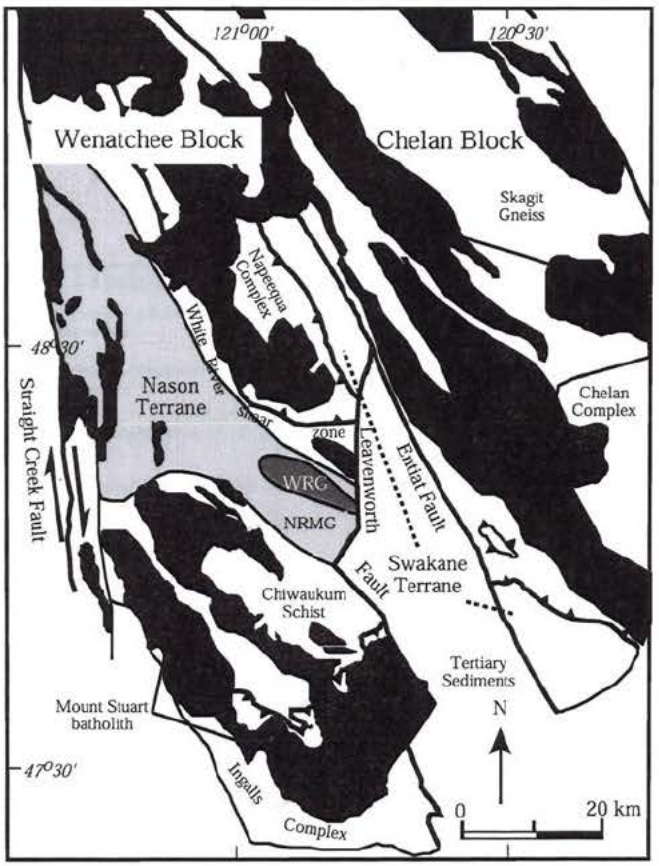

Figure 2. Geologic map of the Nason terrane, Wenatchee block, Cascades crystalline core. The dashed line denotes the Labyrinth Mountain-Jove Peak study transect. Kilometer-scale anitforms and synforms are inferred from foliation data (Van Diver et al. 1968; Tabor et. al 1987; Tabor et al. 1993; Paterson et al., 1994; ; Miller et al. 2000; H. Stowell, D. Tinkham, and C. Zuluaga, personal communication). Map modified from Tabor et al. (1987), Tabor et al. (1993) and Tabor et al. (2002).

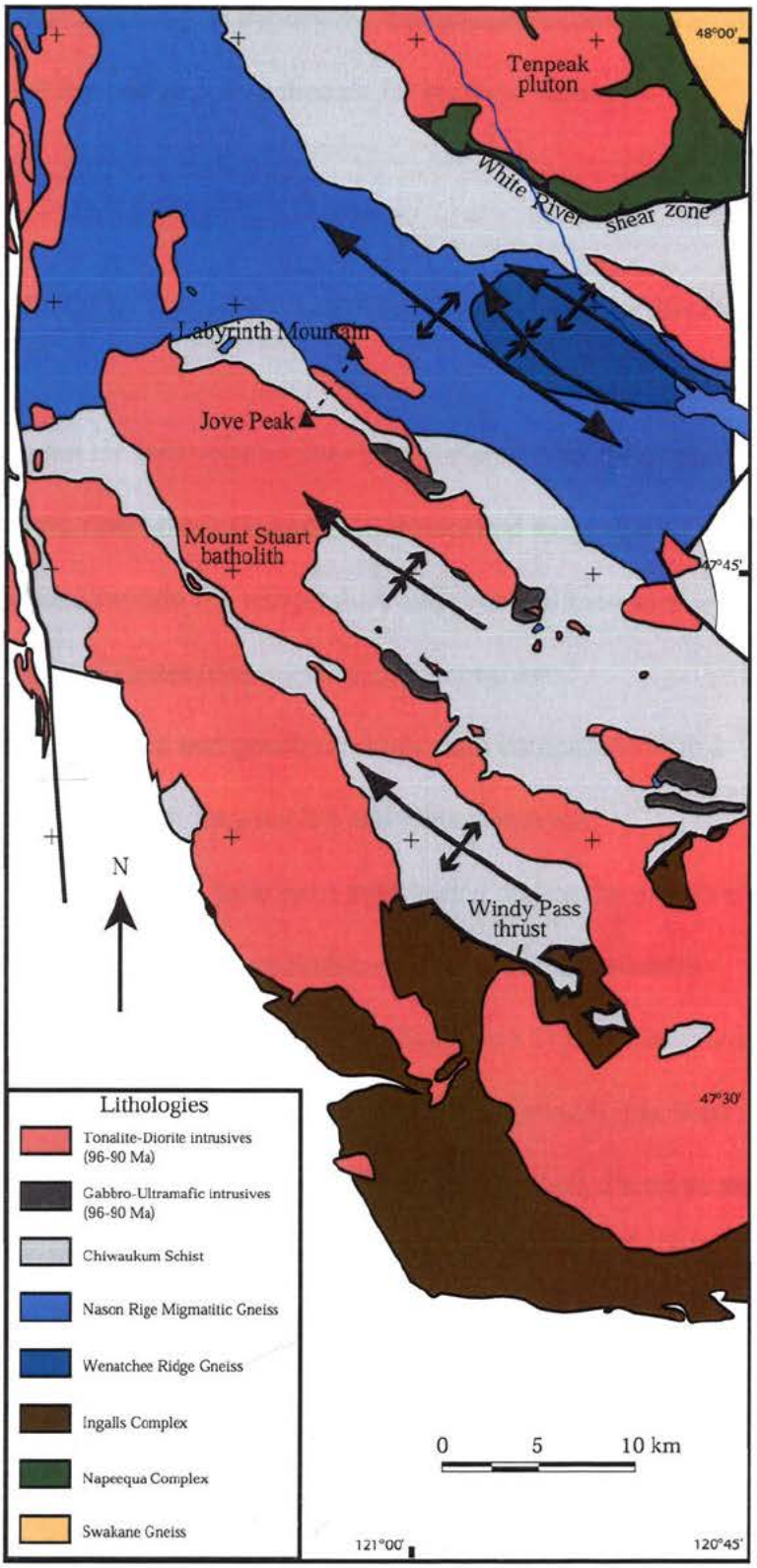

processes operating at the regional level. By extrapolation, complexity understood at the local-scale may help resolve problems confronting models for regional tectonics.

Tectonic Models

Unifying tectonic models for the Cascades crystalline core must address three major questions:

1) When and in what tectonic regime does magmatism occur: transtension, transpression, arc-normal compression or arc-normal extension?
2) What mechanisms explain the temperature and pressure increases responsible for Late Cretaceous regional metamorphism?
3) Are structural, petrologic and geochronologic data compatible with a conceptual model for both magmatism and metamorphism?

Three fundamentally different models have been entertained during the past two decades to explain the Late Cretaceous tecto-metamorphic evolution of the Cascades crystalline core: 1) a magma-loading model, 2) rigid block tilting, and 3) a tectonic/thrust loading model. Only one of these models, however, the thrust loading model, has been favored during the past five years (Evans and Davison 1999; Miller, Matzel, Paterson and Stowell 2003; Stowell and Tinkham 2003; Paterson et al. 2004). This model, too, has been revised continually since its inception. Following is a summary of the development of these conceptual models and important questions that remain.

All three models attempt to explain the steep paleobarometric gradients that decrease from NE to SW across the core (Fig. 3). But the rigid block tilting model alone appeals to a process other than Late Cretaceous crustal thickening. This model (Kriens

Figure 3. Isobars, Nason terrane. A) Isobars after Brown and Walker (1993). B) Isobars after Evans and Davidson (1999), Bulman (2004), and Stowell et. al. (accepted).

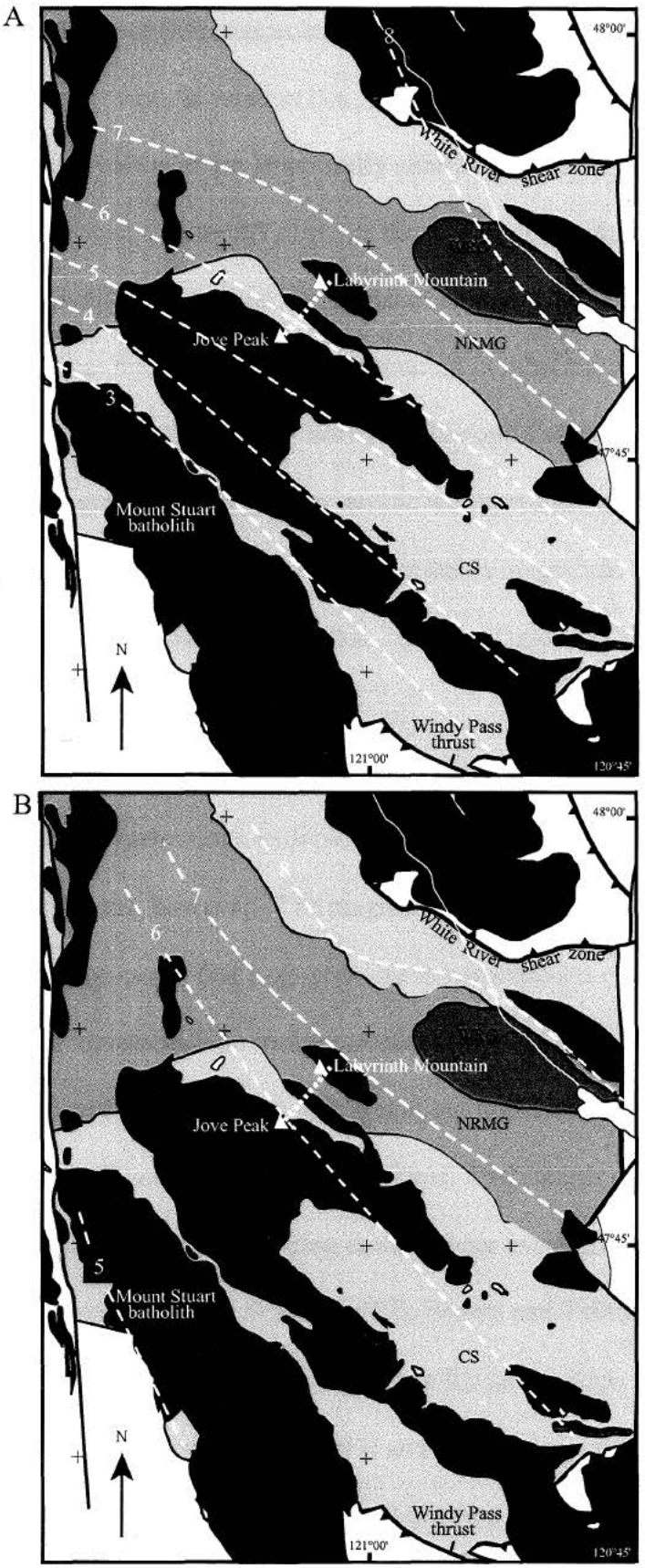

Lithologies

- Tonalite-Diorite intrusives (96-90 Ma)
- Gabbro-Ultramafic intrusives (96-90 Ma)
- Chiwaukum Schist (CS)
- Nason Rige Migmatitic Gneiss (NRMG)
- Wenatchee Ridge Gneiss (WRG)

5 Pressure (kbars)

0 5 10 km

and Wernicke 1990) suggests that the steep paleobarometric gradients and the exposed high grade rocks could be explained by vertical rotation (i.e., steep tilting) of the core to the SW, so that the present surface reveals a 30 km structurally continuous crustal section with increasing depth to the NE. Because this model obviates the role of post-intrusion pressure increases, post-intrusion ductile deformation and burial of supracrustal rocks for which there is so much evidence, it has been peremptorily discounted in most subsequent studies (Miller, Brown, McShane and Whitney 1993; Whitney, Miller and Paterson 1999). Additionally, the steep baric gradient in the Nason terrane would require tilting in excess of 45° from a vertically stratified crustal section—an improbable magnitude of rotation for which evidence should abound (Stowell, Bulman, Zuluaga, Tinkham, Miller and Stein accepted).

The magma-loading and thrust-loading models are both predicated on Late Cretaceous crustal thickening broadly synchronous with plutonism. The mechanisms invoked by each model are quite different, however. The magma-loading model (Brown and Walker 1993; Miller et al. 1993) proposes that high-pressure metamorphism overprinting lower pressure contact metamorphism in the aureoles of 96-90 Ma plutons in the Cascades crystalline core was caused by magmatic inflation of the upper crust and consequent downward displacement of host rock to higher pressures. Proponents of this model call upon magma emplacement during NW trending dextral shear concomitant with orogen-wide transpression as documented by Brown (1987), Brown and Talbot (1989), Longtine (1991), and Brown and Walker (1993). Evidence for the magma-loading model as summarized from Brown and Walker (1993) and Miller et al. (1993) follows: 1) If magmatism were the result of loading (i.e., crustal anatexis as proposed by

Zen (1988)), rather than the cause, it should lag loading by ca. 20 m.y. (England and Thompson 1984). The interpretation, therefore, that the Cascades crystalline core reveals broadly synchronous high-pressure metamorphism and magmatism (e.g., Walker and Brown 1991) is used as evidence to refute the thrust-loading model. 2) Lineations are generally shallow and orogen-parallel, suggesting a transpressional tectonic regime. 3) Metamorphic fabrics are often subvertical and parallel to pluton margins; there is little structural evidence for thin-skinned thrusting. 4) Steep paleobarometric gradients (Fig. 3A) represent a steep-sided load and are not suggestive of thrust loading. 5) Higher pressures are associated with an orogen-parallel zone of highly intruded migmatitic host rock thought to represent the roots of a now eroded upper-crustal steep-sided batholith. 6) The age of the ballooning upper-crustal batholith is estimated to be 90-84 Ma; this is compatible with loading of the older 96-91 Ma Mount Stuart batholith, where higher pressure metamorphism has overprinted a lower pressure contact aureole.

The distinction between evidence for co-magmatic Late Cretaceous dextral transpression and magma-loading induced high-pressure metamorphism is important to the current and future consideration of this model. If magma-loading were viable, could this magmatism have occurred during arc-normal contraction (Paterson and Miller, 1998a, 1998b) instead of during transpression (Brown and Talbot 1989)? Does evidence for dextral transpression support a magma-loading model exclusively? And if, as seems to be the trend, the magma-loading model lacks general acceptance, could distributed or strain-partitioned dextral transpression be reconciled with a thrust-loading model?

The thrust loading model is the longest-lived model for Cascades crystalline core tectono-metamorphic evolution. Middle to Late Cretaceous thrust-loading has been

attributed to two mechanisms: 1) crustal shortening resulting from collision of the Insular and Intermontane superterranes, and 2) intra-arc crustal shortening following collision of the two superterranes (Misch 1966; Monger, Price and Tempelman-Kluit 1982; Brandon and Cowan 1985; Whitney and McGroder 1989; Rubin, Saleeby, Cowan, Brandon, and McGroder 1990; McGroder 1991; Miller et al. 1993; Umhoefer and Miller 1996; Paterson and Miller 1998b). The first mechanism requires closure of a pre-existing terrane-intervening basin and inception of a magmatic arc during collision. The second mechanism requires formation of a magmatic arc related to E-dipping Farallon subduction during arc-normal contraction (Rubin et al. 1990). Earlier studies (Monger et al. 1982; Whitney and McGroder 1989; and McGroder 1991) prefer the collisional model. This model was contested, however, by Miller et al. (1993) on the basis of the implications for the timing of loading. For example, the McGroder (1991) model requires loading of the Intermontane terrane Twisp Valley schist during the onset of contractional loading at >100 Ma. Miller et al. (1993) argue, instead, that the schist was loaded after 88 Ma. Furthermore, Paterson and Miller (1998b) have demonstrated that arc-magmatism and arc-normal contraction were, in fact, coeval and that it is not uncommon for terrane-stitching (i.e., post-collisional) plutonism to precede significant tectonic crustal thickening (Haugerud, Brown, Tabor, Kriens and McGroder 1994; Paterson and Miller 1998a). Arc-normal contraction was followed by dextral transpression between 73–55 Ma (Paterson et al. 2004); thus, dextral transpression was not the dominant regime at 90 Ma, as proposed by Brown and Talbot (1989) and Brown and Walker (1993).

As in the magma-loading model, separating the general cause of crustal thickening (tectonic loading) from the specific mechanism (collision of superterranes or intra-arc thrusting/folding) is critical to evaluating the thrust-loading model. Recent studies focus less on the tectonic origin of loading and more on evidence for timing, rates, extent and magnitude. Evans and Davidson (1999) denote three distinct episodes of Mid- to Late Cretaceous metamorphism in the Mount Stuart domain and Nason terrane: (M1) regional metamorphism and deformation ca. 120 Ma (Plummer 1980; Evans and Berti 1986; Walker and Brown 1991; Paterson, Miller, Anderson, Lund, Bendixen, Taylor, and Fink 1994; Chace, Stowell, and Tinkham 1998), (M2) contact metamorphism associated with emplacement of the Mount Stuart batholith (Plummer 1980; Evans and Berti 1986; Brown and Walker 1993; Paterson et al. 1994), and (M3) regional metamorphism overprinting M2 contact metamorphism (Evans and Berti 1986; Paterson et al. 1994; Evans and Davidson 1999).

A steep isobaric gradient across the Nason terrane and Mount Stuart domain (Fig. 3A) was used as evidence by Brown and Walker (1993) to support a magma-loading model for M3 regional metamorphism. The apparent steepness of the proposed isobaric gradient across the Mount Stuart domain, however, largely relied upon the erroneous consideration of lower pressure M2 contact metamorphic mineral phases that had not re-equilibrated during M3 regional metamorphism (Evans and Davidson 1999). The imprint of the M3 higher-pressure metamorphism was extended across the Mount Stuart domain with evidence from staurolite-sillimanite-quartz veinlets (Evans and Davidson 1999). Isobars redrawn after Evans and Davidson (1999) and after Tinkham (2002) (Bulman et al. 2004; Stowell et al. accepted) reveal an effective break in slope of the baric gradient

NE of the Mount Stuart domain (Fig. 3B). This led Bulman et al. (2004) and Stowell et al. (accepted) to suggest that the apparent isobaric gradient is as much a function of post-loading tectonic contraction controlled by rheologic heterogeneity (Miller and Paterson 2001) as of the geometry of the imposed load. Essentially, the crystallized tonalite-diorite Mount Stuart batholith accommodated less post-loading contraction than the weaker Chiwaukum Schist and Nason Ridge Migmatitic Gneiss to the NE. This interpretation is consistent with models for the geometry of the imposed load (Bulman et al. 2004) that require >50% shortening across the Nason terrane NE of the Mount Stuart domain. The absence of evidence for SW-directed faults within this terrane suggests that contraction must have been accommodated through ductile processes (Paterson and Miller 1998a; Stowell et al. accepted). Garnet P-T-t paths for metapelites just NE of the Mount Stuart batholith, however, are compatible with thrust-loading (Stowell and Tinkham 2003; Stowell et al. 2005), thus leading Stowell et al. (accepted) to propose a decoupling of ductile mid-crustal contraction and upper-crustal thrusting.

From the previous discussion, a working hypothesis for Late Cretaceous crustal thickening involves intra-arc coeval decoupled upper-crustal thrusting and mid-crustal folding. But what is the role of magmatism? Is magmatism responsible for creating higher geothermal gradients during metamorphism (Whitney 1999; Miller et al. 2003), for advective heating of the Nason Ridge Migmatitic Gneiss pre-, syn- and post- loading (Evans and Davidson 1999); and for imparting lithologic heterogeneity and, thus, strain partitioning throughout the Nason terrane and Mount Stuart domain (Stowell et al. accepted; Miller and Paterson 2001)?

Geologic Setting

The Cascades crystalline core of north-central Washington is the southernmost exposure of the >1500 km Cretaceous to Paleogene Coast Plutonic Complex magmatic arc (Fig. 1A), which lies between the Intermontane superterrane to the east and the Insular superterrane to the west (Monger et al. 1982). The crystalline core is divided into two tectonic blocks, the Chelan block and Wenatchee block, separated by the Tertiary Entiat Fault (Fig. 1B). The core is bounded on the east by the Ross Lake fault and on the west by the Tertiary dextral Fraser River-Straight Creek fault, across which there may have been hundreds of kilometers of offset (Cowan, Brandon, and Garver 1997). The Wenatchee block is subdivided into litho-tectonic terranes, the southernmost of which is the Nason terrane and associated Mount Stuart domain (Fig. 1B; Tabor, Frizzel, Whetten, Waitt, Swanson, Byerly, Booth, Hetherington, and Zartman 1987; Tabor, Frizzel, Booth, Waitt, Whetten, and Zartman 1993; Haugerud et al. 1994; Paterson et al. 1994).

The Nason terrane is bounded by the Fraser-Straight Creek fault on the west, the Leavenworth fault on the east, the Windy Pass thrust on the south and the White River shear zone on the north (Fig. 1 B). The Windy Pass thrust is a folded shallowly SW-dipping structure that carries the Jurassic Ingalls ophiolite over the Chiwaukum schist. The ophiolite is characterized by ultramafic tectonites, gabbro, pillow basalt and diabase dikes, overlain by mudstone, chert, greywacke and intercalated limestone—all thought to represent the various components of a backarc basin (Miller 1985). Metamorphism reaches greenschist and amphibolite facies as it approaches the Windy Pass thrust. Ductile structures are steep in the upper part of the ophiolite and, in the lower part near the Windy Pass thrust, parallel to shallow imbricate thrusts (Miller 1985). The Windy

pass thrust was intruded by 93-91 Ma Mount Stuart batholith magmas. Development of a subhorizontal fabric where the thrust was intruded suggests that movement continued briefly after intrusion (Miller and Paterson 1992), but ceased upon final crystallization of the magma.

The Mount Stuart batholith (MS) is a predominantly tonalitic, granodioritic and dioritic assemblage of 96-90 Ma magmas (Tabor et al. 1993; Matzel 2004). These magmas are believed to have been assembled at the site of emplacement in the upper-crust subsequent to mid-crustal chemical and physical mixing of felsic crustal melts and a mantle-derived basaltic component (Miller, Paterson, DeBari, and Whitney 2000; Paterson et al. 1994; Anderson 1992). The batholith is characterized by magmatic folds and larger kilometer-scale subsolidus folds continuous with the host rock; even the large hook-shaped region of the batholith has been interpreted as a fold (Paterson et al. 1994).

The Nason terrane is predominantly comprised of the Chiwaukum Schist (CS) and Nason Ridge Migmatitic Gneiss (NRMG) (Tabor et al. 1987; Tabor et al. 1993; Tabor, Booth, Vance, and Ford 2002). The Chiwaukum Schist is pelitic mica schist with ancillary lenses of amphibolite and amphibole mica schist. Protoliths of the Chiwaukum Schist likely originated in an accretionary wedge of a Jurassic or Early Cretaceous island arc (Magloughlin 1993; Paterson et al. 1994; Monger and Journeay 1994). The Nason Ridge Migmatitic Gneiss is inferred to be a structurally lower section of the Chiwaukum Schist, variably intruded concordantly and discordantly by centimeter- to decameter-scale tonalite, granodiorite and pegmatite dikes and sills (Tabor et al. 1993; Paterson et. al. 1994; Zuluaga 2004). Wet partial melting of pelitic schist at pressures of 6-8 kbar and temperatures of 650-675 °C played an active role in the formation of quartz-plagioclase

leucosomes (Zuluaga 2004). In total, migmatite and intrusive material accounts for 10-99% of the rock by volume throughout the NRMG. Few data exist to constrain the timing of intrusion and partial melting in the NRMG. J.F. Magloughlin and R.L. Edwards (unpublished data) determined a tonalite age of ca. 103 Ma, and Walker and Brown (1991) presented U-Pb zircon ages of 89-90 Ma for the NRMG. Modeling results (Zuluaga 2004) suggested that some partial melting could have taken place as a result of regional metamorphism, perhaps accompanying both Mid- Cretaceous (M1) and Late Cretaceous (M3) metamorphism.

Ductile deformation in the Chiwaukum Schist and Nason Ridge Migmatitic Gneiss resulted in the repeated transposition of foliation into new structures. Paterson et al. (1994) identified transposition cycles related spatially and temporally to the emplacement of the Mount Stuart batholith. Cycles 1-2 ½ are characterized by SW-verging folds that developed normal to SW-NE contraction and by NW-SE shallowly plunging stretching lineations and fold axes. These structures are pre- to syn-Mount Stuart age. Transposition of these structures in a deformational aureole around the intruding Mount Stuart batholith defines cycle 4. Cycle 5 reflects SW-directed reverse ductile shear zones which accommodate post-Mount Stuart NE-SW contraction (Paterson et al. 1994).

One such SW-directed shear zone is the White River shear zone (WRSZ; Fig. 2), which separates the Nason terrane on the north from the Tenpeak domain. The WRSZ is a SW-directed reverse shear zone that brings up the 7-10 kbar 91-92 Ma Tenpeak pluton (Brown and Walker 1993; Dawes 1993) and host Napeequa Schist (Fig. 2; Tabor et al. 1987; Miller et al. 2000).

Integrated Geochronology, Petrology and Structural Geology

Over a distance of just 5 km, the Labyrinth Mountain-Jove Peak transect includes the northeastern margin of the Mount Stuart batholith, Chiwaukum Schist, Nason Ridge Migmatitic Gneiss and two small granodiorite plutons. The representative lithologies, good exposure and small scale make this study area ideal for understanding relationships between intrusion, deformation and metamorphism. For instance, this study has the potential to relate garnet-age metamorphism to the timing of local pluton crystallization in addition to regional-scale crustal loading processes. Likewise, the relative timing of deformation can be related to the absolute timing of pluton crystallization and peak metamorphism. While this study provides distinct advantages to interpreting isolated data in the context of a regional model alone, it necessitates a broad and demanding methodology—integrating petrology and structural geology with geochronology.

Large euhedral to subhedral garnet in peak metamorphic assemblages throughout the Chiwaukum Schist and Nason Ridge Migmatitic Gneiss, is ideal for observing porphyroblast-matrix microstructural relationships and is resistant to metamorphic resetting. The slow cation diffusion rates in garnet explain why garnet chemistry preserves prograde pressure/temperature conditions and ages. The samarium-neodymium (Sm-Nd) isotopic system in garnet has been studied and offers an excellent tool for determining the timing of peak metamorphism (e.g., Vance and O'Nions 1990; Stowell, Taylor, Tinkham, Goldberg, and Ouderkirk 2001; Thöni 2002) in rocks for which other isotopic systems (e.g., Rb-Sr or Ar-Ar) likely record resetting or cooling ages.

$^{147}Sm_{62}$ decays by alpha emission to $^{143}Nd_{60}$ with a half-life of 106 Byr. Hence:

$$^{143}Nd = {}^{143}Nd_i + {}^{147}Sm\left(e^{\lambda t} - 1\right), \text{ where } (\lambda = 6.54*10^{-12}/\text{yr}).$$

Dividing this equation through by ^{144}Nd—an effectively non-radiogenic isotope on timescales of hundreds of millions of years—permits a comparison of isotopic ratios for minerals and rocks with different concentrations of Sm and Nd and, therefore, provides the basis for calculating ages:

$$\frac{^{143}Nd}{^{144}Nd} = \left(\frac{^{143}Nd}{^{144}Nd}\right)_i + \frac{^{147}Sm}{^{144}Nd}\left(e^{\lambda t} - 1\right).$$

And, thus:

$$t = \frac{1}{\lambda}\ln\left(\frac{\left(\frac{^{143}Nd}{^{144}Nd}\right) - \left(\frac{^{143}Nd}{^{144}Nd}\right)_i}{\frac{^{147}Sm}{^{144}Nd} + 1}\right).$$

The isochron dating method arrives at the requisite initial ^{143}Nd/ ^{144}Nd ratio by linear regression. Two or more points define a line with (x,y) coordinates given by $\frac{^{143}Nd}{^{144}Nd}$ and $\frac{^{147}Sm}{^{144}Nd}$. However, both Sm and Nd are trivalent and have similar atomic numbers of 62 and 60, respectively. As a result, whole rock Sm/Nd ratios show little variability (i.e., they cluster on an x,y plot) and yield isochron lines with poor age resolution. Fortunately, mineral isochrons offer an improvement, and garnet is particularly well suited for this technique, as it shows strong HREE enrichment and preferentially incorporates Sm relative to Nd. Precise isochrons can be constructed using points for higher garnet Sm/Nd ratios and points for lower whole-rock or matrix ratios (Fig. 33).

Garnet is not only abundant, large and resistant to resetting, but often preserves chemical and isotopic zoning that can record multiphase prograde growth. Consequently, garnet rims may be in isotopic equilibrium with only the matrix, with which diffusion occurred during growth, whereas garnet cores are expected to be in equilibrium with the whole rock (Vance and O'Nions 1990). In this study, garnet core-rim separation was attempted even in the absence of evidence for multiphase growth, provided the garnet mass was adequate. Variations in core and rim $^{147}Sm/^{144}Nd$ ratios could themselves provide evidence for multiphase growth or for the rate of garnet growth. At the very least, separate core and rim $^{147}Sm/^{144}Nd$ ratios and Nd concentrations from a single growth phase garnet could increase the isochron precision (e.g., Stowell and Goldberg 1997) or, alternatively, indicate the presence of contaminant inclusions.

Perhaps the greatest impediment to obtaining accurate and geologically meaningful Sm-Nd garnet ages is the presence of LREE enriched mineral inclusions. For most samples presented here, garnets are only crushed and hand-picked under a binocular microscope for apparently clean garnet fragments. Additional cleaning is achieved with short duration acetone and low molarity nitric and hydrochloric acids baths. These steps are sufficient to avoid large matrix mineral inclusions and to remove some weathered surface material but are insufficient to remove microscopic inclusions. The presence of any LREE enriched mineral inclusion will result in $^{147}Sm/^{144}Nd$ ratios that do not reflect those in garnet, although the ultimate isochron age will prove erroneous only if the inclusions are in disequilibrium with or are a different age than garnet. For example, inclusions such as epidote, apatite and titanite may be cogenetic with or in equilibrium with garnet, and a Sm-Nd isochron will yield a true age. Conversely, mineral inclusions

with higher closure temperatures such as zircon and monazite may perturb the isochron age if they are older than the host garnet or if they closed to isotopic equilibration significantly before the garnet (Thöni 2002).

The question, then, is how can the reliability of a garnet isochron age be assessed without specific knowledge of the mineral inclusions? First, multiple samples or fractions with assumed similar histories must be analyzed. Second, samples showing different Nd concentrations and $^{147}Sm/^{144}Nd$ ratios must yield similar ages, thereby demonstrating either 1) the varying isotopic contribution of equilibrated inclusions (Thöni 2002) or 2) variability of core-rim or garnet-to-garnet REE concentrations (Stowell and Tinkham 2003). In ideal multiple analyses, similar $^{147}Sm/^{144}Nd$ ratios, Nd concentrations and ages would indicate a reliable age and either a general lack of LREE enriched inclusions or a homogeneous distribution of REE throughout the garnet. Third, leaching experiments may improve both the accuracy and precision of the isochron when inclusions are present.

Although microscopic or microprobe characterization of microscopic inclusions would help direct an appropriate leaching technique, the benefits of experimenting with various leaching techniques to remove unidentified inclusions outweigh the potential problems of sample mass loss and an increased blank. Leaching out LREE enriched phases will improve isochron accuracy if the inclusions are in disequilibrium and will increase the $^{147}Sm/^{144}Nd$ ratio of the garnet residue, thereby improving the isochron precision regardless of whether the phases are in equilibrium (Zhou and Henson 1995; DeWolfe, Zeissler, Halliday, Mezger, and Essene 1996; Thöni 2002; Anczkiewicz and Thirwall 2003; Vance, Muller, and Villa 2003). No studies document isotopic

fractionation resulting from leaching garnet with strong acids (Zhou and Henson 1995; DeWolfe et al. 1996; Thöni 2002). High temperature hydrochloric and sulfuric acid leaches are investigated here, using the methods of Thöni (2002) and Anczkiewicz and Thirwall (2003). High temperature and high molarity HCl leaching attacks calcium bearing phases such as epidote, apatite and titanite and may result in significantly higher $^{147}Sm/^{144}Nd$ ratios for the garnet residue (Thöni 2002). Monazite is potentially the most problematic inclusion for Sm-Nd garnet geochronology; with 10,000-100,000 times more Nd than garnet, a single submicroscopic crystal could alter the apparent age of and reduce the $^{147}Sm/^{144}Nd$ ratio of the host garnet (Dewolfe et al. 1996; Anczkiewicz and Thirwall, 2003). Hence, a recently proposed technique that dissolves only phosphate bearing phases, H_2SO_4 leaching, has dramatically increased the $^{147}Sm/^{144}Nd$ ratio of garnets suspected to contain monazite (Zhou and Henson 1995; Anczkiewicz and Thirwall 2003). Zircon inclusions are also theoretically capable of influencing $^{147}Sm/^{144}Nd$ ratios in garnet, particularly when garnet Nd concentrations are low and zircon Nd concentrations are relatively high (Thöni 2002) or when zircon inclusions are abundant (DeWolfe et al. 1996). The preponderance of work indicates that, in general, however, the relatively low Nd concentrations in zircon with respect to the host garnet render negligible the effect of zircon inclusions on the apparent garnet age (DeWolfe et al. 1996; Scherer, Cameron, and Blichert-Toft 2000; Anczkiewicz and Thirwall 2003).

Accurate and precise garnet ages are critical to dating high-pressure metamorphism in areas in which garnet growth occurred in a high-pressure mineral assemblage. These ages alone, however, date pressure and temperature conditions for garnet growth, not tectonic processes. Testing models for tectono-metamorphic evolution

requires understanding the relative timing of high-pressure metamorphism and magmatic intrusion, among other important structural, petrologic and geochronologic relationships. For example, if high-pressure metamorphism predates intrusion, it is unlikely that magma loading from local intrusion caused the peak metamorphic conditions. Instead, such a relationship might suggest that crustal thickening associated with high-pressure metamorphism initiated lower crustal melting (England and Thompson 1984; Zen 1988). Alternatively, high-pressure metamorphism synchronous with or post-dating intrusion—on a timescale compatible with heat transfer from the cooling magma to the metamorphosed country rocks—provides evidence for the role of intrusion in creating peak temperatures on a local scale, if not peak pressures as well.

Whereas Sm-Nd garnet isochrons date the timing of garnet growth experienced by schist in the Labyrinth Mountain area, U-Pb zircon geochronology for a granodiorite pluton gives the timing of zircon crystallization in an intrusion. Uranium-lead zircon geochronology is perhaps the most widely applied and studied method for dating the crystallization ages of felsic to intermediate igneous rocks. The U-Pb system is particularly useful because it provides a pair of parent-daughter isotopes that should yield the same age, a concordant age, for timescales spanning the history of the earth.

^{238}U produces ^{206}Pb, and ^{235}U produces ^{207}Pb, both through alpha and beta decay with half-lives of 4.47 Byr and 704 Myr, respectively:

$$^{206}Pb = {}^{206}Pb_i + {}^{238}U\left(e^{\lambda t} - 1\right) \qquad (\lambda = 1.55125 * 10^{-10}/y)$$

$$^{207}Pb = {}^{207}Pb_i + {}^{235}U\left(e^{\lambda t} - 1\right) \qquad (\lambda = 9.8485 * 10^{-10}/y).$$

Zircon is ideal for U-Pb geochronology as it occurs widely, incorporates high concentrations of radiogenic U and virtually no Pb, and resists metamorphic resetting. The U-Pb zircon system makes the assumption that initial Pb is negligible. Thus, isotopic ratios share a common age (t) and create a concordia line in (x,y) space. These ratios are given as:

$$\frac{^{206}Pb}{^{238}U} = \left(e^{\lambda t} - 1\right)$$

$$\frac{^{207}Pb}{^{235}U} = \left(e^{\lambda t} - 1\right).$$

Concentrations of ^{207}Pb were low in the relatively young zircons from the Labyrinth Mountain pluton and were, consequently, the source of prohibitive error. Ages in this study, therefore, rely on only the ^{206}Pb/^{238}U ratios from multiple zircons (Fig. 8; Table 5).

While the timing of intrusion and metamorphism is paramount to evaluating tectonic models, understanding the source of the magma is critical to relating processes documented in the Labyrinth Mountain area to the rest of the Nason terrane and Cascades Crystalline Core. For example, it is important to ascertain whether the intrusive bodies dated here are genetically related to the Mount Stuart batholith and whether they represent predominantly crustal anatexis (Zen 1988) or a mantle derivative. Major, trace, rare earth element (REE) and zircon Th/U data are used here to characterize pluton petrogenesis (Anderson 1992; Paterson et al. 1994; Sawyer 1996; Keay, Lister, and Buick 2001; Miller et al. 2003).

Finally, kilometer to millimeter scale structures, as evidenced by field mapping and data collection and thin section microstructural analyses, provide a context for petrologic and geochronologic data: What is the extent of the structural aureole of the Mount Stuart batholith? What is the relationship between deformation and pluton emplacement? What is the relationship between intrusion and deformation in the Nason Ridge Migmatitic Gneiss. Is garnet porphyroblast growth pre- syn-, inter-, or post-tectonic?

II
METHODS

Structural Analyses

Structural data were collected in the field during July and August of 2003 and 2004. Samples, sketches, digital photographs and GPS location readings supplement field notes and mapped data. Unpublished measurements and samples collected by University of Washington graduate student Gary Davidson during 1992 and 1993 augment this dataset.[1] Structural data were collected for 122 locations between Jove Peak and Labyrinth Mountain, a transect distance of ca. 5 km (Fig. 4).

This study seeks to serve as a demonstration of the efficacy of Geographic Information Systems (GIS)-facilitated structural analysis for the Cascades Crystalline core. Data were tabulated in Microsoft Excel[2] by location. By column, the location ID (e.g., 03NCGB124) is followed by a choice of structural-lithologic zones (Appendix A), choice of "P" or "L" (i.e., planar or linear), type of structure (e.g., schistosity, gneissosity, fold axis, slickenside), azimuth reading, angle from horizontal, and dip or plunge direction. Thus, any row can contain linear or planar data for any location in any predefined structural-lithologic zone. After the laborious task of entering the data, mapping and selecting specific structural data was very easy.

---

[1] Courtesy of Professor Bernard Evans, University of Washington, Seattle, Washington.
[2] Microsoft® Excel 2002, Copyright © Microsoft Corporation 1985-2001.

Figure 4. Map of structural data locations. The study transect extends from Jove Peak on the northeastern edge of the Mount Stuart batholith (SW corner of map) to Labyrinth Mountain (NE).
Contacts after Tabor et al. (1987); compare with Figure 12.

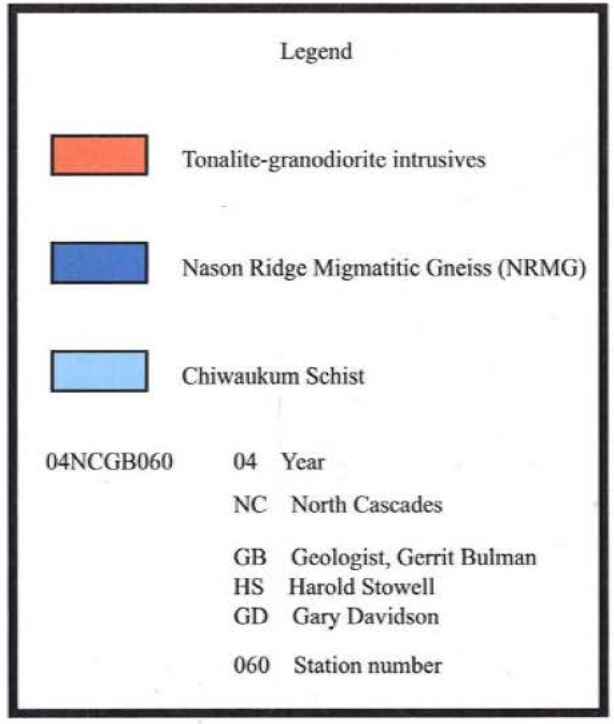

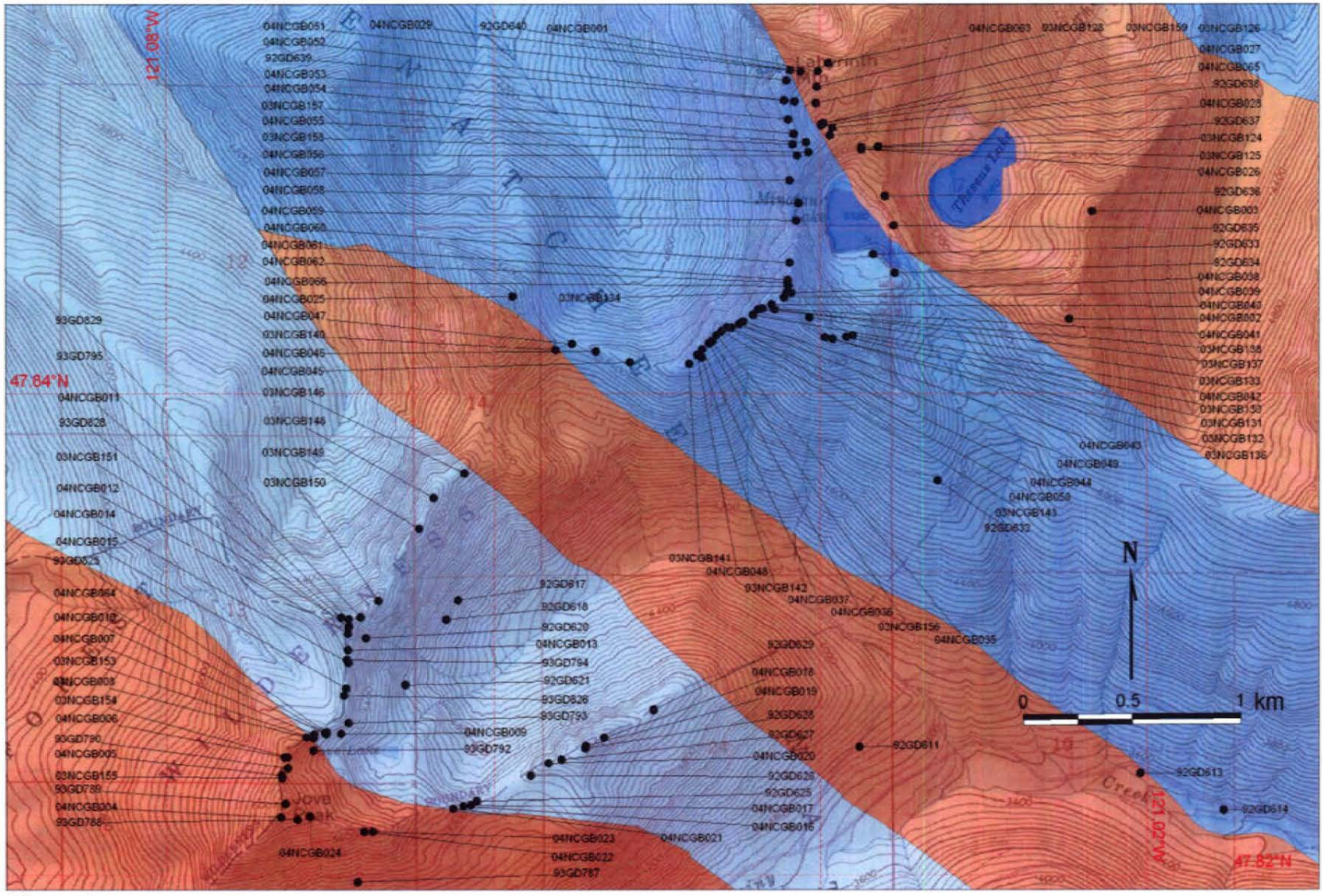

Figure 4.

The Excel table was exported to Microsoft Access where it was joined by location ID to a table containing latitude and longitude coordinates. The coordinate table was created by 1) entering and plotting GPS points in the GIS program MapInfo[3] against a background raster theme or layer containing a coordinate registered topographic map imported from TOPO![4] and 2) correcting the GPS locations using the invariably more accurate field maps. In Access, a master table was created that contains both coordinate locations and structural data (Appendix A). Desired structural data could be subsequently queried in Access and imported into MapInfo to create layers displaying only desired data (e.g., all lineations in zone 5). Alternatively, data could be queried in MapInfo (i.e., selected by location) and exported to Access as a new table.

In either case, data subsets in Access were easily created and exported. This proved a powerful tool for equal angle stereonet analyses. Tables in Access were exported as ASCII text files and directly read by StereoWin.[5]

Petrology

A suite of 117 samples represent the compositional, mineralogical and textural variation across the study transect (Fig. 5). Four analytical techniques were employed to collect petrologic data: petrography (thin section and hand sample), Inductively Coupled Plasma Optical Emission Spectrometry (ICP-OES), Inductively Coupled Plasma Mass Spectrometry (ICP-MS), and X-ray Fluorescence (XRF).

The major element compositions of two whole rock schist samples (03NCGB143 and 03NCHS19A) and six whole rock orthogneiss samples (03NCGB126, 03NCGB139,

---

[3] MapInfo v8.0, Copyright© 2005, MapInfo Corporation.
[4] USGS digital topographic maps, Copyright© 2002, National Geographic Maps.
[5] StereoWin for Windows, Copyright© 2002, Richard W. Allmendinger.

Figure 5. Map of sample locations. The study transect extends from Jove Peak on the northeastern edge of the Mount Stuart batholith (SW corner of map) to Labyrinth Mountain (NE).
Contacts after Tabor et al. (1987); compare with Figure 12.

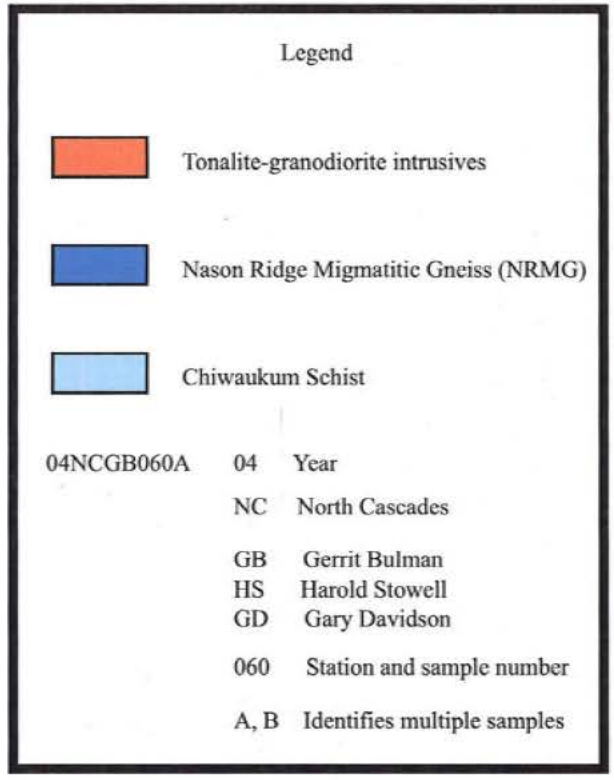

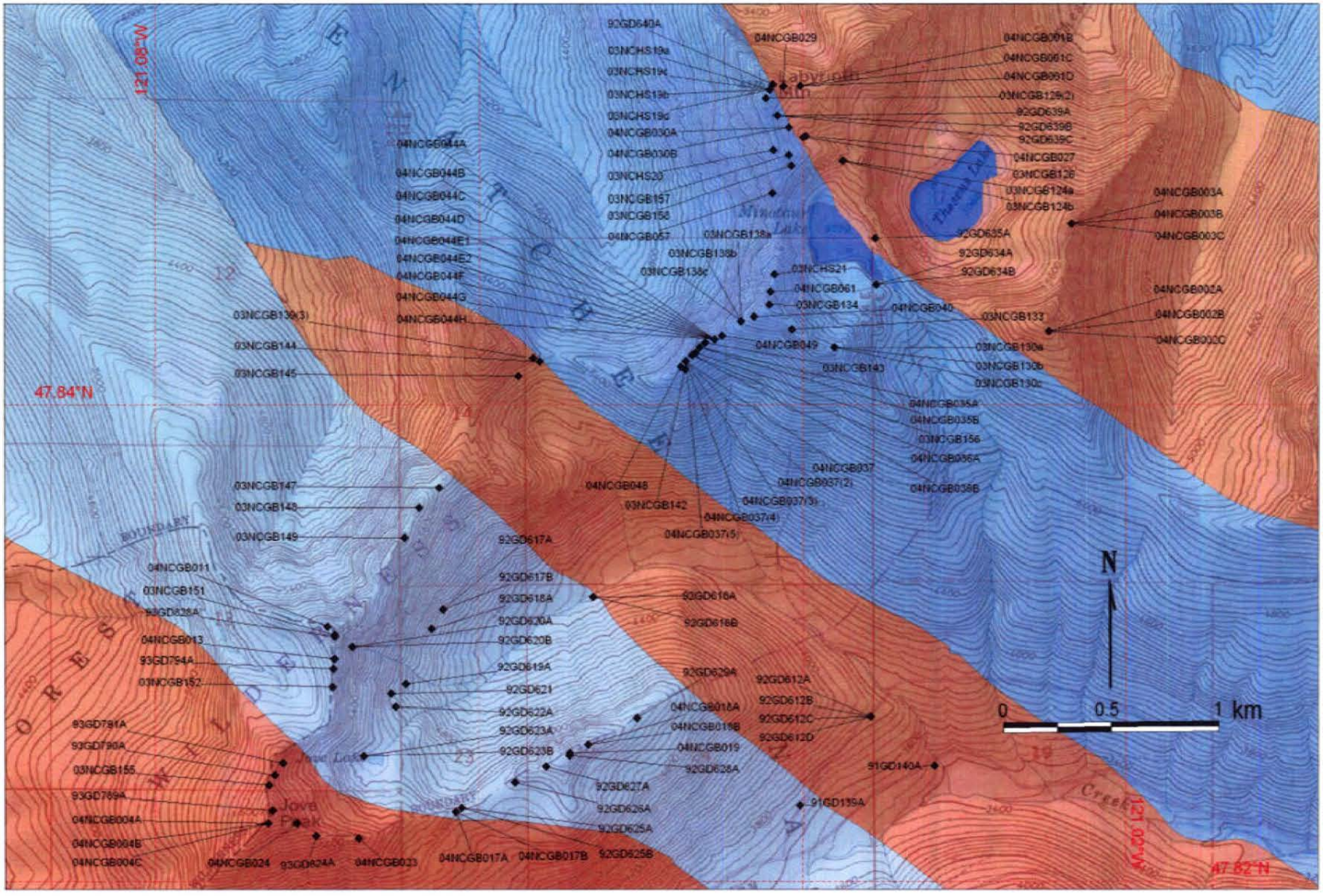
121.08°W
47.84°N
121.02°W
47.82°N
Labyrinth Mtn
Thrush Lake
Mirror Lake
Jove Fork
Jove Lake
Creek
BOUNDARY
N
0
0.5
1 km
92GD640A
03NCHS19a
03NCHS19e
03NCHS19b
03NCHS19c
04NCGB030A
04NCGB030B
03NCHS20
03NCGB157
03NCGB158
04NCGB057
03NCGB138a
03NCGB138b
03NCGB138c
03NCHS21
04NCGB061
03NCGB134
04NCGB040
04NCGB029
04NCGB061B
04NCGB061C
04NCGB061D
03NCGB129(2)
92GD639A
92GD639B
92GD639C
04NCGB027
03NCGB126
03NCGB124a
03NCGB124b
92GD635A
92GD634A
92GD634B
03NCGB133
04NCGB003A
04NCGB003B
04NCGB003C
04NCGB002A
04NCGB002B
04NCGB002C
04NCGB044A
04NCGB044B
04NCGB044C
04NCGB044D
04NCGB044E1
04NCGB044E2
04NCGB044F
04NCGB044G
04NCGB044H
03NCGB139(3)
03NCGB144
03NCGB145
04NCGB049
03NCGB143
03NCGB130a
03NCGB130b
03NCGB130c
04NCGB035A
04NCGB035B
03NCGB156
04NCGB036A
04NCGB037
04NCGB037(2)
04NCGB037(3)
04NCGB037(4)
04NCGB037(5)
04NCGB038B
04NCGB048
03NCGB142
03NCGB147
03NCGB148
03NCGB149
92GD617A
92GD617B
92GD618A
92GD620A
92GD620B
92GD619A
92GD621
92GD622A
92GD623A
92GD623B
92GD616A
92GD616B
92GD629A
92GD628A
92GD627A
92GD626A
92GD625A
92GD625B
04NCGB018A
04NCGB018B
04NCGB019
92GD612A
92GD612B
92GD612C
92GD612D
91GD140A
91GD139A
04NCGB011
03NCGB151
93GD835A
04NCGB013
93GD794A
03NCGB152
93GD781A
93GD790A
03NCGB155
93GD789A
04NCGB004A
04NCGB004B
04NCGB004C
04NCGB024
93GD824A
04NCGB023
04NCGB017A
04NCGB017B

Figure 5.

03NCGB145, 04NCGB030A, 99NC2 and 99NC55) were determined by ICP-OES. Trace element concentrations in the six orthogneiss samples were determined by ICP-MS. The major element composition of whole rock schist sample 03NCGB152 was determined by XRF.

Samples for ICP-OES, ICP-MS and XRF were pulverized to <100 microns using a low-carbon steel ring-and-puck mill. ICP samples were fused with a lithium metaborate and lithium tetraborate fluxing agent and subsequently dissolved in a 5% nitric acid solution containing an internal standard. This fusion technique is preferred for resistant geologic materials, for which acid digestion may be incomplete. The ICP-OES samples were analyzed on a combination simultaneous/sequential Thermo Jarrell-Ash ENVIRO II ICP or a Spectro Cirros ICP by Activation Laboratories Ltd., Ontario, Canada. Analyte-emitted radiation was correlated to analyte concentration using USGS and CANMET certified reference calibration materials. Trace element analyses were conducted using ICP-MS, a technique which collects data from the plasma-generated ions rather than photons. Although more expensive, this technique offers detection limits 3 to 4 orders of magnitude better than ICP-OES. The solution used for ICP-OES was divided, spiked and diluted to ensure that trace element concentrations fell within the analyte signal region of quantification. Samples were run on a Perkin Elmer SCIEX ELAN 6000 ICP-MS by Activation Laboratories Ltd., Ontario, Canada. XRF analyses of a fused glass disc were conducted on a Phillips PW2400 X-ray Fluorescence Spectrometer equipped with a Rh X-ray tube at the University of Alabama.

Sm-Nd Garnet Geochronology

Ages for garnet growth in the Labyrinth Mountain area are based on Sm-Nd garnet-matrix-whole-rock isochrons for samples 03NCGB143 and 03NCHS19A. This demanding technique employs mechanical separation of whole-garnet or garnet rims and representative matrix (i.e., whole rock minus garnet), garnet leaching, complete rock and mineral dissolution, bulk REE separation, Sm and Nd separation from bulk REE, and precise Sm and Nd isotope concentration measurements.

Samples of schist showing the least weathering and largest apparently clean garnets were selected for candidacy, thin-sectioned and reassessed based on garnet morphology, size, color and number of inclusions, and dissected with small chisels to retrieve the largest glassy euhedral garnets. Core-rim separation was attempted on most garnets >5 mm using a diamond coring drill. Whole garnets or garnet fractions were then shattered to <1 mm size pieces with a steel percussion mortar and hand-picked for inclusion-free pieces in alcohol with the aid of a 20x binocular microscope. Optically clean garnet was next ground with an agate mortar and pestle to fine-sand size. The ground samples were cleaned with successive rinses of acetone, doubly distilled (2x) 2.5 M HNO_3, ultrapure H_2O, 2x 2 M HCl and finally ultrapure H_2O, all in watch glasses at 25 °C for one to two hours. Solutions were siphoned off between steps.

Matrix samples were prepared from unweathered rock adjacent to the selected garnets, rinsed in 2M HCl and acetone, crushed and picked free of visible garnet at 20x magnification. Unweathered representative whole rock samples were also rinsed in 2 M HCl and acetone. Both matrix and whole rock samples were then dried, ground in a low-

carbon steel ring and puck mill, cleaned in acetone again and leached in 2x 2M HNO_3 overnight.

Leaching performed on garnet samples involved pulverizing the hand-picked and cleaned garnet for an additional 10-15 minutes under ultrapure water in an agate mortar. This reduced the grain size to 2-20 μm, presumably exposing microscopic inclusions. The powdered sample and water was centrifuged and the water was pipetted off. The samples were then leached/cleaned for one hour at 25 °C with 2x 2M nitric acid in the centrifuge tube. Several ultrasonic treatments assisted cleaning/leaching. The garnet powders were again separated from the liquid, dried and weighed. Mass lost was negligible. Samples were transferred to a Teflon screw-cap vial and leached in 2x 6M HCl at 100 °C for 12 hours—or in 2x 5M HCl at 85 °C for 6 hours—and intermittently subjected to ultrasonic treatment. Leachate was separated from the garnet residue via centrifugation, and the residue was rinsed three times with ultrapure water. Subsequent drying and weighing revealed a 27% mass loss for the sample leached for 12 hours at higher temperature and higher molarity. Such loss cannot be attributed to inclusion dissolution and iron oxide removal alone. Instead, this result corroborates the findings of DeWolfe et al. (1996) that garnet is attacked by high temperature-high concentration HCl leaching. Samples leached for 6 hours and at a lower temperature and HCl molarity lost only 8% of their mass. Finally, the samples were leached in 1 ml 2x 98% H_2SO_4 at 180 °C for 24 hours to dissolve any remaining monazite. The viscosity and high concentration of sulfuric acid made leachate-residue separation more difficult. However, diluting the mixture prior to centrifugation facilitated successful separation.

Dried room-temperature samples were weighed to the 0.01 mg accuracy, averaging at least four repetitions and taking precautions to mitigate the error introduced by air currents, building vibrations, and static charge on the glassine weighing paper and Teflon vials. Matrix and whole rock samples weighed 100-200 mg, and garnet samples weighed 50-250 mg (Table 11). Garnet samples were spiked for isotope dilution using 70 μl of the University of North Carolina Basalt spike (UNC "B") per 100 mg of garnet. Matrix and whole rock samples were spiked with 1 ml, and the blank was spiked with 70 μl.

All samples were then dissolved in 15 ml screw-cap Savillex Teflon vials with 1-2 ml of a 20:1 solution of concentrated 2x HF: 2x 7M HNO_3 on a 120 °C hotplate enclosed in a ventilated Plexiglas evaporation box. Dissolution and fluoride compound disintegration was assisted by periodically cooling the samples to room temperature and placing them in an ultrasonic bath. Samples were checked daily for visible solids and, after 2-3 days, evaporated to drive off the fluoride compounds. Following this step, samples found to be incompletely dissolved were again subjected to HF digestion, or if satisfactorily digested, were redissolved and dried in a sequence of steps to convert remaining fluorides to chlorides: 2x 6M HCl, 2x 12M HCl and 2x 2M HCl. Samples were redissolved in 0.5 ml 2x 2M HCl and centrifuged for 10 minutes to separate any solid chlorides.

Samarium and neodymium were separated using two ion chromatography methods. First, 0.25 ml aliquots of each sample were loaded onto BIO-RAD AG 50W-X8 polypropylene cation exchange columns. Bulk REE separates were eluted with 2x 6 M HCl. Second, separates of Sm and Nd were eluted from the bulk REE separates using

0.225 M methylactic acid (αHIBA) and an AG 50W-X4 200-400 mesh cation exchange resin in silica columns. Finally, aqua regia—a volatile 3:1 mixture of 2x HCl:2x HNO_3—is added to the Sm and Nd samples and evaporated at 90 °C to drive off the methylactic acid.

Samarium and neodymium isotope ratios were measured by thermal ionization mass spectrometry (TIMS). Samples were analyzed by the author and by Dr. Staci Loewy on a VG Sector 54 TIMS at the University of North Carolina, Chapel Hill. In preparation for loading, dried samples were dissolved in 0.5 ml 6 M 2x HCl and evaporated to dryness after 2-3 μl 0.5M H_3PO_4 was added to each sample. Neodymium was then loaded onto a single center Re filament in 2 μl 2.5 M 2x HCl. Parafilm dams helped focus the neodymium to a 1-2 mm spot on the filament. The Parafilm was burned off by increasing the filament current to 1.5 A prior to loading the filament into the turret block. Despite the potential for similar mass oxide interferences, low mass Nd separates were measured as NdO to enhance the signal intensity and duration. The signal intensity was further increased by introducing a small stream of oxygen into the chamber to promote NdO formation during Nd ionization. Intensities for ^{144}Nd ranged from 0.150-2.00 V for garnet samples run between 2.4-2.7 A. Sm was loaded onto a triple filament with a Re center and Ta sides and was run as a metal. Neodymium was measured in dynamic mode on eight Farraday collectors, and Sm was measured in multi-collector static mode.

Isochrons were constructed using the Microsoft Excel add-in Isoplot 3.00 (Ludwig 2003) and the linear regression algorithm described by York (1969). Neodymium concentrations were corrected for mass fractionation to ^{146}Nd/^{144}Nd =

0.7219 (O'Nions et al. 1977). Oxygen is corrected for the NdO analyses such that $^{18}O/^{16}O = 2.114*10^{-3}$ and $^{17}O/^{16}O = 0.392*10^{-3}$ (Thirwall 1991). Sm isotope concentrations are corrected to $^{149}Sm/^{152}Sm = 0.51685$ (Wasserburg et al. 1981). Two-sigma (2σ) uncertainties for the ratios $\frac{^{143}Nd}{^{144}Nd}$ and $\frac{^{147}Sm}{^{144}Nd}$ were calculated as the square root of the sum of the squares of the absolute 2σ run error and the external standard reproducibility error. External reproducibility was calculated to be ± 0.000004 (2 standard errors) from multiple recent University of North Carolina TIMS analyses of the J Ndi standard, which has an accepted $\frac{^{143}Nd}{^{144}Nd}$ of 0.512116 ± 0.000008.

U-Pb Zircon Geochronology

The Laser Ablation Inductively Coupled Mass Spectrometry (LA-ICPMS) technique used in this study to obtain isotope concentrations offers a few advantages to traditional Thermal Ionization Mass Spectrometry (TIMS): Isotope data for U, Pb and Th can be collected simultaneously, and many individual grains for one sample can be analyzed fairly rapidly to reveal heterogeneous age populations. Age precision, however, may be compromised in samples containing a single cogenetic population.

Seventeen magmatic zircons from granodiorite-tonalite sample 03NCGB126 were analyzed with a Micromass Isoprobe multi-collector ICPMS by Dr. George Gehrels at the University of Arizona. A New Wave DUV 193 laser ablated 35 μm spots on individual zircons to a depth of ca. 20 μm. Concentrations of ^{206}Pb, ^{207}Pb, ^{208}Pb, ^{232}Th, and ^{238}U were measured in static mode with 9 Faraday detectors. Non-radiogenic ^{204}Pb was measured simultaneously with a secondary electron multiplier.

Analyses were corrected for minor initial incorporation of Pb in the zircon lattice by normalizing $^{206}Pb/^{204}Pb$ to the composition of common lead from a general Pb terrestrial evolution calculation (Stacey and Kramers 1975). Corrections for mass fractionation of $^{206}Pb/^{238}U$ and $^{206}Pb/^{207}Pb$ were based on fractionation observed in a concordant zircon of known age; this calibration zircon was run once for every four samples. Two-sigma (2σ) standard deviations for the ratios $^{206}Pb/^{238}U$ and $^{206}Pb/^{207}Pb$ were calculated from 2% error associated with the calibration zircon isotope composition uncertainty and 1% error associated with the decay constant and common lead ratio uncertainty. The age of zircon crystallization was ultimately based on the weighted mean of the 17 zircon $^{206}Pb/^{238}U$ ages determined. Two-sigma (2σ) age uncertainty was calculated from the quadratic sum of the weighted mean error and the standard deviations for the measured $^{206}Pb/^{238}U$ values (Dr. George Gehrels, University of Arizona, personal communication).

III
THE LABYRINTH MOUNTAIN PLUTON

Northeast of the Mount Stuart batholith, two 5-10 km long NW-trending granodiorite sills cross the study area (Fig. 2); the more northeastern sill is herein referred to as the Labyrinth Mountain pluton. Both sills are designated Cretaceous gneissic biotite granodiorite (Kbgg) in USGS publications (Tabor et al. 1993) and are composed of medium-grained, light-colored, weakly foliated granodiorite with locally variable amounts of biotite and muscovite. Zircon, apatite and titanite are accessory phases. Plagioclase occurs as relatively large subhedral laths with compositions of An_{25} -An_{30} and commonly displays normal core to rim oscillatory compositional zoning (Table 1), Carlsbad twinning and albite twinning (Fig. 6). Subhedral to anhedral alkali feldspar and quartz occur interstitially, often as myrmekite and granophyre intergrowths. Muscovite is potentially secondary, as it is frequently observed on the rims of biotite grains (Fig. 6; Appendix B).

The Labyrinth Mountain pluton and its sister sill to the SW are similar petrographically (Appendix B) and chemically (Table 2 and Table 3; Fig. 7). Silica accounts for 65-70 weight percent, total iron (as Fe_2O_3) 2.5-3.7 percent, $Na_2O + K_2O$ 6-7%, and CaO 2.8-4.1 percent. Empirical igneous classification schemes predict that all five chemically analyzed Kbgg samples fall within the granodiorite field (e.g., Fig. 7A) and plot compositionally closer to smaller granitoid dikes and sills from the NE margin of

Sample	Grain	CW angle (deg)	CCW angle (deg)	Average
03NCGB127				
	1	21	25	23
	2	16	13	14.5
	3	9	8	8.5
	4	10	12	11
	5	12	12	12
	6	11	12	11.5
An Content	**28%**			**13**
03NCGB126				
	1	13	11	12
	*2 core	15	15	15
	*2 rim	10	9	9.5
	3	8	8	8
	*4 core	12	11	11.5
	*4 rim	8	9	8.5
An Content	**26%**			**11**

* Where core to rim oscillatory zoning is overprinted by albite twinning, cores show slightly higher An content.

Table 1. Anorthite content of plagioclase grains in the Labyrinth Mountain granodiorite pluton (Kbgg). Anorthite (An) contents were estimated petrographically using the Michel-Levy method (Nesse, 2004), in which extinction angles are measured clockwise (CW) and counter-clockwise (CCW) from sets of albite twin lamellae.

	98NC55	99NC2	03NC126	03NC139	03NC145	04NC030 A
SiO2	70.40	70.80	70.13	65.09	65.85	68.57
Al2O3	14.18	14.81	15.72	16.90	16.79	16.10
Fe2O3 (T)	3.32	2.79	2.45	3.68	3.64	3.02
MnO	0.061	0.017	0.024	0.027	0.027	0.025
MgO	1.66	0.59	0.63	1.26	1.23	0.83
CaO	2.62	2.77	2.94	4.11	3.91	3.30
Na2O	3.21	3.71	4.04	4.28	4.24	4.27
K2O	2.49	2.37	2.86	1.89	2.27	2.44
TiO2	0.358	0.413	0.407	0.733	0.727	0.600
P2O5	0.10	0.08	0.13	0.23	0.22	0.21
LOI	1.14	0.37	0.37	0.71	0.50	0.26
TOTAL	99.53	98.71	99.69	98.90	99.40	99.62

Table 2. Major oxide compositions. The Labyrinth Mountain granodiorite pluton (03NC126 and 04NC030A), the SW Kbgg sill (99NC2, 03NC139 and 03NC145) and the Mount Stuart batholith near Heather Lake (98NC55). All data in weight percent.

	98NC55	99NC2	03NC126	03NC139	03NC145	04NC030 A
Sc	9	0	2	3	3	2
Be	2	2	2	2	2	2
V	48	15	13	31	30	16
Cr	63	79	0	0	0	0
Co	6	24	3	6	6	4
Cu	10	0	0	14	19	30
Zn	64	0	78	123	131	221
Ga	16	16	23	25	25	26
Ge	1.4	0.0	0.8	0.7	0.8	0.7
Rb	72	71	76	63	75	80
Sr	265	440	539	566	533	529
Y	17.8	2.7	3.9	5.9	5.8	4.7
Zr	107	106	101	145	143	170
Nb	5.8	2.8	3.7	4.2	4.2	5.0
Cs	3.6	2.9	3.1	3.2	3.2	3.4
Ba	844	906	1,010	675	842	956
Hf	3.9	3.2	3.1	4.2	4.3	4.8
Ta	0.62	0.19	0.26	0.34	0.38	0.31
W	0.0	1.8	0.0	0.0	0.0	0.0
Tl	0.59	0.12	0.60	0.53	0.66	0.62
Pb	24	6	21	16	18	24
Bi	0.3	0.0	0.5	0.6	0.2	0.4
Th	12.6	5.48	5.68	5.49	6.19	8.88
U	4.24	1.77	2.75	1.84	1.99	1.93

Table 3. Trace element data. Labyrinth Mountain granodiorite pluton (03NC126 and 04NC030A), the SW Kbgg sill (99NC2, 03NC139 and 03NC145) and the Mount Stuart batholith near Heather Lake (98NC55). All abundances in ppm.

	98NC55	99NC2	03NC126	03NC139	03NC145	04NC030 A
La	26.5	19.2	19.6	20.8	22.4	28.1
Ce	49.2	37.0	36.8	42.5	46.1	55.7
Pr	5.44	4.28	4.80	5.25	5.64	6.56
Nd	19.5	16.0	18.9	21.1	22.8	25.1
Sm	3.59	2.73	3.64	4.30	4.43	4.39
Eu	0.725	0.915	1.11	1.27	1.29	1.26
Gd	3.06	1.73	2.43	3.00	3.16	2.83
Tb	0.47	0.16	0.24	0.32	0.34	0.26
Dy	2.57	0.56	0.83	1.15	1.25	0.94
Ho	0.51	0.07	0.10	0.17	0.17	0.12
Er	1.44	0.15	0.23	0.37	0.39	0.27
Tm	0.217	0.018	0.029	0.046	0.049	0.036
Yb	1.45	0.11	0.17	0.26	0.28	0.22
Lu	0.233	0.016	0.026	0.036	0.038	0.031

Table 4. Rare earth element data. The Labyrinth Mountain granodiorite pluton (03NC126 and 04NC030A), the SW Kbgg sill (99NC2, 03NC139 and 03NC145) and the Mount Stuart batholith near Heather Lake (98NC55). All abundances in ppm.

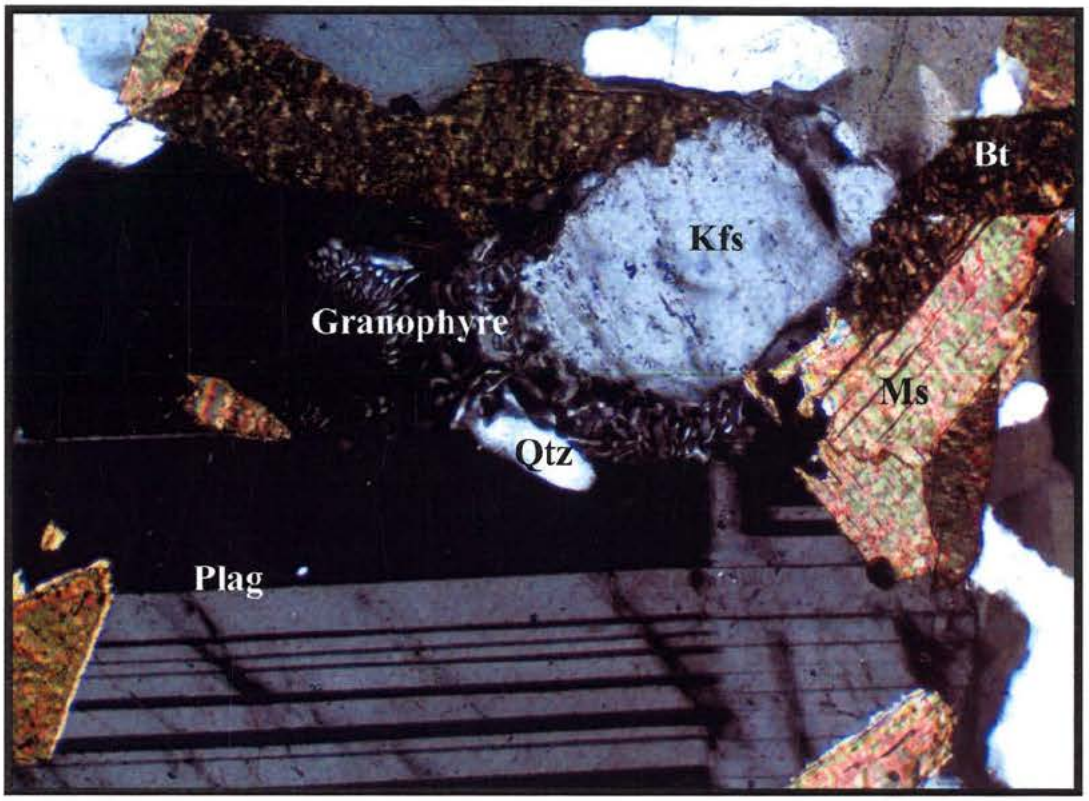

1 mm

Figure 6. Photomicrograph of Labyrinth Mountain granodiorite (sample 03NC126). A large plagioclase lath shows albite and Carlsbad twinning (bottom and middle); granophyre and quartz are interstitial; muscovite is both intergrown with biotite and replacing biotite along rims (bottom left); alkalai feldspar is subhedral to anhedral. Zircons, from which a U-Pb age of 90.6 +/- 2.4 Ma was determined, are concentrated in the biotite grains.

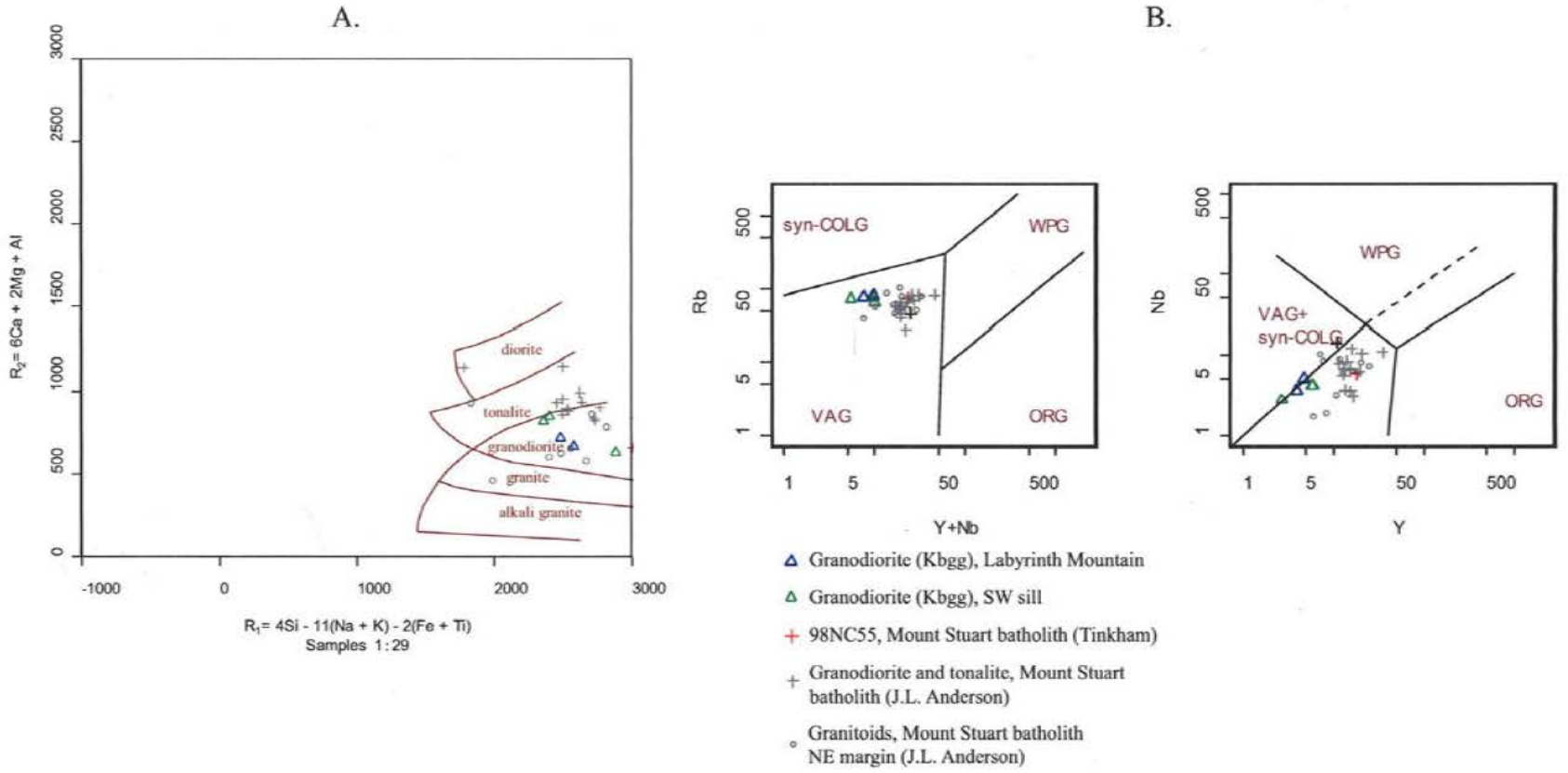

Figure 7. Geochemical classification of granodiorite sills. The Labyrinth Mountain pluton and SW granodiorite sill (Kbgg) are compared phases of the Mount Stuart batholith and associated granitoids on the NE side of the hook region of the batholith, all of which have similar SiO2 contents. Mount Stuart data after J.L. Anderson in Paterson et al. (1994) and Tinkham (2002).
A) Empirical igneous classification, after DeLaRoche (1980). B) Empirical tectonic classification after Pearce et al. (1984). WPG (within plate granite), ORG (ocean ridge granite), syn-COLG (syn-collisional granite), VAG (volcanic arc granite).

the Mount Stuart batholith than to tonalite and granodiorite phases of the Mount Stuart batholith proper (Fig. 7; Paterson et al., 1994). Tectonic classifications (Fig. 7) based on trace element data (Table 3) show that the Labyrinth Mountain granodiorite is empirically similar to volcanic arc granites (sensu lato) and to syn-collisional granites (sensu lato).

Timing of Intrusion

Granodiorite sample 03NC126, collected just south of Labyrinth Mountain (Fig. 5), provides a U-Pb zircon age of 90.6 ± 2.4 Ma. The 90.6 Ma ± 2.4 Ma age is the weighted mean of $^{206}Pb/^{238}U$ ages from 17 zircons (Fig. 8; Table 5). Because the isotope data were analyzed using LA-ICPMS and the sample is relatively young, the $^{207}Pb/^{235}U$ data were considered unreliable. Individual $^{206}Pb/^{238}U$ zircon ages generally overlap each other within analytical uncertainty (Fig. 8), suggesting the population is cogenetic. Hence, 90.6 ± 2.4 Ma is interpreted to represent the age of emplacement.

The 90.6 ± 2.4 Ma emplacement age for the Labyrinth Mountain pluton is very similar to ages for the Dirtyface pluton (91.1 ± 1.6 Ma) and Tenpeak pluton (91 Ma) (Fig. 9; Walker and Brown, 1991; Hurlow, 1992). However, the Labyrinth Mountain pluton age appears younger than ages for the closest Mount Stuart batholith geochronology samples (Fig. 9). Matzel (2004), for example, presented precise TIMS U-Pb zircon ages of 95.68 ± 0.05 Ma and 96.03 ± 0.05 Ma (internal analytical error only) for the northeastern hook region of the Mount Stuart batholith (Fig. 9).

Origin

Zircon Th/U ratios have been used to differentiate between magmatic and metamorphic petrogenesis (Williams and Claesson 1987; Sawyer 1996; Keay et al. 2001;

Zircon	$^{207}Pb/^{235}U$	± 1 SD (%)	$^{206}Pb/^{238}U$	± 1 SD (%)	6/8 Age*	±(Ma)	U (ppm)	Th (ppm)	Th/U
1C	0.0859	4.8362	0.0138	3.5414	88.2	3.1	2168	1365	0.63
2C	0.0953	4.2595	0.0145	2.8015	92.9	2.6	2432	127	0.05
3C	0.0907	5.5278	0.0143	1.9541	91.6	1.8	1543	136	0.09
4C	0.0958	3.0261	0.0147	2.1610	93.9	2.0	2129	171	0.08
5C	0.0924	6.0610	0.0149	5.4309	95.5	5.1	1753	80	0.05
6C	0.0579	16.1578	0.0142	1.4656	90.7	1.3	1009	30	0.03
7C	0.0853	6.1878	0.0135	2.2343	86.5	1.9	1957	118	0.06
8C	0.0768	14.5108	0.0144	3.2505	92.5	3.0	919	93	0.10
9C	0.0560	19.7914	0.0135	4.4634	86.5	3.8	2600	189	0.07
10C	0.0768	16.3612	0.0139	5.9009	89.0	5.2	1112	51	0.05
11C	0.0850	4.1548	0.0141	2.4049	90.1	2.2	2648	88	0.03
12C	0.0975	9.3716	0.0149	3.0044	95.2	2.8	574	55	0.10
13C	0.1023	29.7551	0.0141	3.0796	90.1	2.8	514	149	0.29
14C	0.0715	37.7183	0.0138	5.3674	88.5	4.7	62	4	0.07
15C	-0.0064	111.5549	0.0132	9.5726	84.5	8.0	430	231	0.54
16C	0.0773	15.5654	0.0134	4.6693	85.8	4.0	2090	88	0.04
17C	0.0424	72.4846	0.0134	7.7229	85.8	6.6	364	13	0.03

* $^{206}Pb/^{238}U$ age.

Table 5. Zircon uranium and lead isotope analyses, ages and uranium and thorium concentrations for sample 03NC126. Data were collected by Dr. George Gehrels at the University of Arizona using Laser Ablation Inductively Coupled Mass Spectrometry (LA ICPMS).

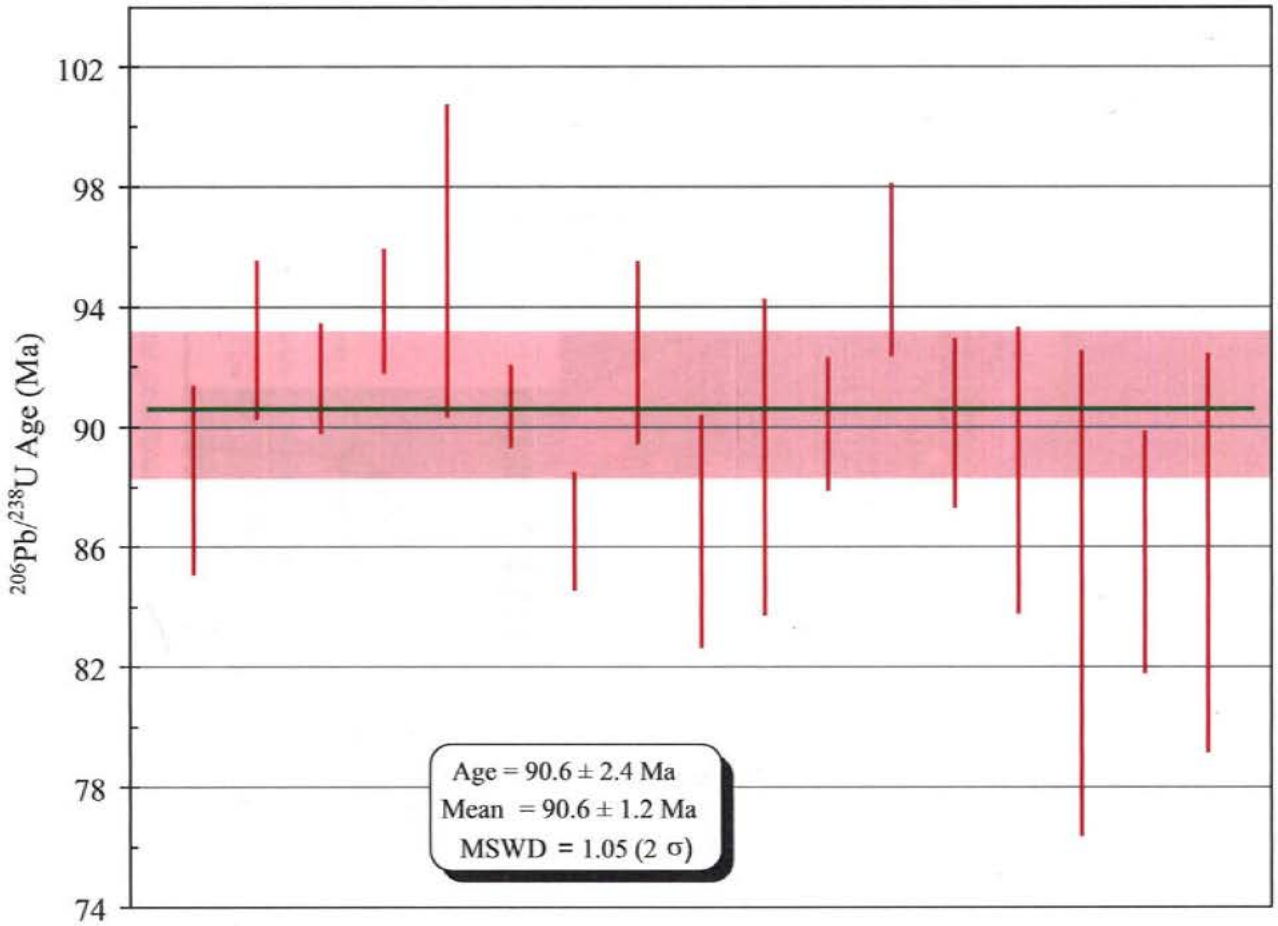

Figure 8. U-Pb zircon ages for sample 03NCGB126. $^{206}Pb/^{238}U$ age data for 17 zircons from Labyrinth Mountain granodiorite pluton (Kbgg). Error bars include two standard deviations from the mean. The sample age (90.6 +/- 2.4 Ma) is based on the weighted mean of the zircon ages. Analyses were performed by George Gehrels, University of Arizona, using LA-ICPMS.

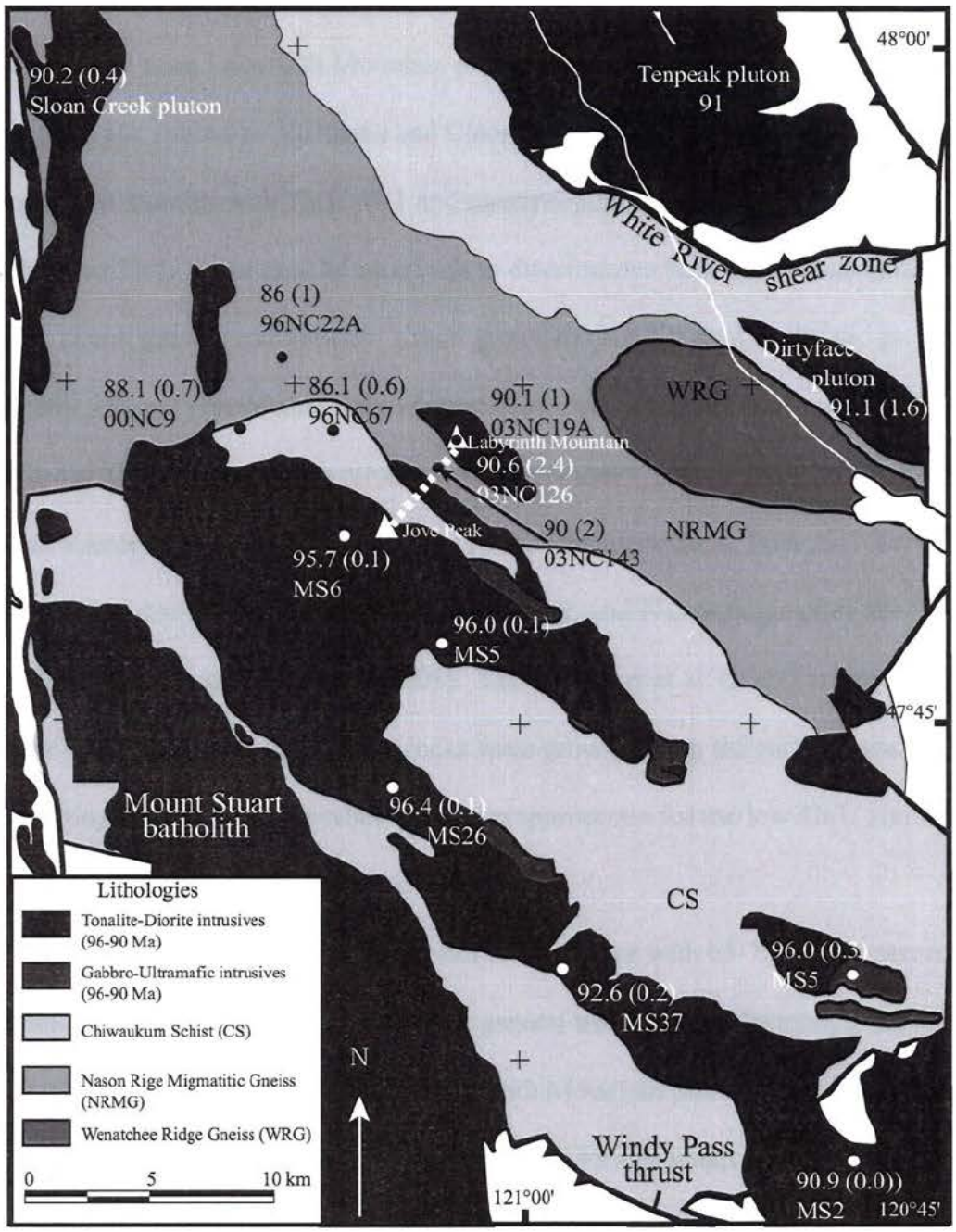

Figure 9. Nason terrane geochronology: U-Pb zircon and Sm-Nd garnet ages (Ma). Mount Stuart batholith (Matzel 2004); Dirtyface pluton (Hurlow 1992); Tenpeak pluton and Sloan Creek pluton (Walker and Brown 1991); 03NC126, Labyrinth Mountain pluton (this study); Garnet ages (Tinkham 2004; this study).

Tomaschek, Kennedy, Villa, Lagos, and Ballhaus 2003). Eighty-two percent of the zircons analyzed from Labyrinth Mountain pluton sample 03NC126 have Th/U ratios less than 0.1 (Fig. 10; Table 5). Williams and Claesson (1987) first identified an association between zircon mantles with Th/U <0.1 and metamorphism. Keay et al. (2001) postulated that Th/U ratios may be used both to discriminate between metamorphic and magmatic zircon growth and between zircon grown during different magmatic processes. Specifically, zircons precipitated from metatextites—melts that are produced locally—exhibit lower Th/U ratios than do zircons from diatextites—pervasive melts that migrate from their source (Keay et al. 2001; Sawyer 1996). Intrusive rocks from the Naxos core reveal a trend of decreasing Th/U with increasing age, and Naxos migmatites show low Th/U independent of age (Keay et al. 2001). This led Keay et al. (2001) to hypothesize that lower Th/U zircons from intrusive rocks were grown during the early stages of partial melting. A similar interpretation may be appropriate for the low Th/U zircons from the Labyrinth Mountain granodiorite.

Zircon Th/U ratios from granodiorites and tonalites with 65-70 weight percent SiO_2 from the Mount Stuart batholith show a general trend toward decreasing Th/U with increasing age (Fig. 10; Matzel 2004). Labyrinth Mountain pluton zircon Th/U ratios are unexpectedly low for their age with respect to the Mount Stuart batholith trend (Fig. 10; Table 5). The data, however, show a striking similarity to Th/U ratios for Mount Stuart granodiorite and tonalite samples near Jove Peak (Fig. 10)—close spatially to Labyrinth Mountain but not temporally (Fig. 9).

A common thorium-depleted source for both the Labyrinth Mountain granodiorite and the nearby Mount Stuart batholith phases is one possible explanation for the

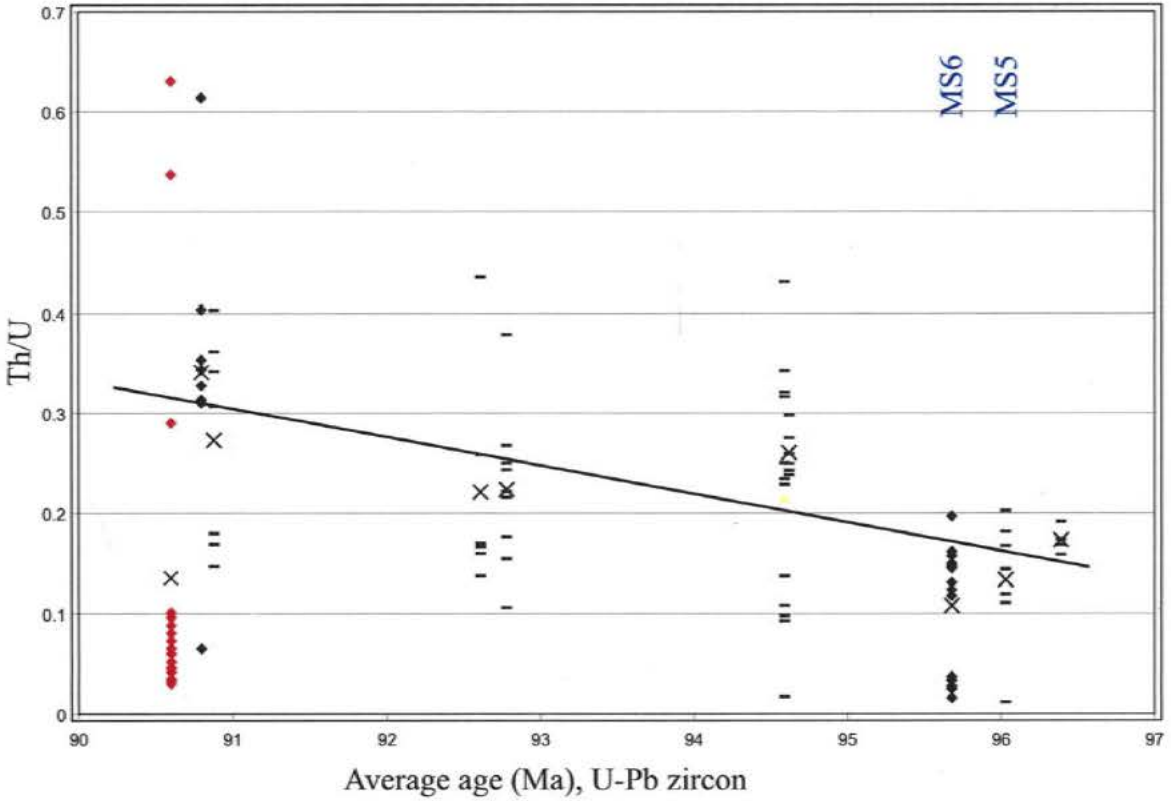

Figure 10. Comparison of zircon Th/U ratios as a function of U-Pb age. Labyrinth Mountain granodiorite data (Kbgg, sample 03NCGB126) are represented by red diamonds. Black diamonds represent Mount Stuart batholith granodiorite data, and black dashes represent Mount Stuart batholith tonalite data. Mean Th/U ratios for each sample are indicated by a black X. Note the general decrease of in Th/U with increasing age for the Mount Stuart batholith data. The trendline is fit to the mean values of the Mount Stuart batholith data ($R^2 = 0.69$).

unexpectedly similar Th/U ratios in samples with different ages (Fig. 11). An alternative magmatic origin interpretation of low zircon Th/U ratios is predicated on the assumption that zircon grew in a metatextite chemical environment associated only with early partial melting; such melts are depleted in Th, Y and REEs (Sawyer 1996). Labyrinth Mountain granodiorite samples are lower in Y than both tonalite and granodiorite phases of the Mount Stuart batholith and granitoids from the northeastern margin of the batholith (Fig. 7B; Table 4). Hence, zircon Th/U data from the Labyrinth Mountain pluton support an initial partial melt origin at 90.6 ± 2.4 Ma, but a reconciliation of the zircon Th/U ratios from the Mount Stuart batholith and from the Labyrinth Mountain pluton requires a more complex petrogenesis.

Compared to Mount Stuart batholith samples, Labyrinth Mountain pluton samples are depleted in Y and HREE but not in LREE (Fig. 7B; Fig. 11; Table 3 and Table 4). Labyrinth Mountain rocks show a steeper LREE to HREE slope and a concave-up HREE pattern (Fig. 11). This REE pattern is more similar to patterns for the deeper-seated, lower-crustal, 91 Ma Tenpeak pluton (Paterson et al. 1994; Miller et al. 2000) than to patterns for the upper-crustal Mount Stuart batholith. Based on field observations and chemistry, Paterson et al. (1994) and Miller et al. (2000) proposed that the felsic end-members of the Tenpeak pluton originated from partial melting of garnet-bearing lower-crust. Labyrinth Mountain pluton samples likewise show LREE enrichment and HREE depletion diagnostic of partial melts from a garnet-bearing source (Fig. 11; Table 4). The Tenpeak pluton, emplaced at 20-35 km depth, preserves incompletely mixed felsic crustal melt phases and mafic mantle-derived phases (Miller et al. 2000). Shallower level homogenization of mantle-derived mafic phases and felsic crustal melts has been

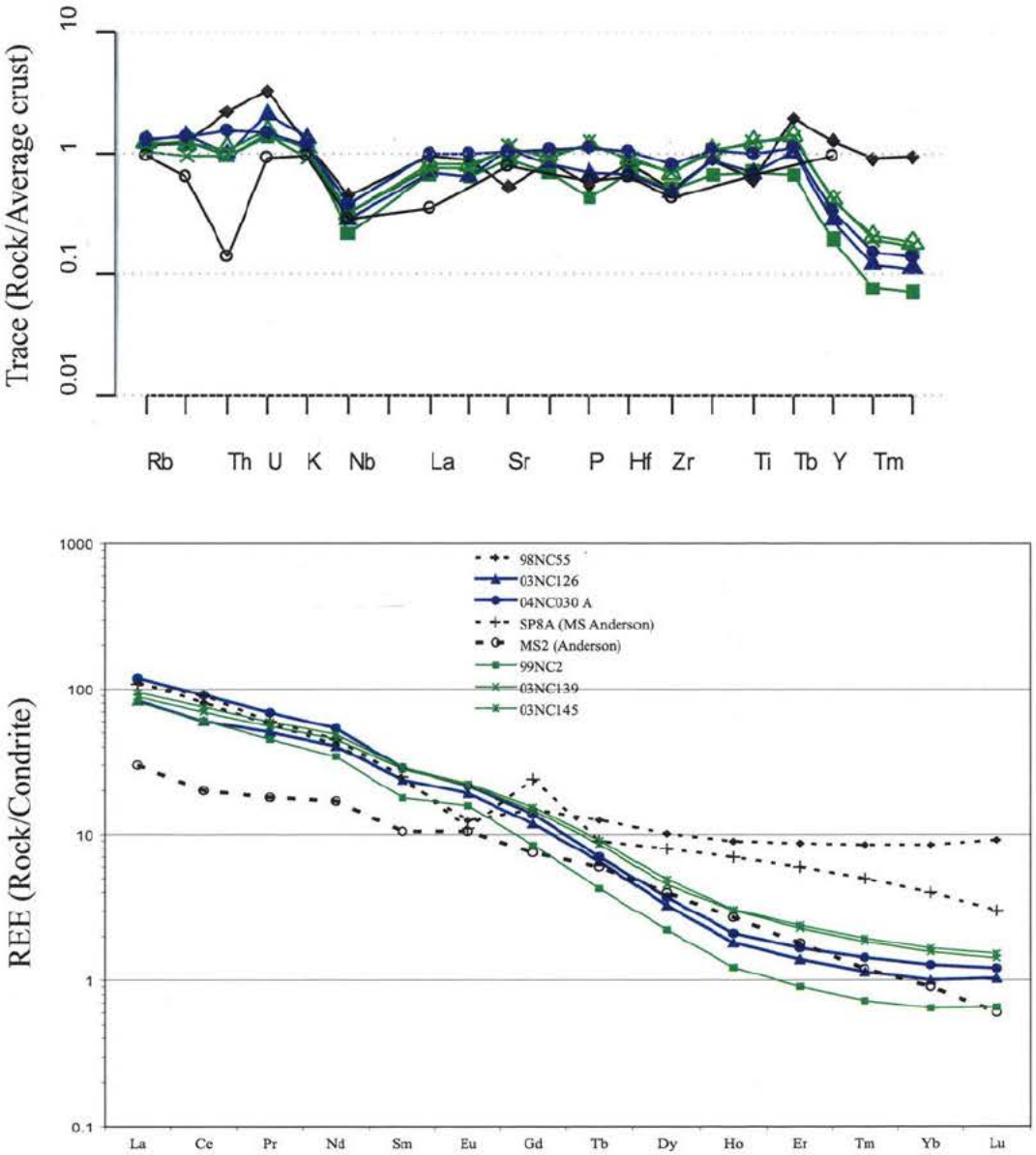

Figure 11. REE and trace element spider plots. Comparison of condrite normalized (Sun and McDonough 1989) REE patterns and average crust normalized (Weaver and Tarney 1984) spider plots from the Labyrinth Mountain granodiorite sill (Kbgg, samples 03NC126 and 04NC130), the SW granodiorite sill (Kbgg, samples 99NC2, 03NC139 and 03NC145) and from tonalite phases of the Mount Stuart batholith (98NC55, SP8A and MS2). All samples contain 65-71% SiO2. Data for samples SP8 and MS2 are after Paterson et al. (1994) and were collected and analyzed by J.L. Anderson, University of Southern California.

proposed to explain the different geochemical signature of the Mount Stuart batholith (Miller et al. 2000).

Geochemical similarities (Fig. 11; Table 3 and Table 4) strengthen the petrographic evidence (Appendix B) that the Labyrinth Mountain pluton and SW Kbgg sill are related in origin, whereas the differences between the Kbgg REE pattern and the Mount Stuart batholith REE pattern suggest a different petrogenesis for the Mount Stuart batholith. This difference may be attributable to magma mixing (Miller et al. 2000) and not necessarily to a fundamentally different lower-crustal locus of partial melting.

Assuming a spatially proximal garnet-bearing source region for Mount Stuart batholith magmas and the Labyrinth Mountain granodiorite magma, a conceptual model could account for the differences in zircon Th/U, age and REE trends:

1) Mount Stuart batholith granodiorites and tonalites originated from early partial melting in the lower crust ca. 96 Ma. This may explain the Th/U versus age trend.
2) These magmas mingled with mantle-derived mafic magmas, perhaps even in the middle- and upper-crust, producing voluminous homogenous magmas at the site of emplacement—a possible explanation for the hybrid REE signature.
3) Partial melting initiated again at ca. 91 Ma and produced km-scale granodiorite sills at a mid-crustal site of emplacement, without a contribution from mafic magmas. This explains the Labyrinth Mountain Th/U and REE patterns. The depth of emplacement will be addressed below in Section V.

IV
DEFORMATION AND MAGMA EMPLACEMENT

Fanning foliation

New mapping of the Labyrinth Mountain to Jove Peak study area reveal structural domains controlled largely by intrusion (Fig. 12). Structural-lithologic domains identified here include (1) a. the Mount Stuart batholith b. the Chiwaukum schist blocks or rafts in the batholith c. the Jove Peak orbiculite; (2) the Chiwaukum schist; (3) the Labyrinth Mountain pluton and southwestern sill, Kbgg; (4) Nason Ridge Migmatitic gneiss; (5) schist blocks or rafts in Kbgg bodies (Appendix A). Additionally, the Minotaur Lake fault crosses the study area through the Nason Ridge Migmatitic gneiss.

On a km-scale, NE-dipping dominant foliation becomes steeper (>60°) away from the Mount Stuart batholith until it is effectively vertical in the Nason Ridge Migmatitic gneiss (Fig. 12 and Fig. 13; Appendix A). Toward the contact with the Labyrinth Mountain pluton and within the pluton, foliation becomes less steep and dips SW, thus giving the impression of fanning foliation between the Labyrinth Mountain pluton and the Mount Stuart batholith (Fig. 25 below). An alternative interpretation projects a synformal axis parallel to the steepest foliation in the Nason Ridge Migmatitic gneiss (Fig. 12).

Available evidence suggests that differences in bulk rock composition in the Chiwaukum schist—for example, the difference between samples 03NC152 and 03NC19A (Table 6)— represent compositional layering parallel to the dominant NW-

	03NC152	03NC143	03NC19A
Weight %			
SiO2	50.19	66.06	63.86
Al2O3	30.07	14.56	16.10
CaO	1.26	2.65	1.91
MgO	3.77	2.65	2.72
FeO		5.68	6.33
Fe2O3	10.28	0.70	0.75
K2O	2.54	1.67	2.36
Na2O	1.67	2.89	2.13
MnO	0.17	0.13	0.15
TiO2	1.26	0.67	0.78
Cr2O3		0.01	0.02
P2O5	0.03	0.05	0.16
LOI	0.30	2.08	2.42
TOTAL	101.53	99.80	99.69
Mole % (normalized in the MnNCKFMASH system)			
SiO2	58.37	72.84	71.75
Al2O3	20.60	9.46	10.66
CaO	1.57	3.13	2.30
MgO	6.53	4.36	4.56
FeO	9.00	5.82	6.58
K2O	1.88	1.17	1.69
Na2O	1.88	3.09	2.32
MnO	0.17	0.12	0.14
Total	100.00	100.00	100.00

Table 6. Bulk compositions of pelitic samples used in thermodynamic modeling or geochronology.

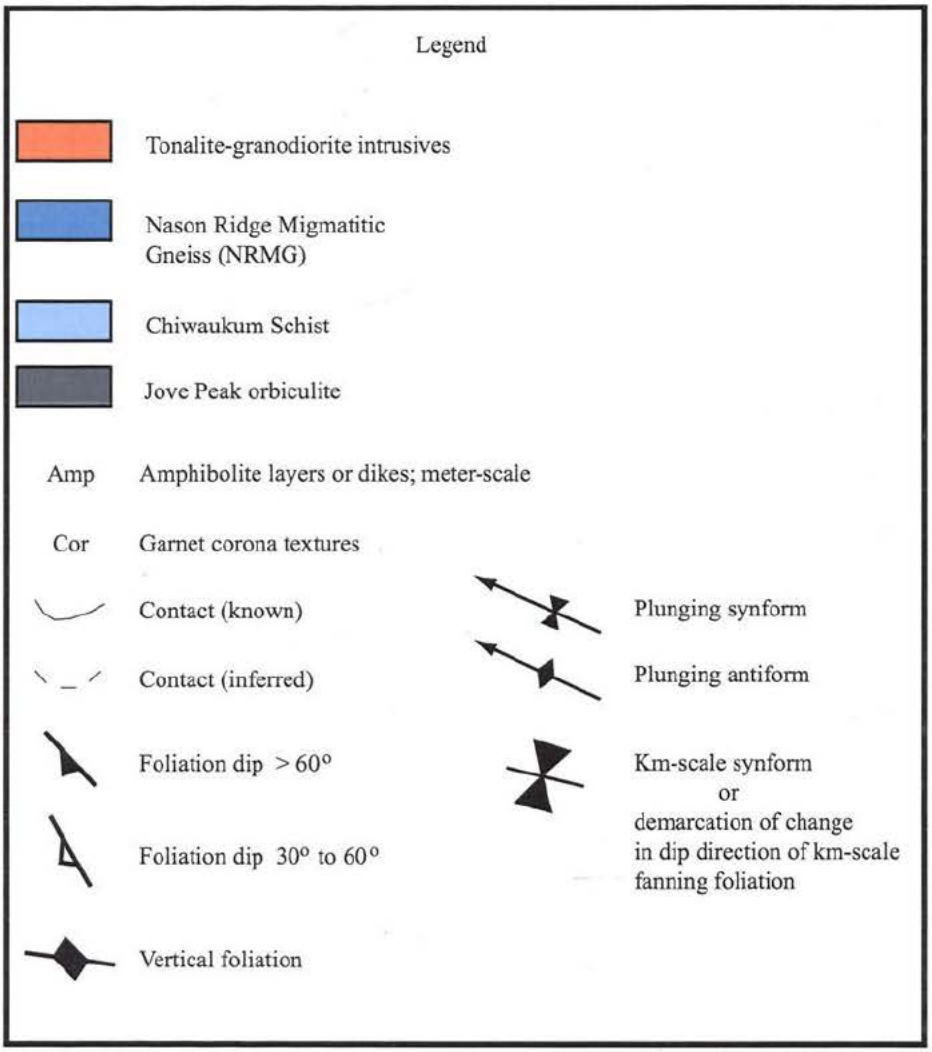

Figure 12. New mapping of the Labyrinth Mountain-Jove Peak area. Geologic units after Tabor et al. (1993). Jove Peak orbiculite after Van Diver (1968). Only representative folds, faults, foliation and schist rafts are shown.

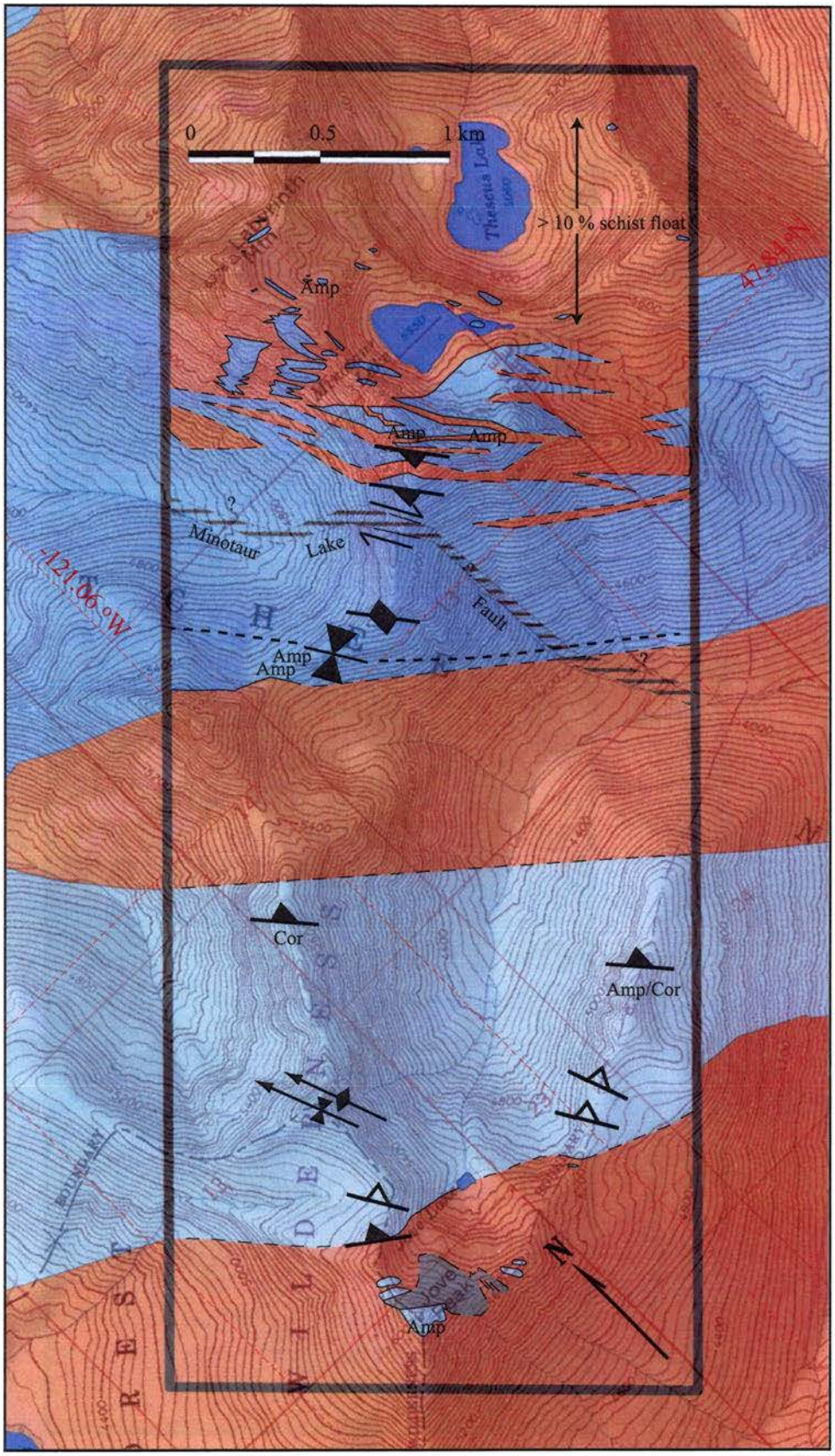
0
0.5
1 km
Theseus Lake
> 10 % schist float
Amp
Amp
Amp
Minotaur
Lake
Fault
Amp
Amp
Cor
Amp/Cor
Amp
-121.06 °W
47.84 °N

Figure 12.

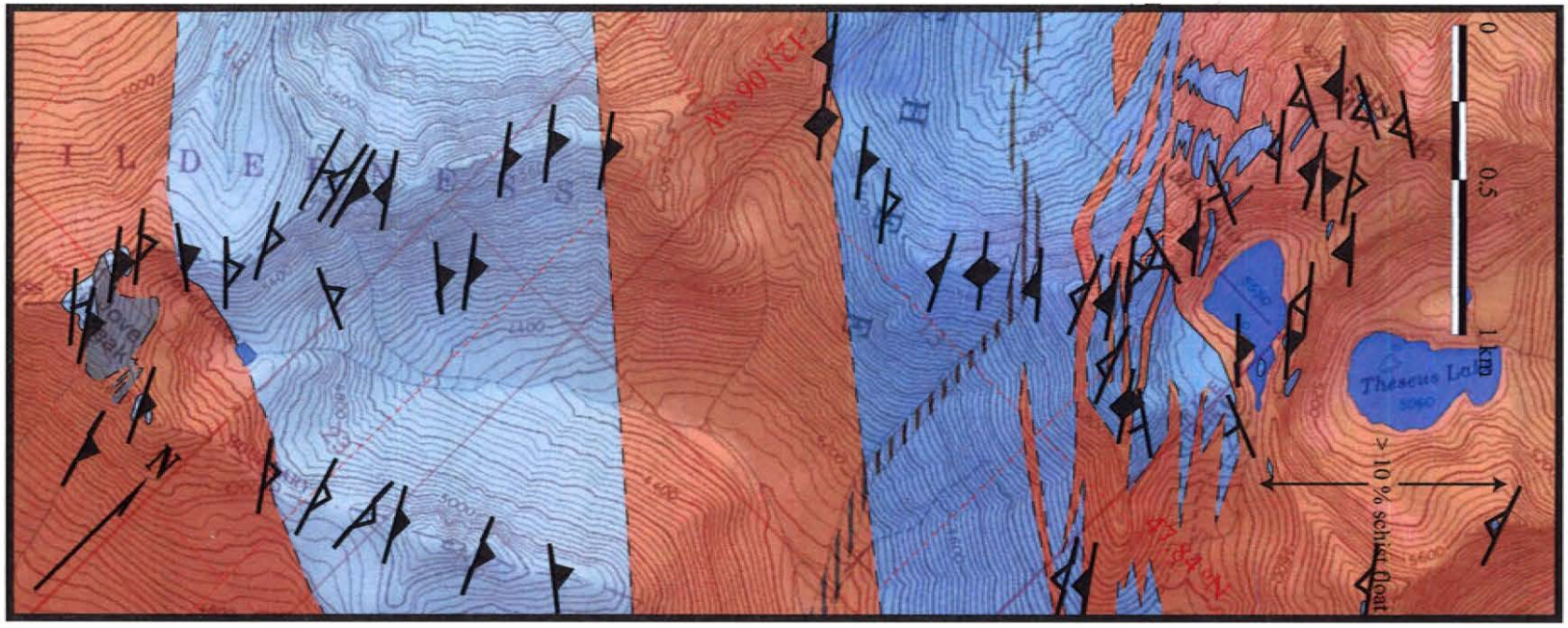

Figure 13. Map of representative foliations.
Dips less than 30° are denoted with tick marks; 30° to 60°, triangle outlines; and greater than 60o, filled triangles.
Data are provided in Appendix A; additional outcrop-scale foliation data are given in Table 7.

striking schistosity. Amphibolite dikes or lenses and garnet corona textures (e.g., Stowell and Stein 2005) observed as far apart as 1 km appear to correlate along strike (Fig. 12).

High temperature lineations (fold axes and mineral lineations) consistently trend NW-SE (Fig. 14). The majority plunge shallowly NW (Fig. 14; Table 7; Appendix A). These data are consistent with general trends and plunges of lineations on the NE side of the Mount Stuart batholith on a regional scale (Miller et al. 2005). Evidence for ductile dextral or sinistral orogen-parallel kinematics (e.g., Brown and Walker 1993) is ambiguous or entirely absent. Lineations are compatible with SE-NW extension and upright folding during NE-SW contraction (Miller et al. 2005).

Whereas lineations and foliations in the Nason Ridge Migmatitic gneiss and Labyrinth Mountain pluton are generally parallel to the contacts between intrusive bodies and schist, lineations and foliations in the Chiwaukum schist are acute to the contact with the Mount Stuart batholith (Fig. 13 and Fig. 14). Lineations proximate to the Mount Stuart batholith contact are rotated slightly N with respect to lineation in the Nason Ridge Migmatitic gneiss.

Local crosscutting relationships (Fig. 15 A) at the Mount Stuart batholith contact suggest that at least some foliation development pre-dated MS intrusion and that the dominant schistosity (S2) incompletely transposes the pre-existing schistosity (S1; Fig. 15 A). Close to the contact, axial planar schistosity (S2) is parallel to the contact. Possible syn- to post- Mount Stuart age SW-directed shearing is evidenced by asymmetric folding (Fig. 15 B). NE-side-up shearing in the Mount Stuart structural aureole has been documented (e.g., transposition cycle 5 in Paterson et al. 1994). An

04NCGB001 (Cylindrical Fold)

Fold Axis: 2--> 114 SE (from stereonet)

Strike	Dip*
120	71
308	54
295	56
293	62
293	62
291	62
280	40
113	62
125	23
99	55
304	51
305	63
101	60
252	7

*Right-Hand-Rule

04NCGB011 (Cylindrical Fold)

Fold Axis: 11--> 330 NW (from stereonet)

Strike	Dip*
162	48
160	49
270	24
326	90
335	29

*Right-Hand-Rule

Labyrinth Kbgg Qtz+Pl Dike Data

Strike	Dip*
129	11
72	83
81	78
155	4
256	90
85	53
260	12
212	36
68	77
265	70

*Right-Hand-Rule

Table 7. Outcrop-scale structural data.

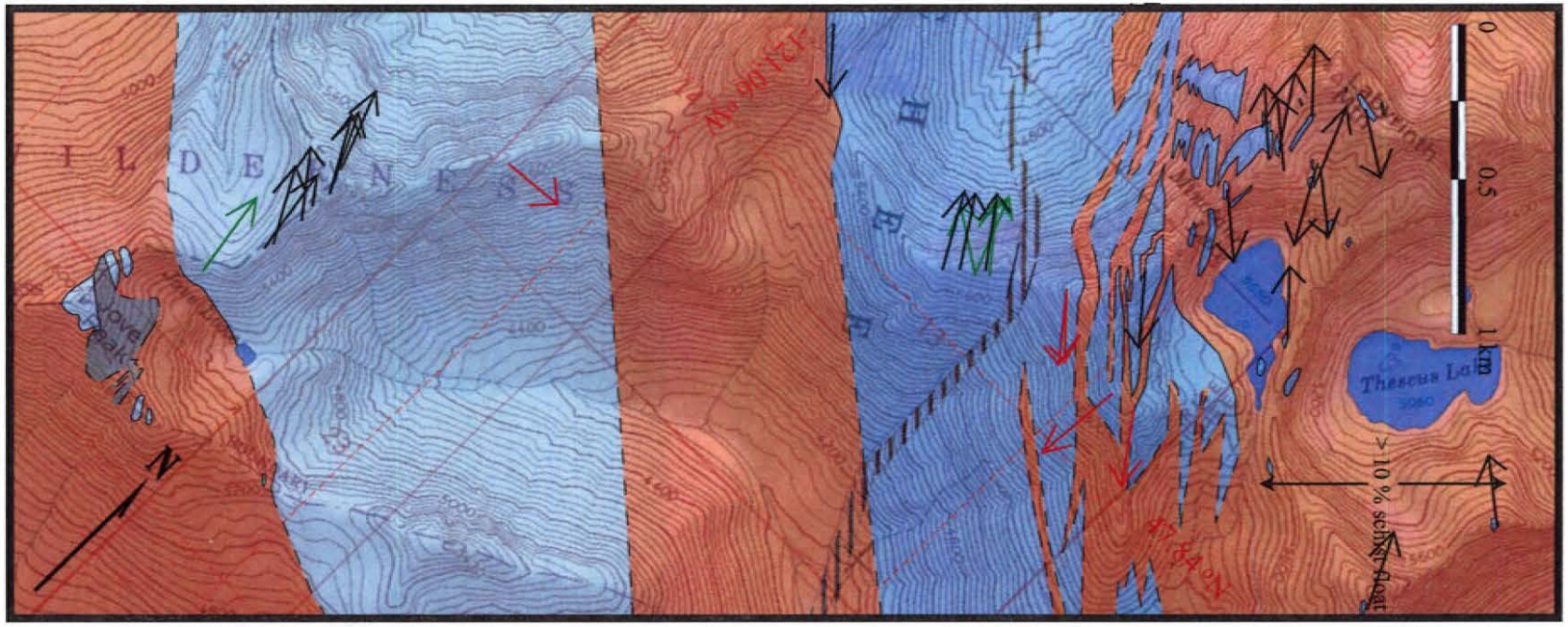

Figure 14. Map showing high temperature lineations. Fold axes with plunges less than 30° (black arrows); fold axes with plunges greater than or equal to 30° (green arrows); mineral lineations (red arrows). All trend and plunge data are provided in Appendix A.

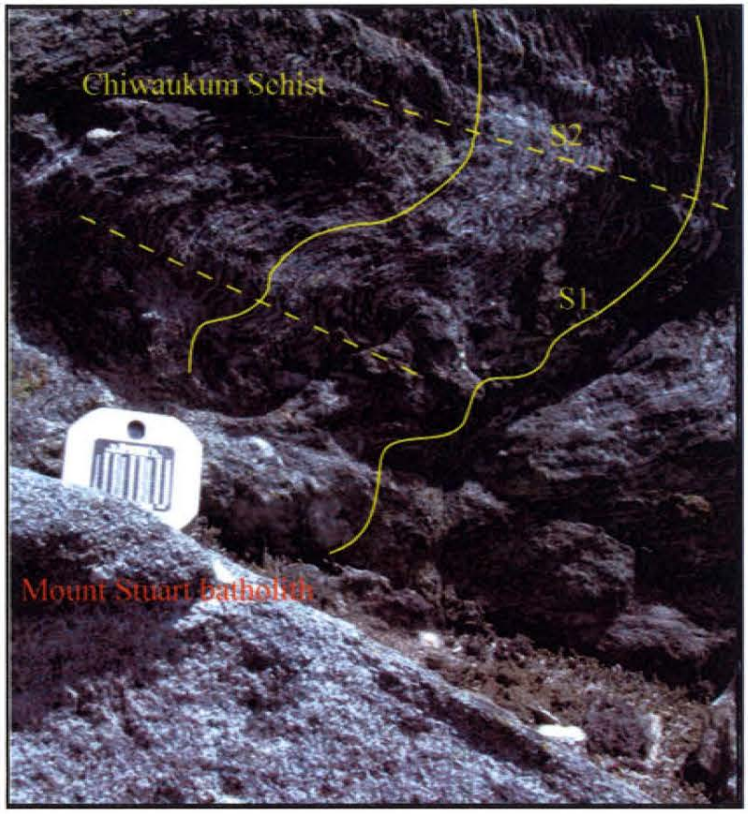

A.

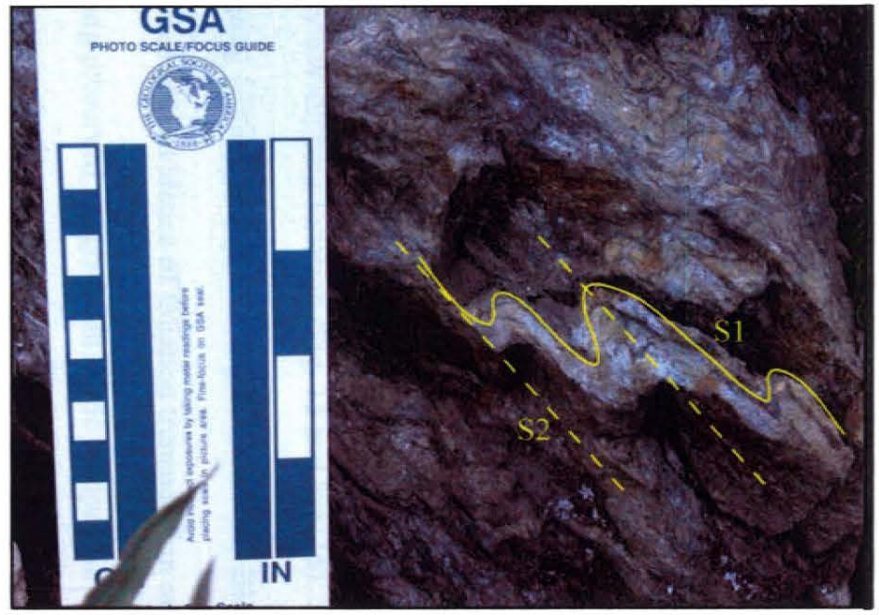

B.

Figure 15. The Mount Stuart batholith structural aureole. A) Location 04NCGB017. Non-foliated Mount Stuart batholith truncates an earlier schistosity (S1) and shows contact parallelism with moderately NE-dipping axial surfaces (S2) that may have developed syn- and post- emplacement of the batholith. B) Location 04NCGB014. An earlier gneissic foliation (S1) is transposed into a moderately NE-dipping axial planar foliation. Cylindrical intrafolial folds show asymmetry consistent with NE-side-up shearing.

absence of recognizable shear zones in the Jove Peak region makes significant NE-side-up shearing unlikely, however.

Outside of a ½ km structural aureole NE of the Mount Stuart batholith characterized by SW-directed shearing and moderately NE-dipping incompletely transposed gneissosity and schistosity, foliation rolls over into a steep, near-vertical pervasive schistosity (S2) via a decameter-scale antiform-synform couple (Fig. 13). This foliation in the Chiwaukum schist continues on the NE side of the interceding SW granodiorite sill, such that the Nason Ridge Migmatitic gneiss is characterized by near vertical and steeply SW-dipping foliation (Fig. 13 and Fig. 16). On a regional scale, this pervasive SW-dipping fabric is uncommon in the Wenatchee Block (Fig. 16). And on the outcrop-scale, there is little evidence of foliation transposition or shearing; this domain is interpreted as having preserved a high-strain fabric compatible with NE-SW contraction.

A magma emplacement model

Miller and Paterson (2000) proposed that intrusions in the Cascades crystalline core can be assigned to two categories: 1) variably discordant dikes of all sizes, and 2) elliptical visco-elastic diapirs (Miller and Paterson 1999). The Labyrinth Mountain-Jove Peak area may preserve examples of both types of intrusions. This section will focus on the kilometer-scale elliptical plutons or sills, and the next section will describe the sheeted intrusives that constitute the Nason Ridge Migmatitic Gneiss between the two elliptical plutons.

Elliptical plutons within the Cascades crystalline core are generally sills parallel to the pervasive NW trending foliation and were likely emplaced during arc-normal

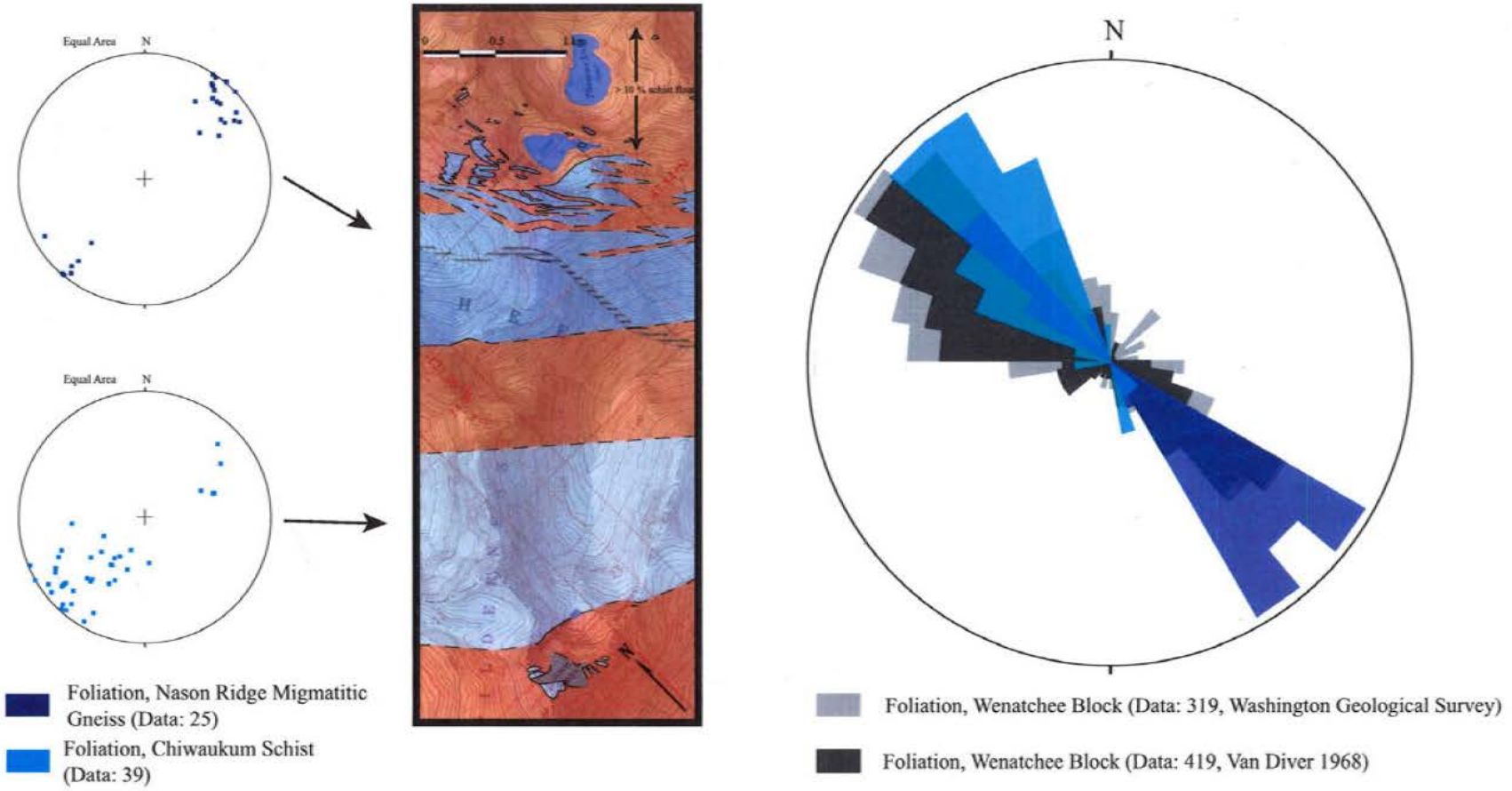

Figure 16. Comparison of Chiwaukum Schist and Nason Ridge Migmatitic Gneiss foliations. Equal area stereonet plots show poles to foliation. Rose diagrams compare strike orientations, using right-hand-rule convention for dip direction, for the Nason Ridge Migmatitic Gneiss and the Chiwaukum Schist from thestudy area with undifferentiated foliation data from the entire Wenatchee block (data from Van Diver 1968; Tabor et al. 1987; Tabor et al. 1993).

contraction (Miller and Paterson 1998; Paterson and Miller 1999). Plutons throughout the core preserve various stages and vertical levels of emplacement summarized below (after Miller et al. 2000):

1) Mantle-derived mafic sheets intrude parallel to subvertical axial surfaces of upright folds and, thus, normal to the maximum shortening direction. Host rock fabrics are steepened and shortened in narrow structural aureoles normal to the intruding sheets.

2) More evolved crustally-derived tonalite and granodiorite magmas ascend along these heated pathways and displace the older mafic sheets. Increasingly wider magmatic sheets coalesce, thereby creating rafts of host rock and earlier mafic dikes which are displaced downward.

3) Finally, emplacement of large volumes of homogenous tonalite is accommodated by stoping along the pluton margins.

Whereas deeper-seated plutons may preserve mafic sheets along their margins, shallower level extensions of these plutons may reveal only late-stage tonalites derived from higher volumes of crustal melt. Pathways heated by earlier and deeper tonalite and mafic sheets facilitate both the upward migration and chemical and physical homogenization of shallower level plutons (Miller et al. 2000).

Chemical and physical homogenization of crustal melt and mantle-derived mafic magmas in shallower level plutons has been proposed to account for the geochemical signature and for the absence of discrete compositional sheets throughout much of the Mount Stuart batholith (Section III; Paterson et al. 1994; Miller et al. 2000). At Jove

Peak (Fig. 12), detailed mapping and three-point calculations for the contact (296/62 NE) between the Mount Stuart batholith and the Chiwaukum schist reveal a slight discordance (10-20°), which is supported by outcrop scale observations that show incomplete transposition of an earlier foliation into parallelism with the contact (see foliation section). This discordance, the sharpness of the Mount Stuart batholith-Chiwaukum schist contact (Fig. 12), and the geochemical evidence all suggest that the Mount Stuart batholith was emplaced a shallow crustal levels corresponding to the epizone depth zone (Buddington 1959).

The granodiorite sill nearer to the Mount Stuart batholith trends NW in map view and exhibits a 4:1 length-to-width ratio (Fig. 2). The contact between the southwestern granodiorite sill and the Chiwaukum schist and Nason Ridge migmatitic Gneiss is concordant and sharp (Fig. 12 and Fig. 13). Foliation is nearly vertical in the host schist, and only a weak near-vertical fabric is preserved in the sill. These observations are ambiguous as depth zone criteria, but the absence of a recognizable contact aureole (Section V) suggests a mesozonal emplacement level.

The contact between the Nason Ridge Migmatitic Gneiss and the Labyrinth Mountain pluton, on the other hand, is gradational (Fig. 12). The Labyrinth Mountain pluton similarly trends NW with a 3:1 length-to-width ratio, perpendicular to the Late Cretaceous shortening direction (Fig. 2). Such concordant gradational contacts are often associated with deeper-seated catazonal emplacement, where the host rock is ductile and already at amphibolite facies conditions or above. The Labyrinth Mountain may exemplify processes attributed to deeper mid- to late-stage visco-elastic diapirs (Miller and Paterson 1999; Miller et al. 2000).

The preservation of map-scale to outcrop-scale host-rock schist xenoliths in the Labyrinth Mountain pluton implies that magma ascent and chamber expansion were active during final solidification (Fig. 12; Miller and Paterson 1998). The distribution, deformation and intrusion experienced by these rafts may be important to understanding magma emplacement processes in the Labyrinth Mountain pluton. Of particular note is that rafts occur not only in the gradational contact, where they are clearly associated with wall-rock, but also throughout the center of the pluton with volumes locally >10% (Fig. 12). No record of raft settling, however, is recorded in the granodiorite fabric. Analogous observations by Miller and Paterson (1998) in the Mount Stuart batholith led them to conclude that crystallizing magmas are poor recorders of subsolidus strain.

Both subvertical and subhorizontal rafts trend parallel to Nason Ridge Migmatitic Gneiss wall-rock contacts, and they are concordant with weak foliation in the Labyrinth Mountain granodiorite (Figs. 15, 16 and 21). Similarly oriented fold axes in subvertical and subhorizontal rafts (Fig. 17) indicate a lack of rotation about a NE-SW axis during stoping or disaggregation of the rafts from wall-rock. However, it is unlikely that rafts are simply pendants that preserve host rock foliation and fold attitudes; in steep cross-sectional exposures, rafts are separated vertically from one another or free-floating in granodiorite. Instead, rotation about a NW-SE axis could explain steepening of foliation (Fig. 17 and Fig. 18) in subvertical rafts. Or, alternatively, less steeply-dipping rafts and their subhorizontal foliation may represent late-stage roof blocks that did not experience the intense wall-rock deformation and intrusion characteristic of more vertical rafts. This is supported by the observation that subhorizontal rafts more common distal from the contact (Fig. 25) and that subhorizontal rafts often preserve earlier folding where high

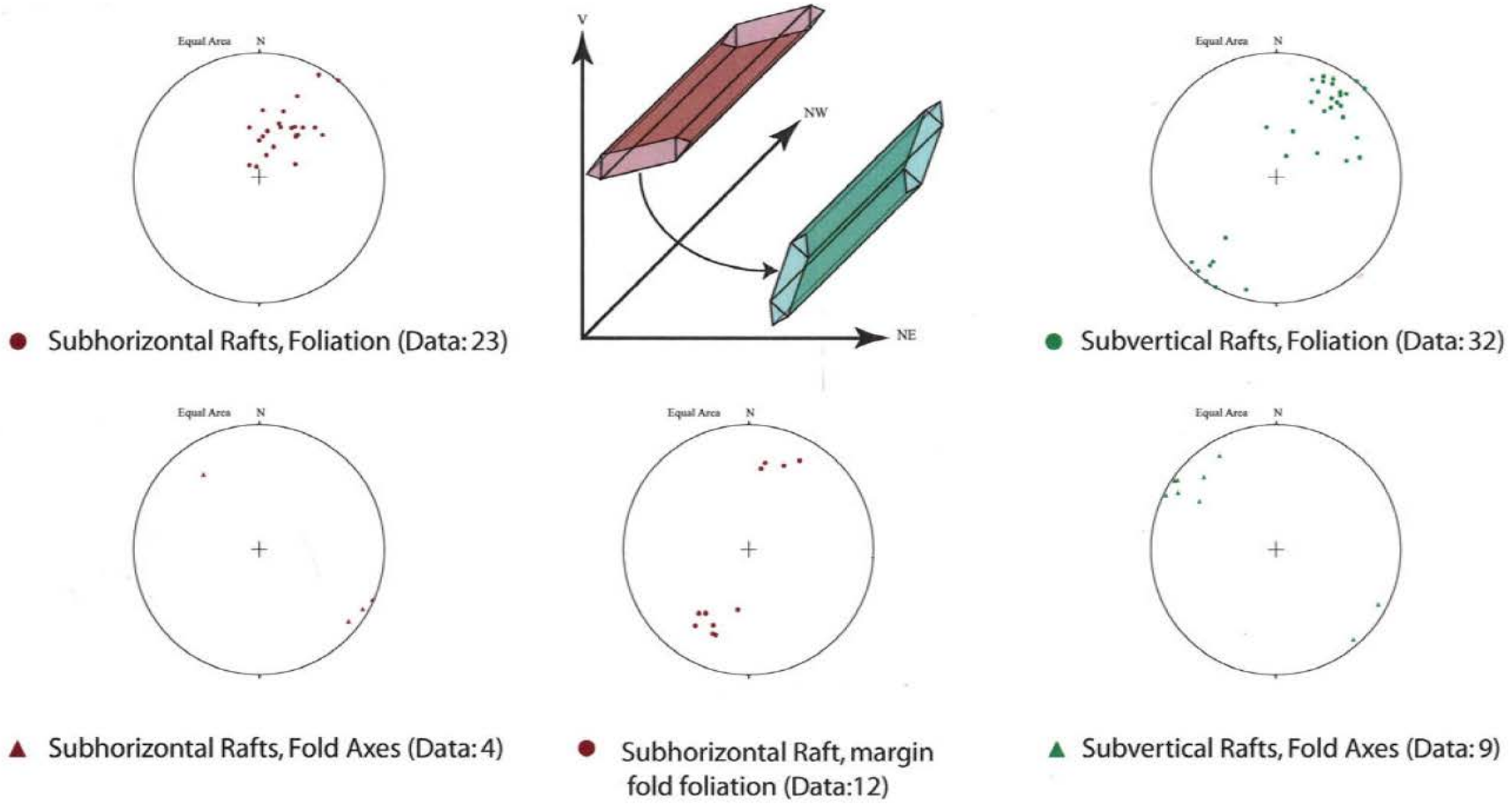

Figure 17. Raft foliations and fold axes. Equal area stereonet plots showing poles to foliation and trends and plunges of fold axes for Chiwaukum Schistxenolith rafts in the Labyrinth Mountain granodiorite pluton (Kbgg). The schematic diagram (top and center) displays estimated aspect ratios for raft dimensions as well a rotation component which likely contributed to the observed data. Bottom and center: fold foliation orientations from the intruded margin of a subhorizontal raft.

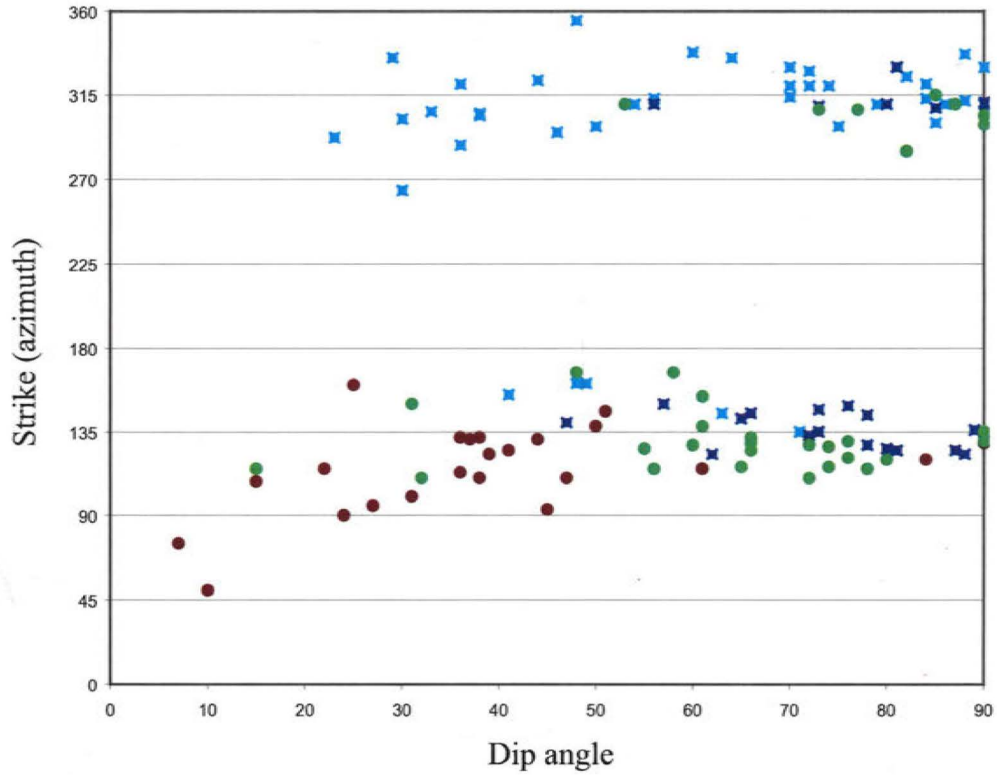

Figure 18. X-Y plot foliation comparisons. Variations in strike orientation as a function of dip angle and structural-lithologic zone. Chiwaukum Schist, CS (pale blue squares); Nason Ridge Migmatitic Gneiss, NRMG (dark blue squares); Subhorizontal CS rafts (dark red circles) and subvertical CS rafts (dark green circles) in the Labyrinth Mountain granodiorite pluton, Kbgg.

temperature deformation, partial melting and granodiorite intrusion did not obliterate the evidence (Fig. 20C). These rafts were essentially armored by more competent granodiorite after magma crystallization (Fig. 20C) and, consequently, were shielded from subsequent deformation.

Subvertical rafts show intense folding, intrusion and partial melting textures (Fig. 19 and Fig. 20). Intrusive granodiorite apophyses both crosscut foliation in rafts and are folded with foliation (Fig. 20), suggesting that foliation development in the rafts was pre- and syn-intrusion. The margins of larger rafts are far more intruded, and isolated schlieren are common in the vicinity of smaller and larger rafts. Co-existing boudinage and folding of granodiorite stringers in these rafts are compatible with NE-SW contraction (Fig. 19 and Fig. 20). Cuspate-lobate mullion structures on the margins of rafts and boudinaged intrusives (e.g., Fig. 19) provide evidence that the granodiorite was more competent than the schist during deformation. This supports an interpretation of high temperature deformation in the schist rafts during the final stages of magma crystallization.

Many of the earlier, foliation-parallel intrusives could have played an important role in wall rock disaggregation, although these pilot sheets were widened by later pulses of magma and are no longer identifiable, as in Miller et al. (2000). Such a process is preserved in the gradational contact between the Nason Ridge Migmatitic Gneiss (NRMG) and the Labyrinth Mountain pluton (Fig. 12). As sheets of granodiorite intruded the host schist, rafts may have initially fractured and separated from the wall-rock, as is telegraphed where granodiorite sills and dikes wedge apart massive NRMG schist blocks in the gradational contact. Enduring the latent heat of crystallization and

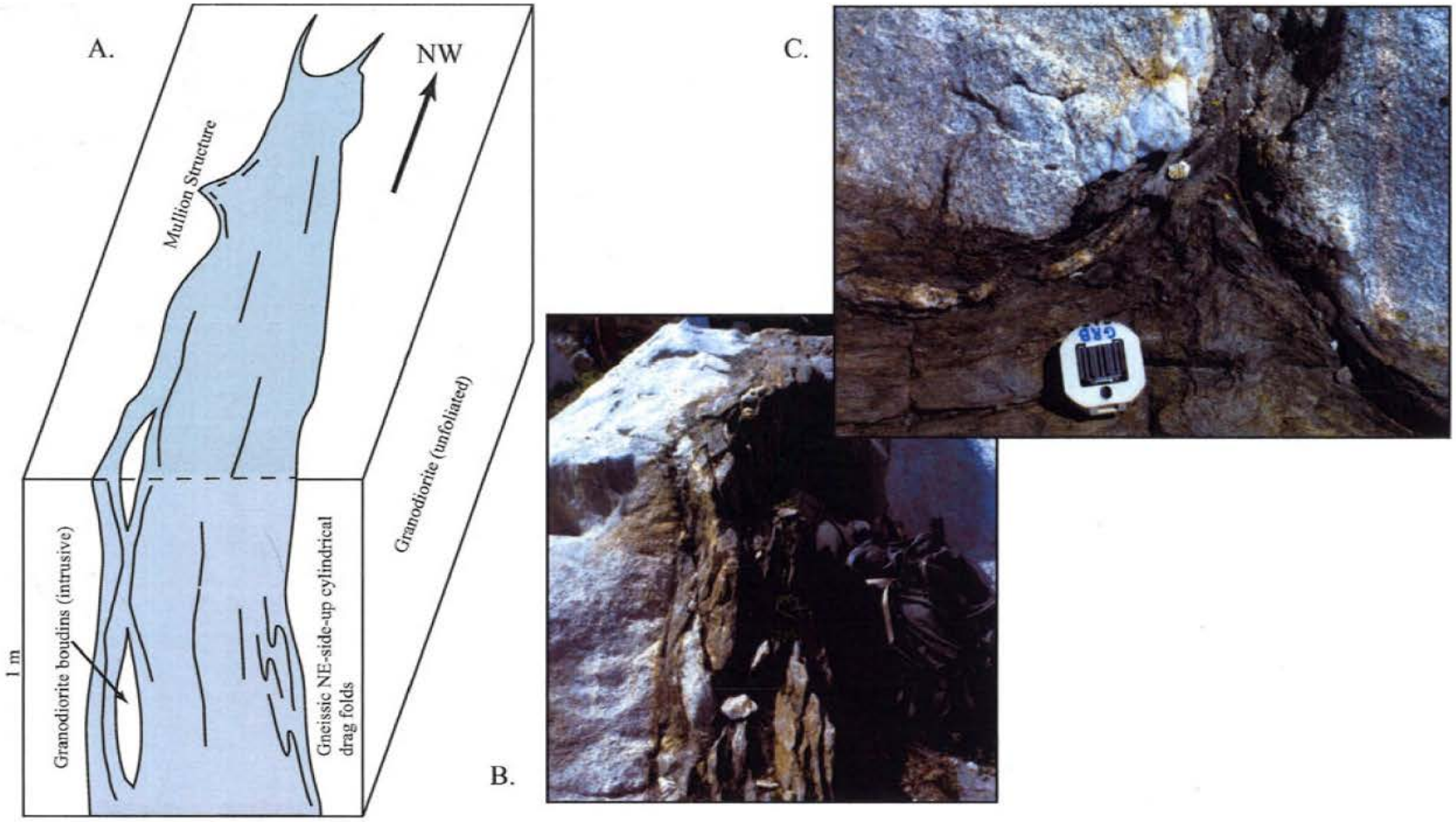

Figure 19. Location 03NCGB126/04NCGB027. Subvertical schist raft in the Labyrinth Mountain granodiorite pluton (Kbgg). A) Outcrop sketch. Note the cm-scale gneissic intrafolial drag folds on the NE side of the raft. Foliation is nearly vertical and strikes NW-SE. Fold axes plunge shallowly SE. B) Photo of raft looking NW. Biotite in the intrusive boudins is parallel to foliation in the raft. C) Top view of mullion structure. The cusp points into the granodiorite, indicating that the schist was less competent at the time of deformation.

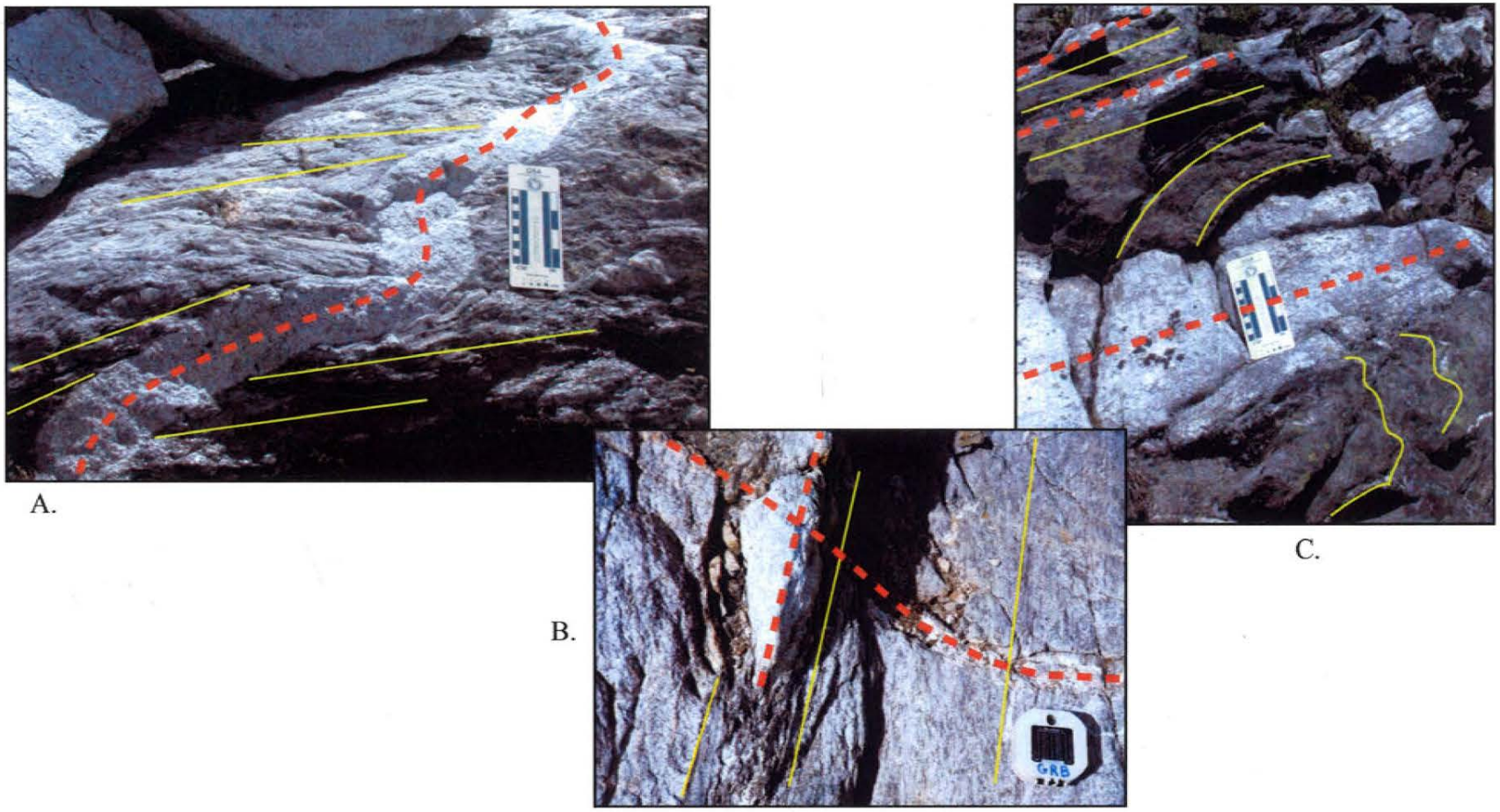

Figure 20. Raft structures. Intrusion and deformation in schist rafts in the Labyrinth Mountain granodiorite pluton. A) Location 04NCGB001. Granodiorite dike crosscuts schist foliation and is folded. B) Location 03NCGB157. Granodiorite stringer intrudes raft parallel to foliation and is boudinaged. A thin coarse quartz-plagioclase dike crosscuts both schist foliation and the intrusive stringer. C) Location 04NCGB002. Compositionally and texturally similar granodiorite sheets intrude parallel to and crosscut schist foliation.

additional intrusion, larger rafts may have begun to suffer ductile disaggreagation. During continued inflation of the pluton, granodiorite apophyses and host thermally weak schist rafts may have experienced greater strain as the pluton exerted increasing stress on the wall rocks. Such magma generated strain rates in pluton structural aureoles can be quite rapid and have been documented for the Mount Stuart batholith (Albertz, Paterson and Okaya 2005). Because granodiorite sheets were likely exploiting pathways parallel to foliation, the stress they exerted would have locally augmented regional stress fields associated with arc-normal SW-NE contraction. Thus, rafts would have rotated into alignment with local foliation and wall-rock contacts according to their shape. Raft shape is primarily controlled by foliation surfaces along which rafts separated from the wall-rock (Fig. 17 and Fig. 12); hence, rafts may have ultimately maintained their original orientation and been translated away from the pluton margins and vertically up or down as a function of magma flow and magma-raft viscosity differences.

The Nason Ridge Migmatitic Gneiss

The second type of intrusion characteristic of the Cascades Crystalline core, according to Miller et al. (2000), includes variably discordant dikes of all sizes. The Nason Ridge Migmatitic Gneiss (formerly called the Banded Gneiss, Tabor et al. 2002; Fig. 1B and Fig. 2) is a variably intruded and partially melted derivative of the Chiwaukum Schist (Tabor et al. 1993; Zuluaga 2004). The amount of leucocratic igneous material comprising the Gneiss—including light-colored dikes, veins and quartz-plagioclase lenses from partial melts—ranges from 10-99% (Tabor et al. 1993; Zuluaga 2004).

The Nason Ridge Migmatitic Gneiss between the southwestern Kbgg sill and the Labyrinth Mountain pluton is composed of 20-30% intrusives (Fig. 23 and Fig. 24). These are foliated and non-foliated mica tonalite and mica granodiorite, garnet-biotite tonalite, garnet-biotite aplite and pegmatite (Fig. 21, 23 and 24). Intrusive sheets are variably concordant, discordant, folded, boudinaged and undeformed. Dikes range in size from several centimeters to one meter, whereas sills are as wide as 10 meters (Fig. 21). As might be expected, the larger sills are granodiorite and closer to the contact with the Labyrinth Mountain pluton. Where schist blocks become distinct from wall-rock in the gradational contact between the NRMG and the pluton, granodiorite is viewed as part of the main pluton or a pluton margin sheet rather than a sill. The difference is semantic; important, however, is the mapped continuation between the main pluton and granodiorite sills in the NRMG (Fig. 12 and Fig. 25). These granodiorite sills also share a structural and petrographic identity with the main phase of the Labyrinth Mountain pluton (Fig. 21 and Fig. 22; Appendix B), and, therefore, reveal the source of a locally major exogenous contribution to the NRMG. Assuming the granodiorite sills are also the same age as the main pluton, the NRMG in this area was intruded and deformed around 90.6 ± 2.4 Ma.

Larger granodiorite sills in the NRMG are generally nonfoliated or weakly foliated, similar to the Labyrinth Mountain pluton. Smaller granodiorite intrusives are more likely to show discordance with the dominant schist foliation and are internally foliated or nonfoliated. Examples of folded and boudinaged granodiorite-tonalite dikes that lack internal foliation suggest that these dikes were more competent than the schist during deformation (e.g., Fig. 24). Furthermore, these dikes are not differentiable from

Location	Zone	Mineralogy	Category	Width (m)	Strike		Dip	Structural
03NCGB124	5	See photo and sample	Dike		300	75	NE	Cross cuts and intrudes fol of CS raft
03NCGB125	3	Qtz+Pl (coarse) see photo	Dike	0.06	308	49	NE	At CS raft and Kbgg contact
03NCGB128	3	Qtz+Pl (coarse)	Dike	0.12	55	66	SE	Crosscuts Kbgg
03NCGB134	5		Pegmatite Dike	0.5	140	50	SW	Crosscuts CS raft fol
03NCGB159	3	Qtz+Pl (coarse)	Dike	0.06	138	8	SW	Crosscuts Kbgg
03NCGB159	3	Qtz+Pl (coarse)	Dike	0.06	265	70	NW	Crosscuts Kbgg and CS raft
03NCGB159	3	Qtz+Pl (coarse)	Dike	0.06	79	77	SE	Crosscuts Kbgg
04NCGB006	2	MS quartz diorite?	Dike	0.08	12	61	E	Crosscuts CS raft fol
04NCGB025	4	Qtz+Pl+Bt (med)	Dike	0.4	219	48	NW	Crosscuts NRMG schist fol; contains internal discordant fol (240/23 NW)
04NCGB027	4		Pegmatite Dike	0.03	52	70	SE	Crosscuts Kbgg
04NCGB027	4		Pegmatite Dike	0.04	258	49	NW	At termination: splays and assimilated by host biotite Kbgg
04NCGB028	3	Qtz+Pl (med)	Dike	0.04	265	45	N	Crosscuts biotite Kbgg
04NCGB028	3	Qtz+Pl (coarse)	Dike	0.03	153	45	SW	Crosscuts biotite Kbgg
04NCGB035	4	Qtz+Pl+Bt (med-coarse)	Dike	0.15				Crosscuts schist fol and Qtz+Pl+Grt+Bt (fine) sill; wraps into parallelism with schist fol and boudinaged; med grained core; coarse margins

Figure 21. Iintrusive dikes and sills. Descriptions including widths and cross-cutting relationships. Zone refers to lithologic domain: (2) Chiwaukum schist; (3) granodiorite intrusive bodies, Kbgg; (4) Nason Ridge Migmatitic Gneiss; (5) Schist blocks/rafts in Kbgg bodies.

Location	Zone	Mineralogy	Category	Width (m)	Strike	Dip		Structural
04NCGB035	4		Pegmatite Dike	0.8	331	90	V	Crosscuts NRMG schist fol
04NCGB036	4	Qtz+Pl+Ms+Bt (med-coarse)	Dike	0.5	N-S			Crosscuts schist fol and Qtz+Pl+Bt (med) sill; folded; Ms locally parallel to host schist fol
04NCGB036	4		Pegamtite Dike	0.2	319	90	V	Crosscuts Qtz+Pl+Bt (med) sill; coarser core
04NCGB036	4	Qtz+Pl+Bt (med)	Dike	0.5	330	86	NE	Crosscuts schist fol; internal Bt margin parallel fol
04NCGB036	4		Pegamtite Dike	0.1	285	46	NE	Crosscuts Qtz+Pl+Bt (med) sill; coarser core
04NCGB037	4	Qtz+Pl+Bt+Grt see "14"	Dike	0.08	184	57	W	Crosscuts schist fol
04NCGB037	4	Qtz+Pl+Ms (fine) see "9"	Dike	0.3	115	81	SW	Crosscuts schist fol and Qtz+Pl+Bt (med)
04NCGB038	5		Pegmatite Dike	0.2	75	80	SE	Crosscuts Kbgg (med)
04NCGB048	4	Qtz+Bt+see sample	Dike	0.1	326	90	V	Crosscuts NRMG schist; crosscut by Qtz+Pl+Ms dike
04NCGB051	3	Qtz+Pl+Bt (fine)	Dike	0.05	275	55	NE	Crosscuts Kbgg (med)
04NCGB051	3	Qtz+Pl+Bt (fine)	Dike	0.07	105	77	SW	Crosscuts Kbgg (med)
04NCGB052	3	Qtz+Pl (fine)	Dike	0.06	195	46	SW	Crosscuts Kbgg (med)
04NCGB052	3		Pegmatite Dike	1	305	75	NE	Crosscuts Kbgg (med)

Figure 21.

Location	Zone	Mineralogy	Category	Width (m)	Strike		Dip	Structural
04NCGB052	3	Qtz+Pl+Kfs (coarse)	Dike	0.05	114	83	SW	Crosscuts Kbgg (med)
04NCGB053	3	Qtz+Pl+Ms (coarse)	Dike	0.05	189	68	W	Crosscuts Kbgg (med)
04NCGB053	3	Qtz+Pl+Ms (coarse)	Dike	0.05	40	70	SE	Crosscuts Kbgg (med)
04NCGB054	3	Qtz+Pl+Ms+Grt (coarse)	Dike	0.04	67	70	SW	Crosscuts Kbgg
04NCGB055	5	Qtz+Pl+Grt+Bt (coarse)	Dike	0.3	316	80	NE	Crosscuts CS raft fol; folded
04NCGB056	5	Qtz+Pl+Grt+Bt (fine-med)	Dike	0.5	120	65	SW	Contact of 30 m CS raft
04NCGB062	3		Pegmatite Dike	1	53	90	V	Contact b/t CS raft and Kbgg
04NCGB065	3	Qtz+Pl+Ms (med)	Dike	0.04	117	57	SW	Crosscuts Kbgg
04NCGB065	3	Qtz+Pl	Dike	0.06	74	49	SE	Crosscuts Kbgg
04NCGB026	4	Qtz+Pl (coarse)	Sill	0.02	142	65	SW	Parallel to weak Kbgg fol
04NCGB026	4	Qtz+Pl (coarse)	Sill	0.02	118	90	V	Parallel to weak Kbgg fol
04NCGB035	4	Qtz+Pl+Bt (med)	Sill	10	133	72	SW	Non-foliated Kbgg
04NCGB035	4	Qtz+Pl+Bt+Grt (fine); sample A	Sill	0.2	320	73	NE	2 cm Qtz+Pl+Bt (med) along NE margin of sill
04NCGB035	4	Qtz+Pl+Bt+Grt (fine); sample B	Sill	0.15	127	77	SW	Crosscut by Qtz+Pl+Bt (coarse) folded dike
04NCGB036	4	Qtz+Pl+Bt (med)	Sill	0.3	125	81	SW	Crosscut by Qtz+Pl+Ms+Bt (coarse) folded dike; moderate foliation
04NCGB036	4	Qtz+Pl+Bt (med)	Sill	0.75	129	84	SW	Crosscut by Qtz+Pl+Ms+Bt (coarse) folded dike; foliated
04NCGB036	4	Qtz+Pl+Bt (med)	Sill	1.5	136	85	SW	Weak margin parallel foliation
04NCGB048	4	Qtz+Pl+Ms (coarse)	Sill	1.2	121	78	SW	Qtz+Pl+Bt+Ms (med)

Figure 21.

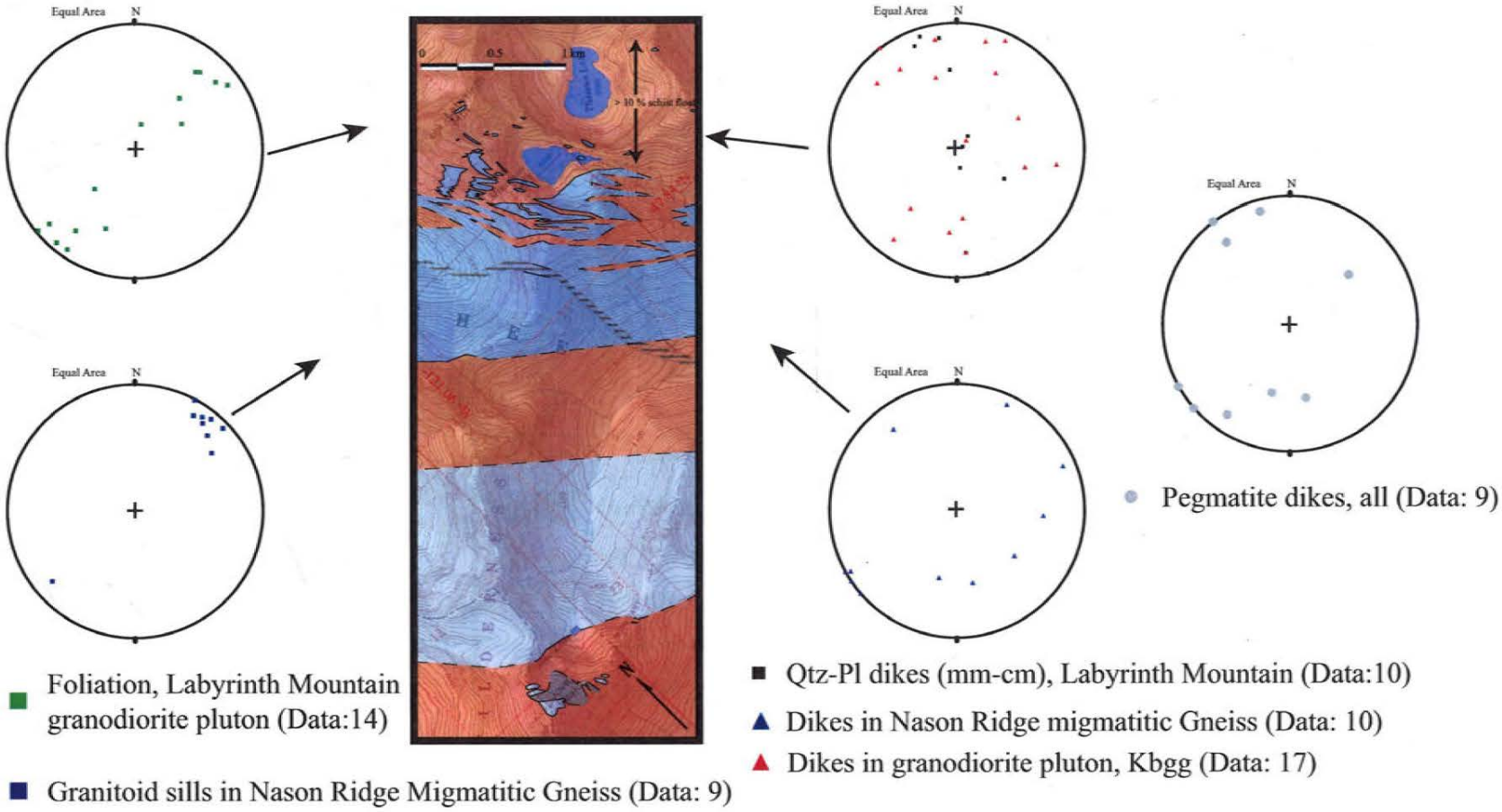

Figure 22. Stereonet plots of intrusives. Equal area stereonet representations of poles to planes for sills and dikes in the Labyrinth Mountain granodiorite pluton (Kbgg) and in the Nason Ridge Migmatitic Gneiss (NRMG). Data for weakly-defined biotite foliation in the granodiorite pluton are provided for comparison.

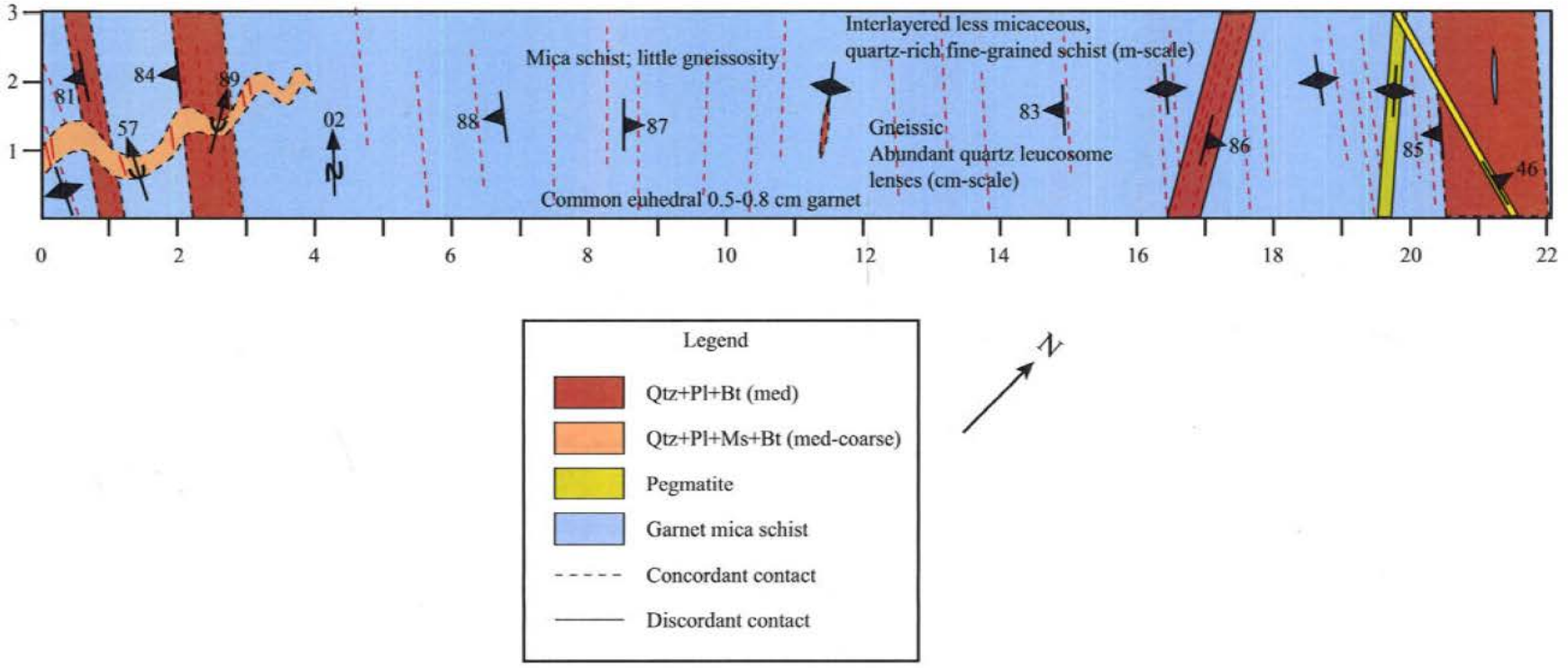

Figure 23. Outcrop Map: Nason Ridge Migmatitic Gneiss, 04NCGB036. Facing 315 NW. Scale in meters.

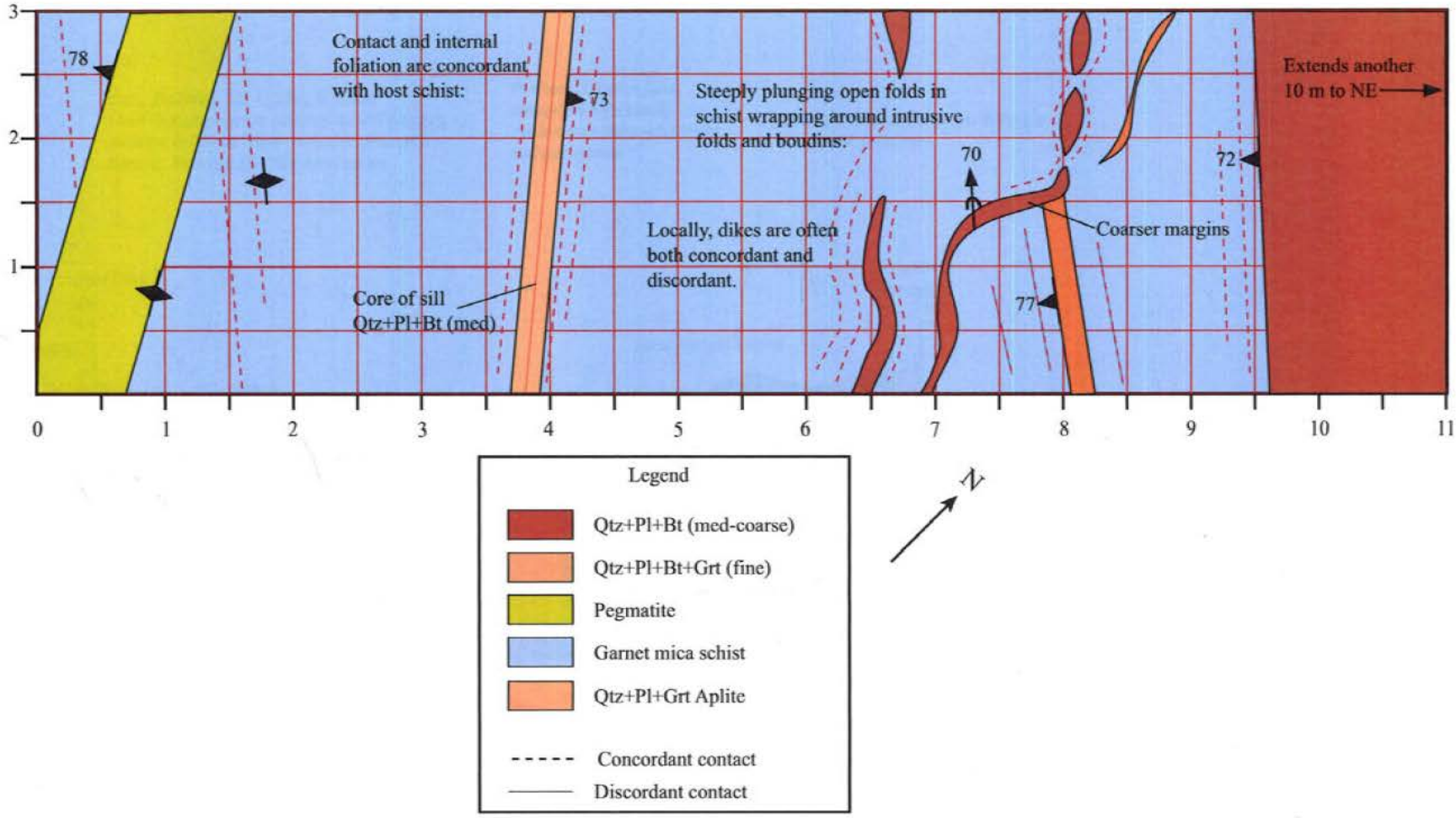

Figure 24. Outcrop Map: Nason Ridge Migmatitic Gneiss, 04NCGB035. Facing 315 NW. Scale in meters.

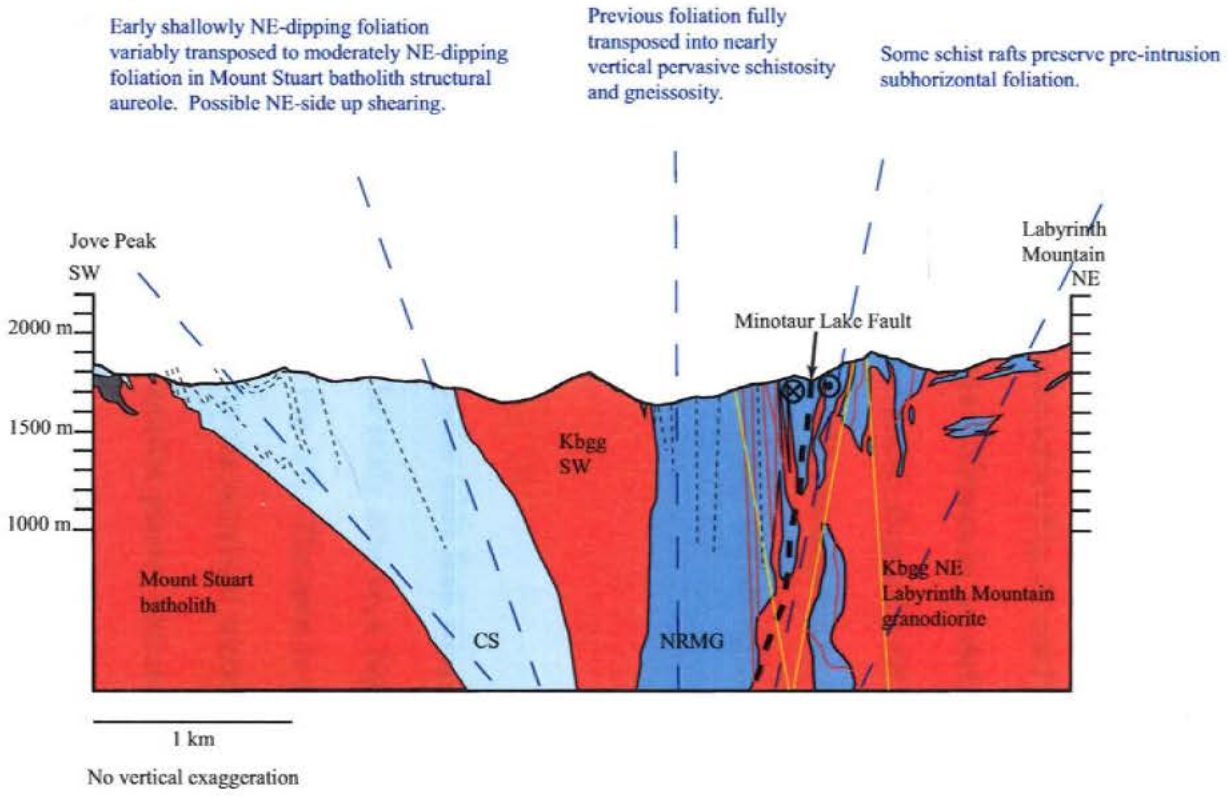

Figure 25. Structural cross section from Jove Peak to Labyrinth Mountain.

dikes measured within the pluton (Fig. 22). This evidence is compatible with observations of intrusive stringers in schist rafts in the Labyrinth Mountain pluton and supports the argument that significant intrusion and deformation may have occurred in the rafts while they were either still connected to the wall-rock schist.

Less abundant granitoid dikes crosscut foliated and nonfoliated granodiorite-tonalite sills (Fig. 21 and Fig. 23), indicating that intrusion of the NRMG continued after intrusion of concordant granodiorite-tonalite sheets. Cross-cutting dikes are often folded and internally foliated consistent with the dominant schist foliation and compatible with NE-SW contraction. Fold axes and boudin-neck lineations in crosscutting folded dikes are steep in comparison to fold axes in adjacent schist (Fig. 23 and Fig. 24; Appendix A). This plunge difference can be explained by the difference in pre-deformational orientation between the crosscutting dikes and schist. Pegmatite dikes crosscut existing schistosity in the NRMG, granodiorite-tonalite sills and foliation in the Labyrinth Mountain pluton (Fig. 21 and Fig. 22), suggesting they are among the latest intrusives in the study area (Fig. 25).

Minotaur Lake Fault

A previously unmapped broad 50-80 meter wide fault zone, hereafter referred to as the Minotaur Lake Fault, is exposed in the study area on a high NE-trending ridge southwest of the Labyrinth Mountain pluton (Fig. 27). The zone is composed of strongly foliated and discretely faulted schist parallel to the dominant schistosity in the NRMG, intensely brecciated schist and granodiorite-tonalite gneiss, and cataclasite; two black pseudotachylyte veins, 1 cm and 10 cm wide, are similarly steeply dipping parallel to the

dominant foliation and to the cataclasite fault surfaces (Table 8; Fig. 26). The pseudotachylyte veins appear to remain parallel to their generation surfaces and not at oblique angles as is often observed (e.g., Magloughlin 1992). Quartz, plagioclase and epidote clasts within the pseudotachylyte veins preserve no subsolidus asymmetry or sense of shear (Fig. 26), suggesting brittle cataclasite fragments were entrained in a melt. Slickensides (Table 8; Appendix A) indicate a predominantly dextral sense of slip and plunge between 5° and 40° NW or SE. Microfaults (Fig. 26) are common and crosscut the dominant foliation, cataclasite bands and faults. No structures crosscut the pseudotachylyte veins.

Smaller fault zones straddle meter to decameter wide saddles in the cirque ridge surrounding Lake Minotaur in the Labyrinth Mountain pluton (Fig. 27; Table 8). Lineations on these faults trend and plunge very similarly to those on Minotaur Lake fault surfaces. Fault orientations and senses of slip are less consistent. In general, kinematic indicators and the association between cataclasite and pseudotachylyte in the NE of the study area are most compatible with brittle, upper-crustal, late-stage dextral transpression (e.g., Magloughlin 1992; Paterson et al. 2004).

Joint sets throughout the study area (Fig. 28; Table 9; Appendix A) are generally steep and NE-SW striking. These data are most simply interpreted as mode I fractures associated with NE-SW contraction and are consistent with regional mode I fracture data (Paterson et al. 1994). However, thin quartz-plagioclase dikes at Labyrinth Mountain, appearing as thin impregnated or healed fractures (Fig. 28; Table 7), strike E-W. Such fractures post-date crystallization of the main phase of the Labyrinth Mountain granodiorite. And the presence of plagioclase and quartz filling indicates a formation

toward the end of regional magmatism or metamorphism. Data are insufficient to draw conclusions about stress fields, yet an E-W strike could be a response to localized magma cooling and contraction.

	Fault plane			Slickenside lineations		
Location	**Strike**	**Dip**		**Plunge**	**Trend**	**Sense of slip**
Minotaur Lake Fault						
04NCGB044	328	88	NE	18	328	dextral
04NCGB044	163	84	SW	?	?	?
04NCGB044	155	83	SW	?	?	?
04NCGB044	308	84	NE	11	314	dextral
04NCGB044	325	68	NE	40	128	dextral
04NCGB044	325	80	NE	5	146	sinistral
04NCGB044	308	90	V	31	124	dextral
Labyrinth Mountain						
04NCGB053	256	57	NW	26	036	sinistral or oblique thrust
04NCGB056	105	74	SW	04	109	dextral
04NCGB056	131	74	SW	steep	SW	NE-side-up; normal
04NCGB057	357	26	E	21	119	dextral or low-angle normal
04NCGB057	083	36	S	13	126	sinistral
04NCGB058	180	32	W	30	290	low-angle normal
04NCGB058	305	74	NE	12	320	dextral
04NCGB059	NW-SE	steep	?	?	?	Brecciated, chloritized fault rock in saddle

Table 8. Fault plane data.

Strike	Dip*
230	90
208	74
210	50
195	52
88	84
343	74
100	88
228	90
310	58
119	10
218	90
240	75
212	54
210	56
209	56
332	67
198	70
195	56
35	81
186	57
194	64
190	60
306	85
230	90
287	80
65	81
8	75

*Right-Hand-Rule

Table 9. Labyrinth Mountain pluton fracture data.

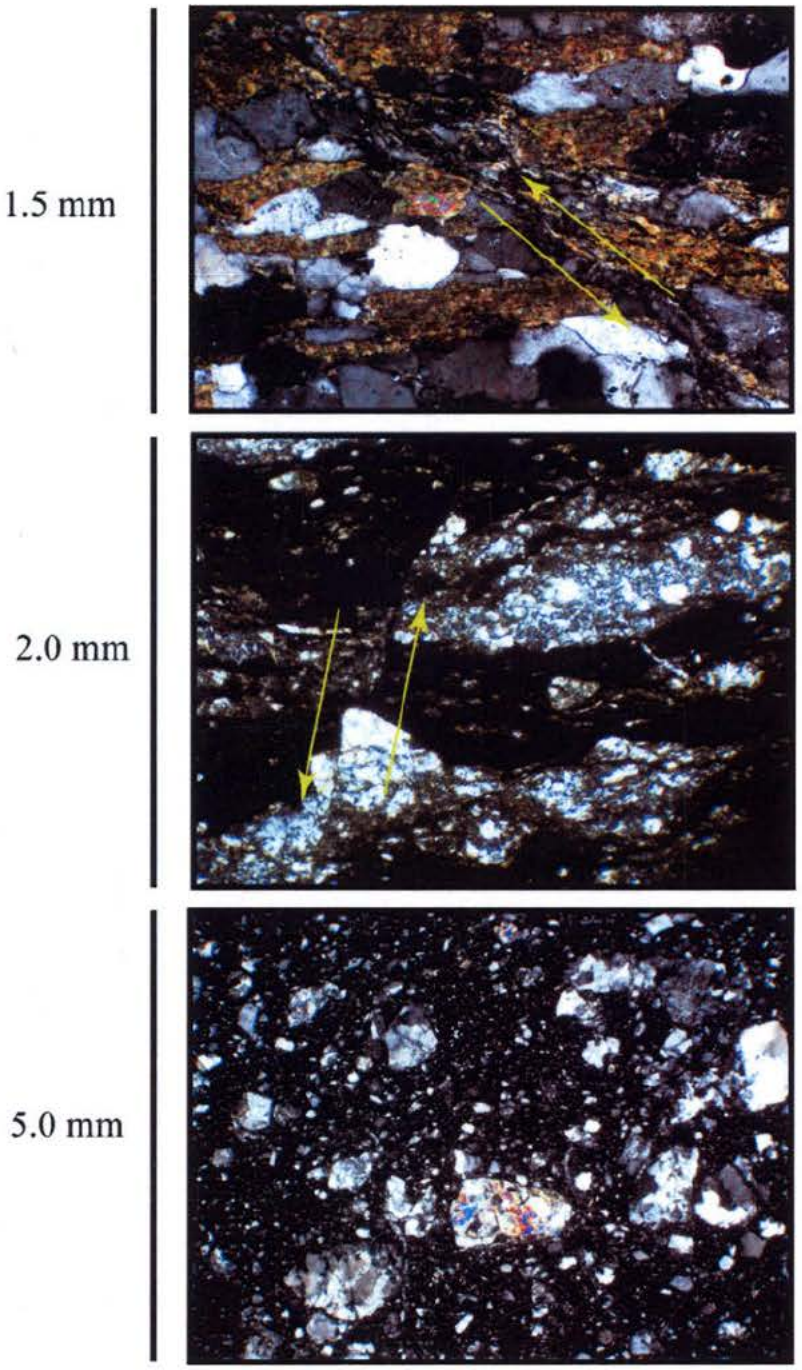

Figure 26. Minotaur Lake Fault rocks. Chloritized microfault in strongly foliated fine-grained biotite schist (top); microfault in banded fine-grained altered cataclasite (middle); plagioclase, epidote and quartz fragments in a glassy pseudotachylyte matrix.

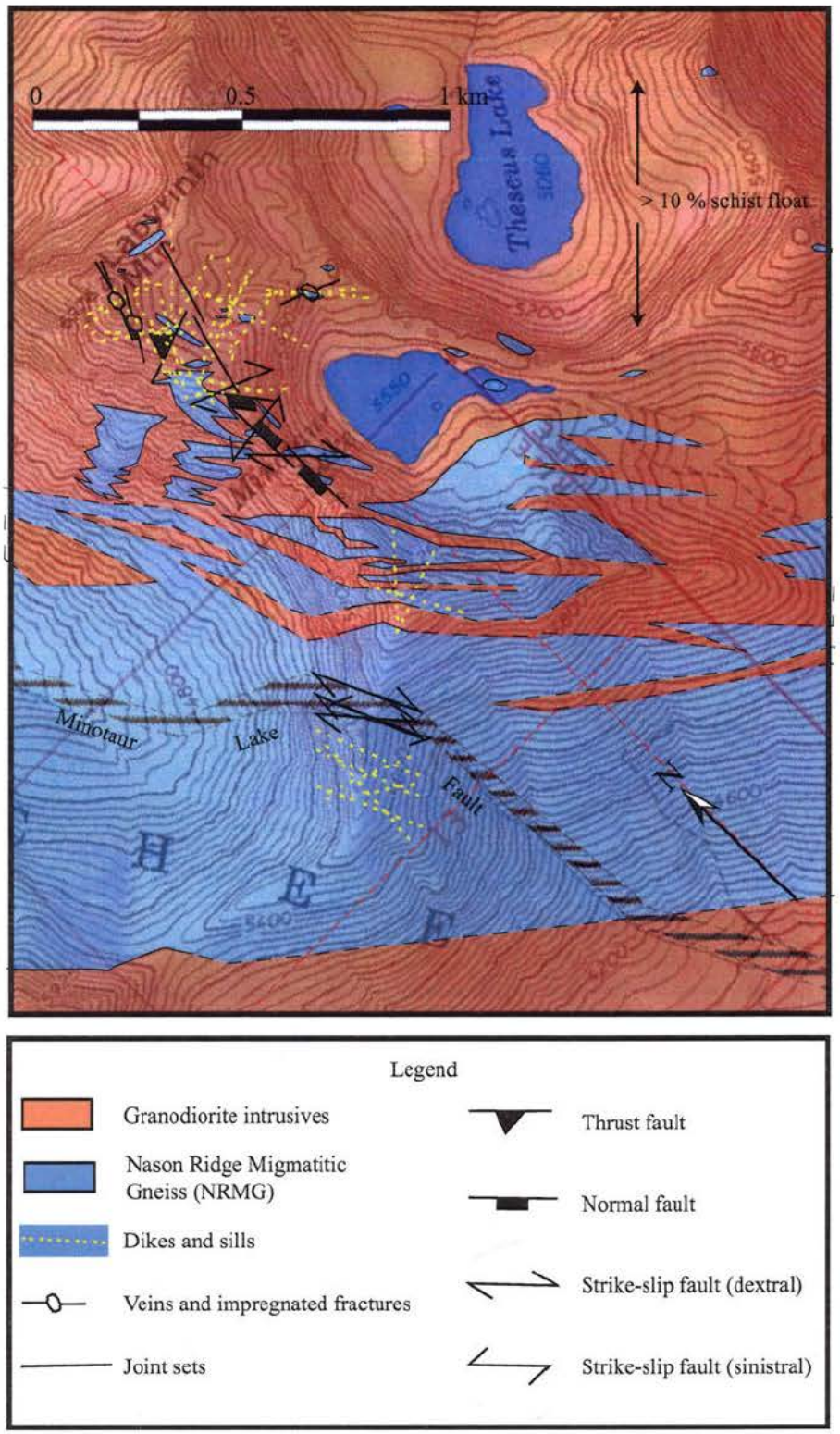

Figure 27. Map of representative dikes, sills, faults and joints in the Labyrinth Mountain/Minotaur Lake Fault area. Note the orientation of the north arrow.

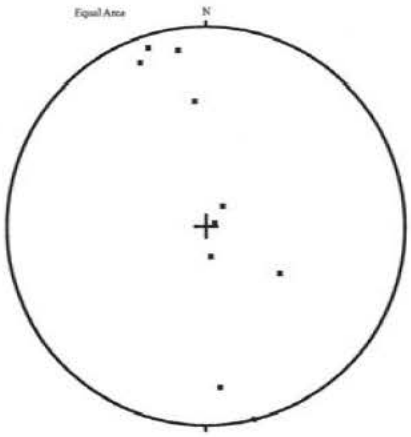

■ Qtz-Pl dikes (mm-cm), Labyrinth Mountain (Data:10)

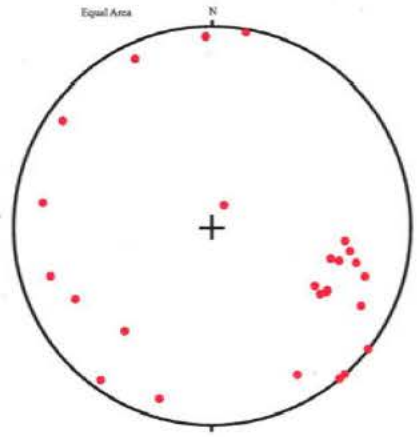

● Joints, Labyrinth Mountain (Data: 27)

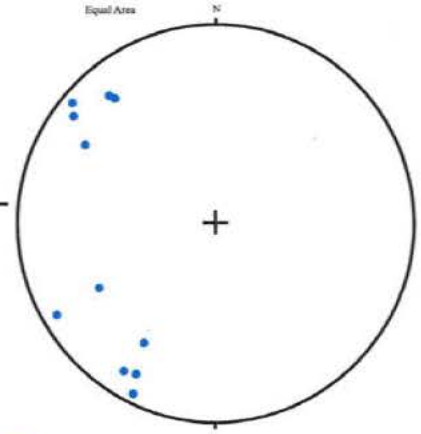

● Joints, Jove Peak (Data: 11)

Figure 28. Joint sets. Equal area steronet plots of poles for joint sets in the Labyrinth Mountain pluton and in the Mount Stuart batholith, Jove Peak. Thin quartz-plagioclasedikes possibly represent early brittle deformation in the Labyrinth Mountain granodiorite.

V
METAMORPHISM

Isograds and metamorphic textures

The Labyrinth Mountain to Jove Peak study area experienced a polymetamorphic history similar to that documented for much of the northeast side of the Mount Stuart batholith (e.g., Paterson et al. 1994; Evans and Davidson 1999; Stowell and Tinkham 2003). Pseudomorphs of kyanite and sillimanite after andalusite (Fig. 29) preserved within ½ kilometer of the Mount Stuart batholith (Fig. 30) are evidence a higher pressure regional metamorphic overprint of contact metamorphism associated with emplacement of the Mount Stuart batholith. Petrographically identifiable contact aureoles are absent from the margins of the southwestern Kbgg sill and the Labyrinth Mountain pluton.

Peak metamorphic conditions throughout the study area were amphibolite to upper amphibolite facies. Amphibolite lenses within the Chiwaukum Schist are characterized by Grt+Hbl+Bt+Pl+Qtz. Peak assemblages in the study area for metapelites are typically Grt+(Ky/ Fib)+St+Bt+Ms+Qtz+Pl±Ilm±Gr (Fig. 30; Appendix B). Chlorite is interpreted as retrograde, and fibrolite appears to postdate kyanite in the Labyrinth Mountain area—a transition zone between kyanite and sillimanite stability zones (Fig. 30).

Comparison of regional isograds with the redrawn isobars (Fig. 30) reveals a complex relationship between pressure and peak mineral assemblage preservation. Evans and Davidson (1999) postulated that differences in heating and dehydration related to

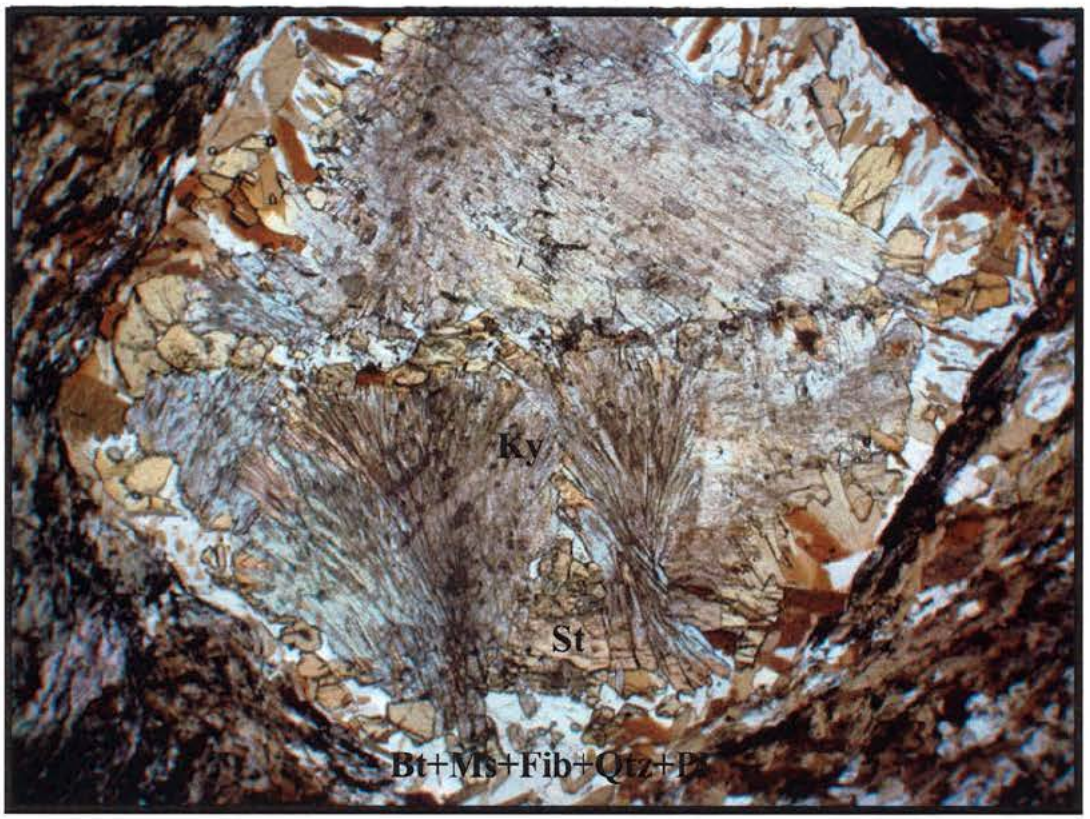

10 mm

Figure 29. Sample of Chiwaukum Schist 1/3 km NE of Mount Stuart batholith. Pseudomorph of Ky+St+Bt+Ms+Qtz after And; diagnostic chiastolite cross is preserved. Periphery of pseudomorph is Qtz+Pl+Bt+Fib+Ms. The matrix also contains 0.5 mm garnet.

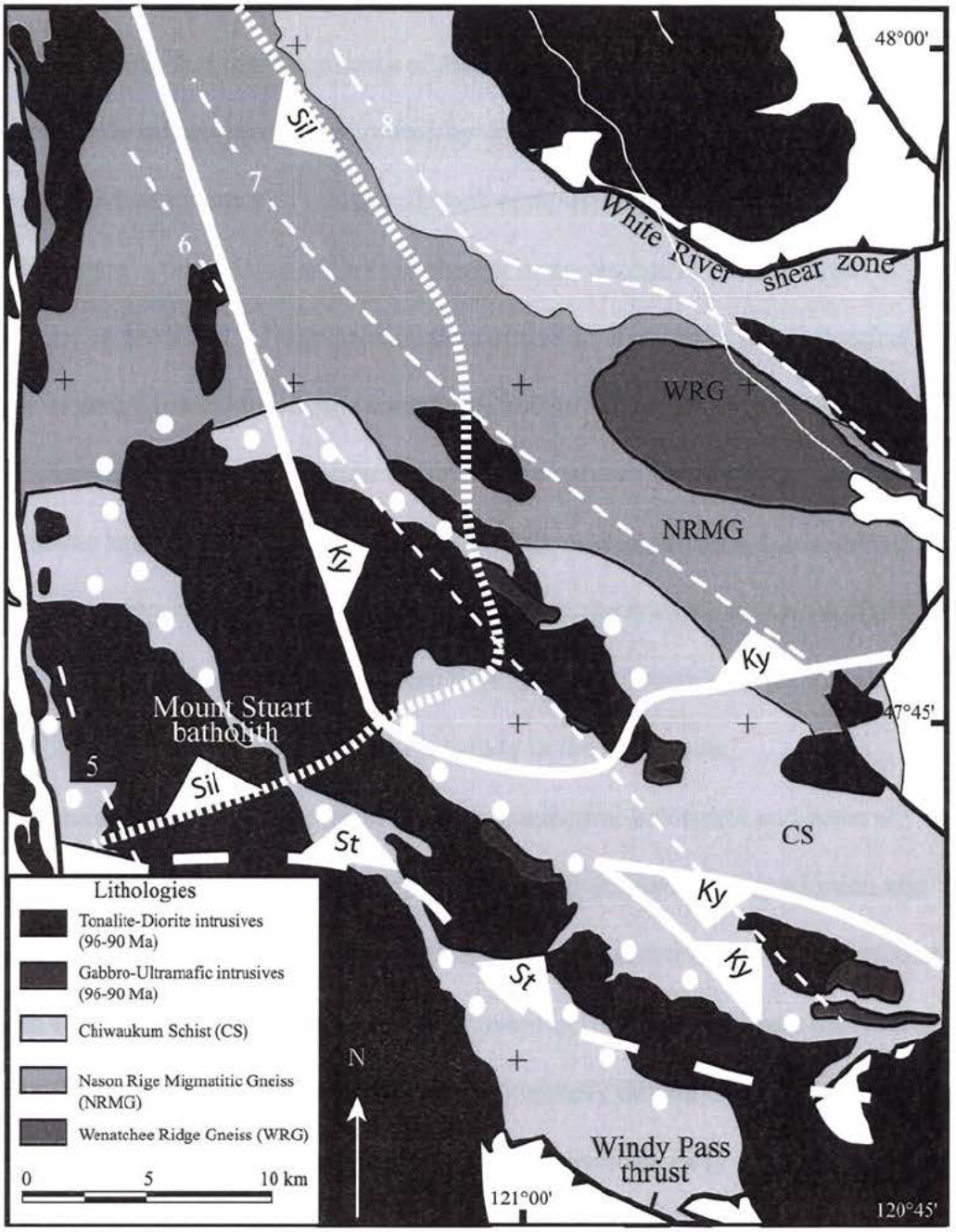

Figure 30. A comparison of isograds and isobars in the southern Nason terrane. Isograds and mineral stability fields after Evans and Davidson (1999) and this study; isobars as shown in figure 3B; andalusite occurrence (white circles) after Evans and Berti (1986); Paterson et al., 1994; this study.

magmatism are the primary controls on mineral growth during high pressure metamorphism and that the complexity of the isograds in the Mount Stuart domain reflects prograde mineral reactions limited by dehydration and rapid cooling to a cooler upper crust. Broad changes in schist bulk rock composition could also change the observed mineral assemblages with little change or no change in pressure and temperature, as predicted by compositionally controlled changes in pseudosection topology among Chiwaukum Schist samples (Tinkham 2002; Zuluaga 2004). However, whether changes in bulk composition are enough to explain the complex isograds in the Nason terrane has not been tested. Regardless of these complexities, the trends of the redrawn isobars are roughly parallel to the isograds in the northwest extension of the terrane (Fig. 30). By comparison, the more E-W trending Brown and Walker (1993) isobars (Fig. 3A) are discordant with the isograds in the same area.

Kyanite and staurolite porphyroblasts are euhedral-subhedral and generally lie within the plane of dominant gneissosity or schistosity defined by aligned mica and alternating quartz-plagioclase layers. Kyanite is likely syntectonic, as porphyroblasts are seen both overgrowing aligned biotite and included in the rims of garnets that deflect the dominant foliation. Staurolite porphyroblasts commonly deflect biotite schistosity and are occasionally included in garnet, suggesting pretectonic or early syntectonic growth (Appendix B). The textural interpretation that staurolite growth initiated before kyanite growth is predicted by phase equilibria modeling for other Chiwaukum Schist and Nason Ridge Migmatitic Gneiss samples in the southern Nason terrane (Tinkham 2002; Zuluaga 2004).

Garnets porphyroblasts are euhedral to subhedral and are 0.5 mm to >10 mm in diameter. The larger garnets are associated with coarser mica schist in the NRMG and in rafts within the Labyrinth Mountain pluton. Most garnet porphyroblasts are capped by biotite selvages and flanked by quartz-plagioclase strain shadows, indicating that considerable garnet growth occurred at an early stage of or before the latest foliation development. Inclusions of staurolite and kyanite in the rims of garnets (Appendix B) provide strong evidence that most, if not all, garnet grew in the peak assemblage stability field.

Garnet inclusion patterns further elucidate the relationship between foliation development and garnet growth (Fig. 31). In thin section, mineral inclusion lineations in garnet from both the Chiwaukum Schist the Nason Ridge Migmatitic Gneiss appear to have overgrown an earlier schistosity (S1). Chiwaukum Schist samples, exemplified by sample 03NC149 (Fig. 31), however, preserve this earlier foliation, where fine-grained gneissic layering (S1) is being folded around garnet porphyroblasts that armor straight inclusion patterns (Si) roughly parallel to the folded external foliation (Se). Axial planar cleavage in the folded layering (S2) is almost perpendicular to S1. The use of S1 and S2 connote two distinct foliations developed in response to different stress orientations. This may be misleading; two models can account for the observed transposition (Passchier and Trouw 1998): In the first, a single foliation is developing with a component of shear that rotates the garnet until all connection between the Si and Se is lost. In the second, the garnet grows over a foliation (Si) before a second (Se) develops at some angle to the first. The linearity of the inclusion patterns and the lack of continuation between internal and external foliation, even during the early stages of transposition in sample 03NC149,

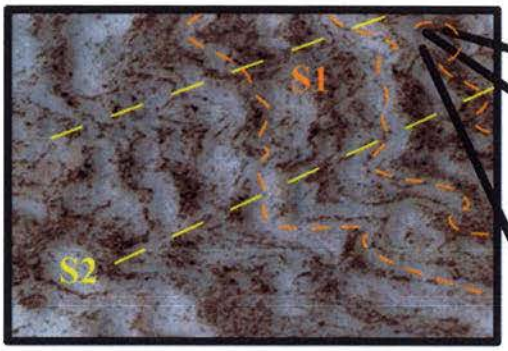

3 mm

Folded S1 gneissic bands of alternating Qtz+Pl and fine-grained Bt partially transposed to S2.

Sample 03NC149

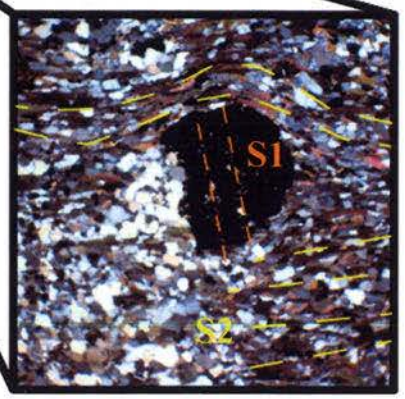

Bt and elongate Qtz grains forming axial planar S2 fabric; Inclusion pattern in Grt (Si) preserves S1 as external matrix foliation (Se) aligns with S2.

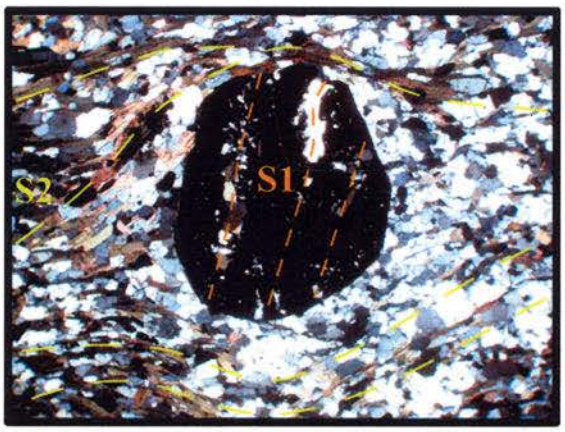

Sample 03NC143

Only inclusion patterns in garnet suggest the presence of an earlier schistosity (Si = S1); the matrix fabric is a relatively undeformed, pervasive, medium to coarse grained Bt schist; deflection of this schistosity around garnet porphyroblasts that overgrew a foliation nearly at right angles to the current external foliation in this plane suggests inter- or syn-tectonic Grt growth.

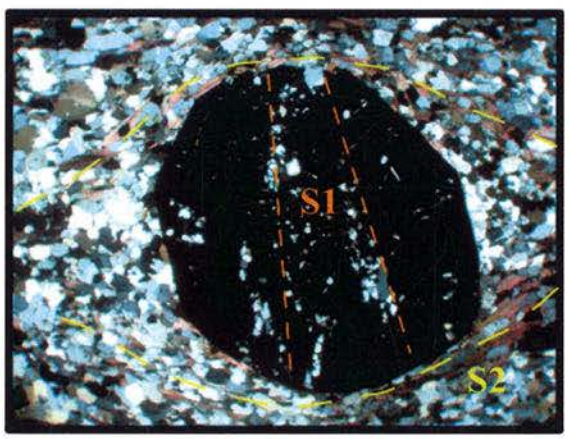

1.5 mm

Figure 31. Garnet inclusion patterns. Evidence for foliation transposition. Foliation S1 is visibly folded in sample 03NC149 and in other Chiwaukum schist samples; whereas, foliation S1 is completely transposed to S2 in the Nason Ridge Migmatitic gneiss (e.g, sample 03NC143).

weaken the case for garnet rotation during development of a single foliation. Instead, the best explanation for the discordance between Si and Se is intertectonic garnet growth and transposition of an earlier foliation into a new foliation at the centimeter-scale. Garnet porphyroblasts overgrowing a foliation in a broad meter-decameter scale open fold hinge could show transposition such as this during a single episode of folding as the interlimb angle becomes tighter. Nason Ridge Migmatitic Gneiss samples, such as 03NC143, preserve no evidence for an earlier foliation in the matrix (Fig. 31). Rather, the pervasive coarse-grained schistosity (Se) and isoclinal, high amplitude:wavelength, upright folds suggest an earlier foliation (S1), now only evident in Si, was completely transposed to S2. The orientations of the developing foliation S2 in the Chiwaukum Schist and of the pervasive foliation in the NRMG are consistent with the dominant foliations in their respective domains (Fig. 16).

Thermodynamic modeling

Composition specific THERMOCALC thermodynamic modeling in the MnNCKFMASH chemical system provides a predicted stability field in pressure-temperature space for the peak assemblage from sample 03NC19A. This sample was collected from a large schist raft of Nason Ridge Migmatitic Gneiss in the Labyrinth Mountain pluton (Fig. 5) and contains the peak assemblage Grt+Ky+St+Bt+Ms+Qtz+Pl. Typical of NRMG samples, as discussed above, biotite defined schistosity wraps around 4-8 mm garnet porphyroblasts. Staurolite is regularly associated with other iron bearing phases such as biotite and garnet and, thus, is probably in equilibrium with the peak assemblage. Inclusions in garnet are typically Qtz+Ky+St ± Bt and Ms. The peak

assemblage is predicted be stable between 6.6 kbar to 8.4 kbar and 630 °C to 650 °C (Fig. 32). Notice that garnet growth could have initiated at temperatures below 450 °C and that the lower end of the peak assemblage field is close to the sillimanite stability field.

Garnet-biotite (GABI) thermometry and garnet-aluminum silicate-plagioclase (GASP) barometry intersections provide independent constraints on mineral stability using microprobe mineral analyses (Table 10). The Bhattacharya (1992) calibration yields an intersection at 6.79 kbar and 632 °C (Fig. 32). THERMOCALC predicts an intersection at 7.86 kbar and 665 °C (Dr. Carlos Zuluaga, Pomona College, personal communication, 2005).

The lower pressure end of the stability field (6.6-7.0 kbar) and the Bhattacharya (1992) GABI-GASP intersection pressure correspond well with the isobars projected through this area—particularly the redrawn isobars—inferred from other paleobarometric analyses throughout the terrane (Fig. 3 B).

Timing of Garnet Growth

Samarium-Neodymium isochron garnet growth ages from two NRMG pelitic schist samples (03NC19A and 03NC143) date the timing of peak metamorphic conditions in the Labyrinth Mountain area. Isochrons constructed from 3-7 points per sample yield internal garnet ages, garnet core-whole-rock ages, garnet rim-matrix ages and garnet matrix-whole-rock ages (Table 11; Fig. 33). The ca. 90-91 Ma ages generally overlap within uncertainty, both within samples and between samples.

Core, rim and leached fractions from a single, large 8 mm, glassy, euhedral garnet crystal from sample 03NC19A, described in the preceding section, reveal Nd

GARNET

	Weight %							
	SiO2	**TiO2**	**Al2O3**	**FeO**	**MgO**	**MnO**	**CaO**	**Total**
2 narrow rims	36.942	0.009	21.434	32.974	2.427	3.530	2.738	100.050
wide rim	36.635	0.015	21.446	31.435	3.281	3.528	2.737	99.077
	Cations (based on 12 oxygens)							
	Si	**Ti**	**Al**	**Fe+2**	**Mn**	**Mg**	**Ca**	**Total**
2 narrow rims	2.963	0.001	2.026	2.212	0.165	0.422	0.235	8.024
wide rim	2.961	0.001	2.043	2.125	0.225	0.425	0.237	8.017
	Mg #	**Alm**	**Prp**	**Sps**	**Grs**			
2 narrow rims	0.160	0.729	0.139	0.054	0.078			
wide rim	0.167	0.705	0.141	0.075	0.079			

PLAGIOCLASE

	Weight %							
	SiO2	**Al2O3**	**FeO**	**MgO**	**CaO**	**Na2O**	**K2O**	**Total**
flat wide rim	59.148	25.721	0.038	0.004	6.476	7.740	0.058	99.184
steep rim	59.260	25.013	0.087	0.018	6.170	7.938	0.075	98.560
whole grain	59.151	26.043	0.048	0.002	6.652	7.613	0.077	99.588
	Cations							
	Si	**Al**	**Fe3**	**Mg**	**Ca**	**Na**	**K**	**Total**
flat wide rim	2.654	1.360	0.001	0.000	0.312	0.673	0.003	5.004
steep rim	2.675	1.331	0.003	0.001	0.299	0.695	0.004	5.008
whole grain	2.644	1.372	0.002	0.000	0.319	0.660	0.004	5.001
	Alb	**An**	**Ksp**					
flat wide rim	0.681	0.315	0.003					
steep rim	0.696	0.299	0.004					
whole grain	0.671	0.324	0.004					

Table 10A. Average garnet and plagioclase composition analyses for sample 03NC19A used in thermobarometry. Data were collected by Dr. Carlos Zuluaga with a JEOL microprobe spectrometer at the University of Alabama (July, 2005).

BIOTITE

Weight %										
SiO2	**TiO2**	**Al2O3**	**FeO**	**MnO**	**MgO**	**CaO**	**Na2O**	**K2O**	**H2O**	**Total**
35.169	2.572	21.121	18.568	0.080	9.233	0.001	0.314	8.775	4.002	99.833
Cations (based on 11 oxygens)										
Si	**Ti**	**Al**	**Fe**	**Mn**	**Mg**	**Ca**	**Na**	**K**	**H**	**Total**
2.635	0.145	1.865	1.164	0.005	1.031	0.000	0.046	0.839	2.000	7.730
Mg#	**Al IV**	**Al VI**								
0.470	1.365	0.500								

Table 10B. Average biotite composition analyses for sample 03NC19A used in thermobarometry. Data were collected by Dr. Carlos Zuluaga with a JEOL microprobe spectrometer at the University of Alabama (July, 2005).

Sample	Mass (g)	$[Sm]_{ppm}$	$[Nd]_{ppm}$	$^{147}Sm/^{144}Nd$	2 SE[1]	$^{143}Nd/^{144}Nd$[2]	2 SE[1]	2 SE[3]
03NC143								
Grt	0.09263	7.10	3.04	1.413707	0.008632	0.513297	0.000016	0.000018
Grt m	0.08916	7.78	3.44	1.368393	0.008672	0.513254	0.000006	0.000010
Grt m R	0.12531	6.03	1.85	1.969361	0.013240	0.513606	0.000006	0.000010
Grt m rp R	0.24053	6.81	1.48	2.773190	0.018613	0.514093	0.000006	0.000010
whole rock 04	0.16326	2.98	14.02	0.128537	0.000795	0.512531	0.000009	0.000012
whole rock 05	0.15849	3.43	19.56	0.106019	0.000657	0.512540	0.000006	0.000010
matrix	0.20380	3.30	19.67	0.101499	0.000562	0.512537	0.000008	0.000011
03NC19A								
Grt rim	0.07036	3.26	1.34	1.470271	0.009290	0.513248	0.000021	0.000022
Grt rim rp R	0.13979	3.06	0.64	2.905548	0.020119	0.514095	0.000009	0.000012
Grt core	0.07905	3.97	2.91	0.792694	0.005030	0.512841	0.000007	0.000011
whole rock 04	0.17961	3.54	17.80	0.120355	0.000690	0.512456	0.000010	0.000013
whole rock 05	0.19561	5.30	26.99	0.118594	0.000724	0.512413	0.000009	0.000012
matrix	0.18382	4.09	21.13	0.116892	0.000665	0.512430	0.000009	0.000012

1 Run uncertainty

2 $^{143}Nd/^{144}Nd$ is normalized to $^{146}Nd/^{144}Nd=0.7219$

3 Combined error: Quadratic sum of 143Nd/144Nd run uncertainty and external standard reproducibility; analyses of the J Ndi standard between 2/02 and 8/05 yielded 0.512116 +/-0.000008 (2SE).

Table 11. Samarium and Neodymium isotope data for geochronology. Multi-garnet fraction (m), only cursory rough picking of garnet fragments from matrix phases (rp), garnet residuum after leaching (R). See text for discussion.

Bulk Composition (Mole %)			
SiO2	Al2O3	CaO	MgO
71.751	10.660	2.299	4.556
FeO	K2O	Na2O	MnO
6.583	1.691	2.320	0.140

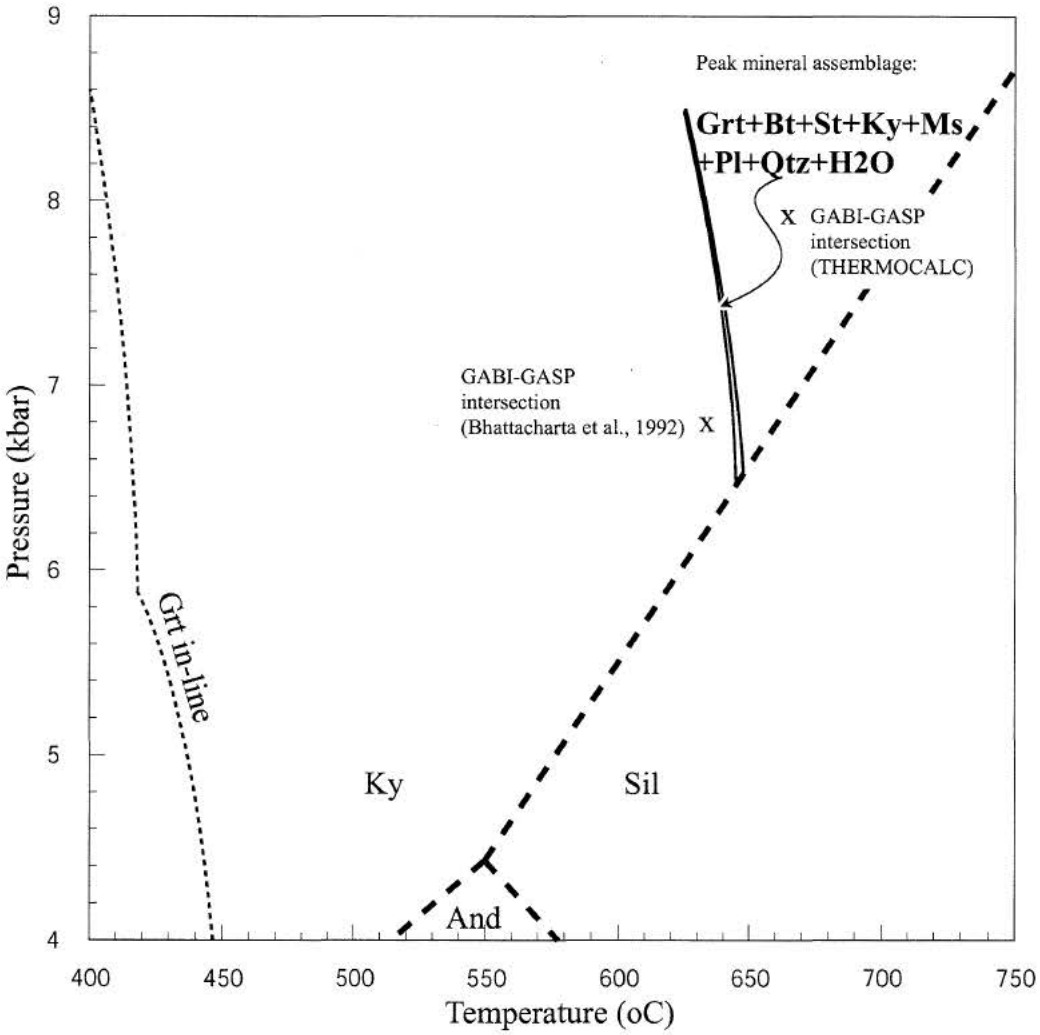

Figure 32. Sample 03NC19A: Peak assemblage stability field. Composition-specific P-T phase diagram (pseudosection) showing the predicted equilibrium peak assemblage stability field, aluminum silicate stability fields, the garnet stability field and two independent pressure-temperature estimates using the GABI-GASP reactions intersections. THERMOCALC modeling results are based on the MnNCKFMASH chemical system.

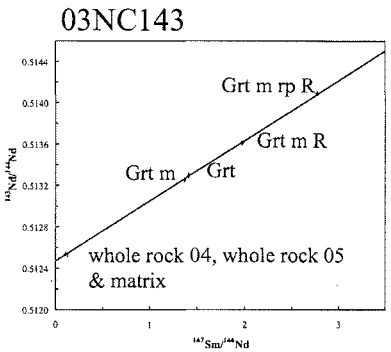

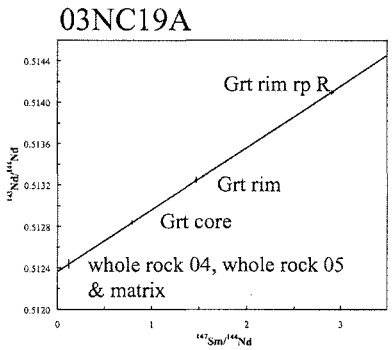

Sample	Isochron Points	Age (Ma)[1]	Uncertainty[1] (+/- Ma)	MSWD
03NC143				
	All (7)	**88.7**	1.9	3.6
	Garnets (4)	**90.7**	1.9	1.8
	Garnets & whole rock 04 (5)	**90.1**	1.0	1.4
03NC19A				
	All (6)	**91.4**	3.3	5.9
	Garnets (3)	**90.7**	1.5	0.17
	Garnet core & whole rocks 04 & 05 (3)	**92.4**	8.4	NA
	Garnet rims & matrix	**91.3**	1.1	0.63
	Garnets & whole rock 04 (4)	**90.1**	1.1	0.91

1 Age and age uncertainty were calculated in Isoplot using the combined analytical and external reproducibility error for $^{143}Nd/^{144}Nd$. See data table.

Figure 33. Sm-Nd isochrons and garnet growth ages for samples 03NC143 and 03NC19A. Multi-garnet fraction (m), only cursory rough picking of garnet fragments from matrix phases (rp), garnet residuum after leaching (R).

concentrations between 0.64 ppm and 2.91 ppm. Matrix and whole rock Nd concentrations from this sample range from 14 ppm to 20 ppm (Table 11). Samarium and neodymium concentrations are higher in the garnet core than in the rim. The $^{147}Sm/^{144}Nd$ spread resulting from this core-rim variation in REE concentration attests to the utility of core-rim separation for isochron construction (Fig. 33). Leaching an only roughly picked, finely ground, rim fraction with high molarity hydrochloric acid and concentrated sulfuric acid produces Nd concentrations >50% lower than the rim fraction that had been optically hand-picked free of inclusions. The corresponding $^{147}Sm/^{144}Nd$ ratio for the leached rim fraction was nearly twice as high as the non-leached rim. The resulting range of $^{147}Sm/^{144}Nd$ ratios from garnet fractions permit construction of an internal garnet-only isochron that yields an age of 90.8 ± 1.3 Ma. This age also showed the highest probability of fit and, thus, the lowest MSWD (mean sum of squares of weighted deviates; Fig. 33). These results suggest that leaching effectively reduced the isotopic contribution of LREE enriched inclusions far more effectively than binocular picking and that the inclusions throughout the garnet are in equilibrium with the garnet. Otherwise, the garnet points with different Nd concentrations and different $^{147}Sm/^{144}Nd$ ratios would not define an isochron.

Within age uncertainty, the garnet rim-matrix age (91.3 ± 1 Ma) from sample 03NC19A is indistinguishable from the internal garnet age (90.8 ± 1.3 Ma), garnet whole-rock-matrix age (91.4 ± 3.6 Ma) and garnets-whole rock age (90.1 ± 1 Ma). The garnet core whole-rock age (92.4 ± 8.4 Ma) is spurious, because the three-point isochron is unconstrained by two whole-rock fractions that show unexpectedly different samarium and neodymium concentrations and apparent disequilibrium (Table 11); the age was

estimated using averages of the two whole-rock isotope ratios. The 2004 whole-rock fraction is a much better fit to the seven-point (all data) isochron than either the 2004 matrix or 2005 whole rock (Fig. 32).

This apparent disequilibrium relationship is also observed in matrix and whole-rock analyses from sample 03NC143 (Table 11; Fig. 33), suggesting the problems may share a common cause. Open system behavior cannot explain the better fit of the 2004 whole rock points; nor would incomplete dissolution of phases in 2005 whole-rock samples explain the poor fit of 2004 matrix points. However, the matrix samples may be in disequilibrium with the whole garnet, as theoretically predicted, since garnet cores are chemically isolated from the matrix during isotopic evolution. If this is the case, analyzing a whole-rock sample with an incorrect modal proportion of garnet—namely, too little—will push the Sm-Nd concentrations and ratios of the whole-rock sample toward the disequilibrium matrix composition. This is a conceivable scenario for samples 03NC143 and 03NC19A, because: 1) Representative garnet modes were difficult to estimate in 2005, because the sample had been broken apart and excavated for garnets, and 2) 2005 whole-rock samples have neodymium and samarium concentrations that are closer to 2004 matrix sample concentrations than to 2004 whole-rock sample concentrations (Table 11). Isotope mass-balance calculations show that, in fact, 2005 whole-rock Sm/Nd ratios can be modeled by varying garnet modes and mixing garnet and matrix Sm/Nd ratios. No reasonable proportion of garnet, however, can appreciably improve the fit of the whole-rock point to the isochron. Thus, the apparent disequilibrium may be better attributed to sampling bias in rocks with an inhomogeneous distribution of LREE enriched phases or to an unidentified analytical problem.

Sample 03NC143, for which garnet inclusion patterns evidence transposition of an earlier foliation (Fig. 31), was collected immediately SW of the Minotaur Lake fault, approximately 250 m from the contact between the NRMG and the Labyrinth Mountain pluton (Fig. 5). This sample contains fewer phases than sample 03NC19A; the peak assemblage includes Grt+Bt+Qtz+Pl±St±Ilm. The most abundant phases included in garnet are quartz and plagioclase; these are visible in thin section (Fig. 31). Accessory phases included in garnet are Zr, Ilm and St (Table 12). Identification of a 60 μm monazite crystal in the matrix indicates that monazite inclusions in garnet are possible, although none were observed. Garnets are typically 5-7 mm, deep purple or red and euhedral (Appendix B). The multi-garnet fraction used for geochronology is composed of the least included separates from four smaller euhedral garnets.

Results from Sm-Nd analyses of 03NC143 garnet fractions (Table 11) further extol the advantages of strong acid leaching experiments. Neodymium concentrations are similar in the single garnet crystal fraction and the non-leached multi-garnet fraction. Leached multi-garnet fractions reveal neodymium concentrations nearly half or less of the non-leached fractions. As in sample 03NC19A, leaching increases the $^{147}Sm/^{144}Nd$ ratio, thereby increasing the isochron age precision (Table 11; Fig. 33). The multi-garnet fraction that was only briefly handpicked from the matrix, finely ground and leached successively in high molarity hydrochloric acid and sulfuric acid yields the highest $^{147}Sm/^{144}Nd$ ratio and lowest Nd concentration. The garnet-only isochron age (90.8 ± 5.4 Ma) overlaps within uncertainty the garnet whole-rock age (90 ± 2 Ma) and seven-point isochron age (88.6 ± 1.9 Ma), suggesting inclusions are likely in equilibrium with the garnet.

	Inclusion (# analyses)	Size (microns)
Garnet 1		
	Zircon (3)	1-20
	Ilmenite	15
Garnet 2		
	Zircon (1)	20
	Ilmenite (1)	40
	Quartz (abundant)	
	Plagioclase (abundant)	
	Staurolite	
Matrix		
	Monazite	60
	Ilmenite (abundant)	

Table 12. Sample 03NC143: Inclusions within garnet and accessory matrix phases. Detected with a JEOL microprobe spectrometer at the University of Alabama (July, 2005).

VI
DISCUSSION

Evaluating Tectonic Models

The agreement between the ca. 91 Ma U-Pb zircon age for the Labyrinth Mountain pluton and the ca. 90-91 Ma Sm-Nd garnet ages is strong evidence for synchronicity and, consequently, for metamorphic garnet growth resulting from heating of the schist by the granodiorite pluton . Garnet growth may have initiated at lower temperatures and pressures than those indicated by the peak assemblage field; however, the temperature increase associated with intrusion likely accelerated garnet growth. Rapid garnet growth, coarse core-rim separation and 10^6 year precision make differences in core and rim ages irresolvable.

Peak metamorphic conditions (>6.6 kbar, 630-665 °C) in the Labyrinth Mountain area are consistent with other thermobarometric data from the northeast side of the Mount Stuart batholith (e.g., Brown and Walker 1993; Evans and Davidson 1999; Tinkham 2002; Tinkham and Stowell 2003; Fig. 3). Petrographic evidence that garnet grew in the peak assemblage field coupled with a 90-91 Ma garnet growth age suggests that most, if not all, loading occurred prior to 91 Ma in the Labyrinth Mountain region. Catazonal depth zone characteristics—the absence of a recognizable contact metamorphic aureole around the pluton and the gradational concordant contact—coupled with the U-Pb zircon age of 90.6 ± 2.4 Ma independently support an interpretation of deep burial of this area ca. 91 Ma.

Mid-crustal emplacement of the Labyrinth Mountain pluton is consistent with deep-seated emplacement of the Dirtyface pluton (7-9 kbar; Fig. 9 and Fig. 34) and Tenpeak pluton (9-10 kbar) to the northeast. All three plutons are ca. 91 Ma (Fig. 9 and Fig. 34; Walker and Brown 1991; Paterson et al. 1994), and the felsic phases of the Tenpeak pluton are petrogenetically similar to the Labyrinth Mountain pluton (Section III). Additional U-Pb zircon ages from the Sloan Creek pluton and a NRMG sill in the northwest of the Nason terrane cluster around 91-92 Ma (Walker and Brown 1991), demonstrating that the Nason terrane experienced widespread intrusion ca. 91 Ma.

The origin of the NRMG in the study area can be largely attributed to granodioritic or tonalitic sills and dikes associated with the main ca. 91 Ma Labyrinth Mountain pluton (Section IV). Given the widespread occurrence of other km-scale 91 Ma plutons, it is not unreasonable to suspect that the NRMG contains abundant 91 Ma intrusives.

The position of the ca. 91 Ma Labyrinth Mountain pluton just 5 km northeast of the ca. 93.5-96 Ma hook region of the Mount Stuart batholith makes it particularly well suited to constrain the timing of regional loading. The deep-seated emplacement of the ca. 91 Ma Tenpeak pluton has little bearing on the timing of loading in the Nason terrane, because the southwest directed White River shear zone (Fig. 9) has carried the Tenpeak domain over lower pressure rocks to the southwest. The ca. 91 Ma deep emplacement of the Dirtyface pluton likewise offers few constraints on loading, as it is situated in the far northeast of the terrane. Potentially protracted SW-directed loading and proposed SW-directed shearing make this pluton difficult to relate in time and space to the northeastern margin of the Mount Stuart batholith. Detailed mapping of the Labyrinth Mountain-Jove

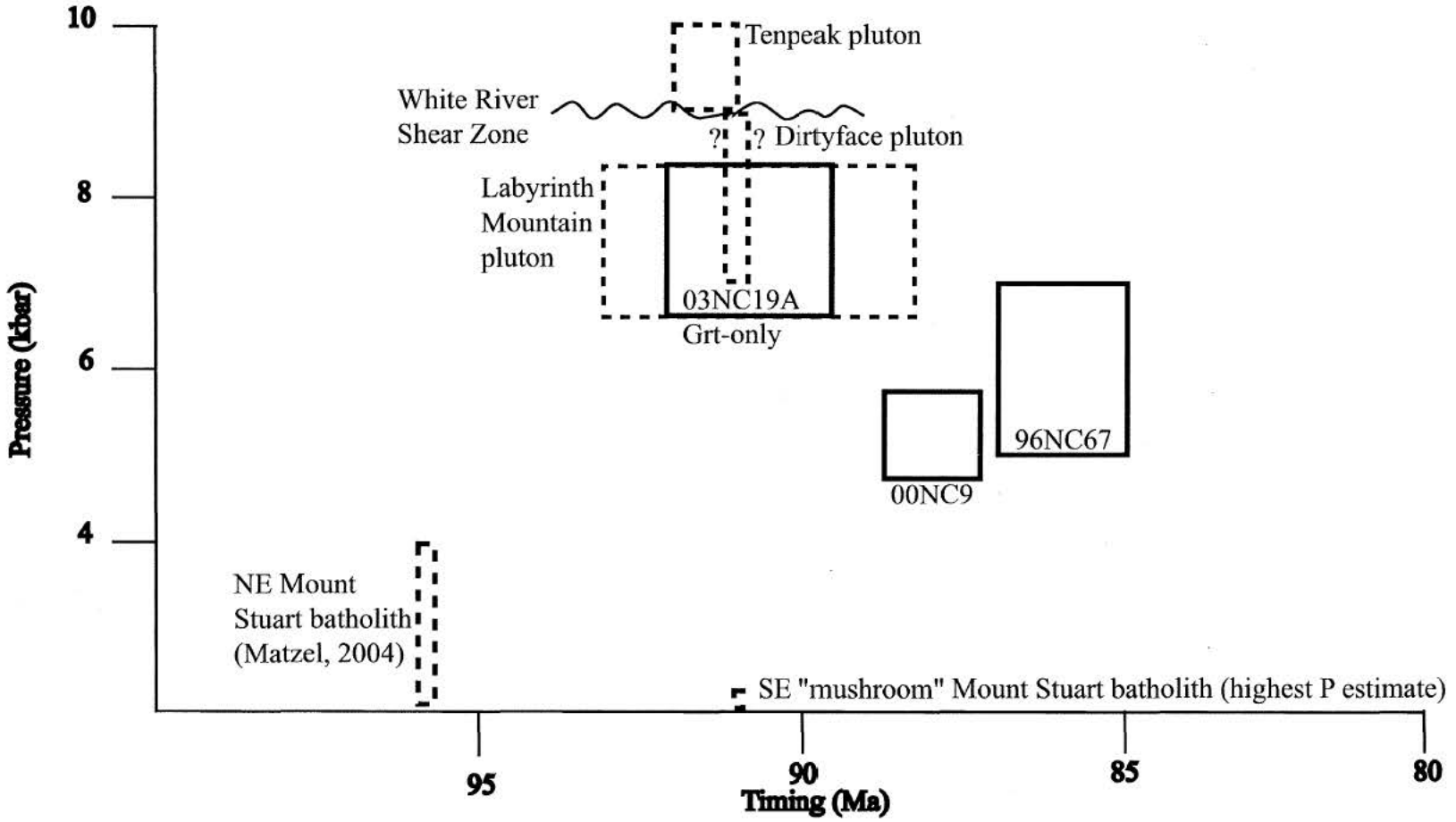

Figure 34. Loading Constraints. A chronology of intrusion (dashed) and peak metamorphism (solid) in the southern Nason terrane and Mount Stuart domain. Ages and uncertainties for the NE Mount Stuart batholith (Matzel 2004); pressures for the NE Mount Stuart batholith (Evans and Berti 1986; Paterson 1994); SE Mount Stuart batholith: ages (Matzel 2004), pressure (Ague and Brandon 1996); 00NC9 and 96NC67 peak metamorphic estimates (Tinkham 2002); Tenpeak pluton (Walker and Brown 1991; Dawes 1993); Dirtyface pluton (Hurlow 1992).

Peak area reveals little evidence for significant NE-side-up shearing and only one major fault, the Minotaur Lake fault, which shows signs of dextral shear and no apparent major offset. Mineral assemblages are continuous across this fault and throughout the study area northeast of the overprinted andalusite zone contact aureole of the Mount Stuart batholith. Thus, pressure increased no less than 2.2 kbar as a result of loading between the NE margin of the Mount Stuart batholith at 93.5-96 Ma and Labyrinth Mountain at ca. 91 Ma (Fig. 32 and Fig. 34). It is important to note that garnet at Labyrinth Mountain grew not in response to loading but instead to ca. 91 Ma intrusion that occurred mostly or entirely after loading. Loading can be constrained in the Labyrinth to Jove Peak area to between 96 Ma and ca. 91 Ma. Using the most conservative pressure difference between Jove Peak at 96 Ma and Labyrinth Mountain at 91 Ma, loading rates likely greater than 1.7 km/m.y.

Relating the pressure conditions at Labyrinth Mountain to those in the synchronously emplaced 91 Ma southeastern "mushroom" shaped region of the batholith (Fig. 9 and Fig. 34; Matzel 2004) is more difficult. Al-in-Hbl barometry indicates very low pressure crystallization (1-2 kbar; Fig. 34; Ague and Brandon 1996) in this region. The range of proposed crystallization pressures from the northeast near Labyrinth Mountain to the southeastern region is 1-3 kbar (Ague and Brandon 1996). In the northeast, a 3 kbar emplacement pressure is compatible with petrographic data (Evans and Berti 1986; Paterson et al. 1994) and is not incompatible with post-Mount Stuart and pre-Labyrinth Mountain age high-pressure loading. But loading of most of the Mount Stuart domain to near peak pressures (Fig. 3B) by 91 Ma is seemingly incompatible with Mount Stuart geochronology and barometry in the southeast.

It is geologically and geometrically unlikely that at ca. 91 Ma, the imposed load increased from <7 km (<2 kbar) in the southeastern region to >24 km (>6.6 kbar) in the northeastern region, across a distance of only 30 km. Theoretical explanations for this apparent incompatibility include: 1) virtually instantaneous loading at 91 Ma within the margin of error for garnet age metamorphism, 2) SE-down tilting five times greater than the tilt proposed by Ague and Brandon (1996) and 3) major W-side uplift along a set of NE or N trending faults. Each of these explanations fails, in turn, on account of a lack of field evidence and incompatibility with extensive structural and metamorphic thermobarometric data (Paterson et al. 1994; Paterson and Miller 1998; Evans and Davidson 1999). Thus, the Al-in-hornblende barometric data (Ague and Brandon 1996) are likely spurious and reflect retrograde pressures (Anderson 1997), as both U-Pb zircon data (Matzel 2004) and synchronous Sm-Nd garnet ages and a U-Pb zircon age at Labyrinth Mountain are more resistant to resetting than Al-in-hornblende and are supported by multiple earlier datasets (Brown and Walker 1993; Paterson et al. 1994; Evans and Davidson 1999).

Whereas ca. 88 Ma garnet ages for peak regional metamorphism (Tinkham 2002) overlap within uncertainty the ca. 90-91 Ma Labyrinth Mountain garnet ages, precise 86 ± 1 Ma garnet ages (Stowell and Tinkham 2003) do not (Fig. 34). Tinkham (2002) hypothesizes that a heat source other than the nearby 93.5-96 Ma Mount Stuart batholith is required to grow garnet at ca. 86 Ma. Stowell et al. (accepted) proposes that a steep geothermal gradient and thermal relaxation following high pressure loading could cause ca. 86 Ma garnet growth. Regional thermal relaxation temperatures would have to reach nearly 670 °C at 6.0 kbar according to thermodynamic modeling and thermobarometry

calculations for ca. 86 Ma garnet (Tinkham 2002; Stowell and Tinkham 2003). Such temperatures equal or exceed peak temperatures for 91 Ma garnet at Labyrinth Mountain, and, hence, might be expected to reset Labyrinth Mountain garnet ages. The intra-sample and inter-sample Sm-Nd garnet age consistency in Labyrinth Mountain pelites evidence no effect from heating associated with regional thermal relaxation at 86 Ma. In support of the Tinkham (2002) hypothesis, the relationship between intrusion and garnet growth synchronous with or following loading at Labyrinth Mountain may be analogous to the relationship between local intrusion and 86 Ma garnet growth to the northwest of Labyrinth Mountain. Alternatively, heating associated with regional thermal relaxation at 86 Ma may not have affected the age of garnets adjacent to the Labyrinth Mountain pluton if the schist had been dehydrated during ca. 91 Ma intrusion. Garnet growth reactions might have been kinetically impeded in the relatively dehydrated Labyrinth Mountain pluton aureole during later heating. Evans and Davidson (1999) argued that the absence of an obvious higher-pressure regional metamorphic overprint and the preservation of contact metamorphic mineral assemblages in the W and NW of the Mount Stuart domain was kinetically controlled and a result of dehydration.

Evidence for foliation transposition postdating garnet growth in the study area may be a local occurrence related to continued NE-SW contraction and upright isoclinal folding. Fabrics in the NRMG are characteristically steeper, more tightly folded and coarser grained than those in the Chiwaukum Schist near the Mount Stuart batholith. Garnet ages from sample 03NC143 (Fig. 31 and Fig. 33) constrain foliation transposition in this sample to <90 Ma and, perhaps more importantly, to a time after loading and preservation of peak metamorphic conditions. Post-loading upright folding and foliation

transposition such as this may have shortened the terrane and, thereby, increased the apparent slope of the isobaric gradient from NE to SW in the Nason terrane. This, rather than a steep-sided magma load (Brown and Walker 1993), is a feasible explanation for the observed paleobarometric gradient. Furthermore, the timing of this late foliation development supports the suggestion by Stowell et al. (accepted) that upper-crustal loading and mid-crustal ductile shortening may be spatially and temporally decoupled.

REFERENCES

Ague, J.J. and Brandon, M.T. (1996) Regional tilt of the Mount Stuart batholith, Washington, determined using aluminum-in-hornblende barometry: Implications for northward translation of Baja British Columbia. Geological Society of America Bulletin, 108, 471-488.

Albertz, Markus, Paterson, Scott R., and Okaya, David (2005) Fast strain rates during pluton emplacement: Magmatically folded leucocratic dikes in aureoles of the Mount Stuart batholith, Washington, and the Tuolumne Intrusive Suite, California. Geological Society of America Bulletin, 117 (3/4), 450-465.

Anczkiewicz, R. and Thirwall, M.F. (2003) Improving precision of Sm-Nd garnet dating by H_2SO_4 leaching—a simple solution to the phosphate inclusion problem, *in* Vance, D. Muller, W., and Villa, I., eds. Geochronology: Linking the isotopic record with petrology and textures. Geological Society Special Publication, 220, 83-91.

Anderson, J.L. (1992) Compositional variation within the high-Mg, tonalitic Mount Stuart batholith, North Cascades, Washington. Geological Society of America Abstracts with Programs, 24, 3.

Anderson, J.L. (1997) Regional tilt of the Mount Stuart batholith, Washington, determined using aluminum-in-hornblende barometry: Implications for northward translation of Baja British Columbia: Discussion and Reply. Geological Society of America Bulletin, 109, 1223-1227.

Bhattacharya, A., Mohanty, L., Maji, A., Sen, S.K., and Raith, M. (1992) Contributions to Mineralogy and Petrology, 1992Non-ideal mixing in the phlogopite-annite binary: constraints from experimental data on Mg–Fe partitioning and a reformulation of the biotite-garnet geothermometer. Contributions to Mineralogy and Petrology, 111, 87-93.

Brandon, M.T. and Cowan, D.S. (1985) The Late Cretaceous San Juan Islands-northwestern Washington thrust system. Geological Society of America Abstracts with Programs, 17, 343.

Brown, E.H. (1987) Structural geology and accretionary history of the Northwest Cascades system, Washington and British Columbia. Geological Society of America Bulletin, 99, 201-214.

Brown, E.H. and Talbot, J.L. (1989) Orogen-parallel extension in the Cascades crystalline core, Washington. Tectonics, 8, 1105-1114.

Brown, E.H. and Walker, N.W. (1993) A magma loading model for Barrovian metamorphism in the SE Coast Plutonic Complex, British Columbia and Washington. Bulletin of the Geological Society of America, 105, 479-500.

Buddington, A.F. (1959) Granite emplacement with special reference to North America, Geological Society of America Bulletin, 70, 671-747.

Bulman, G.R., Stowell, H.H., Tinkham, D.K., and Zuluaga, C.A. (2004) Evaluating thrust sheet models for Late Cretaceous metamorphism in the Nason terrane, Cascades crystalline core, Washington. Geological Society of America Abstracts with Programs, 36 (5), 22.

Chace, R.J. (1998) Samarium-Neodymium garnet geochronology and silicate mineral thermobarometry in the Nason and Chelan Mountains terranes of the North Cascades, Washington, M.S. thesis, 176 p. The University of Alabama, Tuscaloosa, Alabama.

Chace, R.J., Stowell, H.H., and Tinkham, D.K. (1998) The timing and conditions of high pressure metamorphism in the Nason terrane, Cascades Crystalline Core, WA. Geological Society of America Abstracts with Programs, 30 (5), 9.

Cowan, D.S., Brandon, M.T., and Garver, J.I. (1997) Geologic tests of hypotheses for large coastwise displacements—A critique illustrated by the Baja British Columbia controversy. American Journal of Science, 297, 117-173.

Dawes, Ralph L. (1993) Mid-crustal, Late Cretaceous plutons of the North Cascades. petrogenesis and implications for the growth of continental crust [Ph.D. Dissertation], 271 p. University of Washington, Seattle, Washington.

DeLaRoche, H., Leterrier, J., Grandclaude, P., and Marchal, M. (1980) A classification of volcanic and plutonic rocks using R1 - R2 diagram and major element analyses - its relationships with current nomenclature. Chemical Geology, 29, 183-210.

DeWolfe, C.P., Zeissler, C.J., Halliday, A.N., Mezger, K., and Essene, E.J. (1996) The role of inclusions in U-Pb and Sm-Nd garnet geochronology: Stepwise dissolution experiments and trace uranium mapping by fission track analysis. Geochemical et Cosmochemica Acta, 60 (1), 121-134.

England, P.C. and Thompson, A.B. (1984) Pressure-temperature-time paths of regional metamorphism I. Heat transfer during the evolution of regions of thickened continental crust. Journal of Petrology, 25 (4), 894-928.

Evans, B.W. and Berti, J. W. (1986) Revised metamorphic history for the Chiwaukum Schist, North Cascades, Washington. Geology, 14 (8), 695-698.

Evans, B.W. and Davidson, G. F. (1999) Kinetic control of metamorphic imprint during synplutonic loading of batholiths; an example from Mount Stuart, Washington. Geology, 27 (5), 415-418.

Haugerud, R. A., Brown, E. H., Tabor, R. W., Kriens, B. J., and McGroder, M. F. (1994) Late Cretaceous and early Tertiary orogeny in the North Cascades, *in* Swanson, D. A., and Haugerud, R. A., eds., Geologic Field trips in the Pacific northwest, 2, Chapter 2E, 51p. Annual Meeting of the Geological Society of America, Department of Geological Sciences, University of Washington in conjunction with the Geological Society of America.

Hurlow, Hugh A. (1992) Structural and U-Pb geochronologic studies of the Passayten fault, Okanogan range batholith and southeastern Cascades crystalline core, 168p. Washington, Ph.D. thesis, Seattle, Washington, University of Washington.

Keay, Sue, Lister, G., and Buick, I. (2001) The timing of partial melting, Barrovian metamorphism and granite intrusion in the Naxos metamorphic core complex, Cyclades, Aegean Sea, Greece. Tectonophysics, 342, 275-312.

Kriens, B. and Wernicke, B. (1990) Nature of the contact zone between the North Cascades crystalline core and the Methow sequence in the Ross Lake area, Washington: Implications for Cordilleran tectonics. Tectonics, 9, 953-981.

Longtine, M.W. (1991) Mid- to Late Cretaceous structural, metamorphic and magmatic evolution of the Sloan Peak Area, North Cascades, 139 p. Washington, M.S. thesis, University of Texas, Austin, Texas.

Ludwig, K.J. (2003) Isoplot 3.00: A geochronologic toolkit for Microsoft Excel. Berkeley Geochronology Center Special Publication, 4, 71.

Magloughlin, J.F. (1992) Microstructural and chemical changes associated with cataclasis and frictional melting at shallow crustal levels; the cataclasite-pseudotachylyte connection. In Magloughlin, J.F. and J.G. Spray, Eds., Frictional melting processes and products in geological materials. Tectonophysics, 204 (3-4), 243-260.

Magloughlin, J.F. (1993) A Nason terrane trilogy; I, Nature and significance of pseudotachylyte; II, Summary of the structural and tectonic history; III, Major and trace element geochemistry and strontium and neodymium isotope geochemistry of the Pseudosection and Garnet Sm-Nd P-T-t paths Chiwaukum Schist, amphibolite, and meta-tonalite gneiss of the Nason Terrane, Ph.D. thesis, 325 p. Minneapolis, Minnesota, University of Minnesota.

Matzel, J.P. (2004) Rates of tectonic and magmatic processes in the North Cascades continental magmatic arc, Ph.D. thesis, 249 p., Massachusetts Institute of Technology, Boston, Massachusetts.

McGroder, M.F. (1991) Reconciliation of two-sided thrusting, burial metamorphism, and diachronous uplift in the Cascades of Washington and British Columbia. Geological Society of America Bulletin, 103, 189-209.

Miller, R.B. (1985) The ophiolitic Ingalls complex, North Cascades, Washington. Geological Society of America Bulletin, 96, 27-42.

Miller, R.B., Brown, E.H., McShane, D.P., and Whitney, D.L. (1993) Intra-arc crustal loading and its tectonic implications, North Cascades crystalline core, Washington and British Columbia. Geology, 21, 255-258.

Miller, R.B., Matzel, J.P., Paterson, S.R., and Stowell, H. (2003) Cretaceous to Paleogene Cascades Arc: Structure, metamorphism, and timescales of magmatism, burial, and exhumation of a crustal section, *in* Swanson, T.W., ed., Western Cordillera and adjacent areas. Geological Society of America Field Guide, 4, 107–135.

Miller, R.B. and Paterson, S.R. (1992) Tectonic implications of syn- and post-emplacement deformation of the Mount Stuart batholith for Mid-Cretaceous orogenesis in the North Cascades. Canadian Journal of Earth Science, 29, 479-485.

Miller, R.B. and Paterson, S.R. (1999) In defense of magmatic diapirs. Journal of Structural Geology, 21, 1161-1173.

Miller, R.B. and Paterson, S.R. (2001) Influence of lithological heterogeneity, mechanical anisotropy, and magmatism on the rheology of an arc, North Cascades, Washington. Tectonophysics, 342, 351-370.

Miller R.B., Paterson, S.R., DeBari, S.M., and Whitney, D.L. (2000) North Cascades Cretaceous crustal section: Changing kinematics, rheology, metamorphism, pluton emplacement, and petrogenesis from 0 to 40 kilometers depth. *in*, G.J. Woodsworth, L.E. Jackson, J.L. Nelson and B.C. Ward, eds., Guidebook for Geological Field Trips in Southwestern British Columbia and Northern Washington. Geological Society of America, 229-278.

Misch, P. (1966) Tectonic evolution of the Northern Cascades of Washington State: A west-Cordilleran case history, *in*, H. C. Gunning, ed., A Symposium on the Tectonic History and Mineral Deposits in the Western Cordillera in British Columbia and Neighboring Parts of the United States. Canadian Institute of Mining and Metallurgy, 8, 101-148.

Monger, J.W.H. and Journey, J.M. (1994) Guide to the geology and tectonic evolution of the southern Coast Mountains, 97 p. Geological Survey of Canada.

Monger, J.W.H., Price, R.A., and Templeman-Kluit, D.J. (1982) Tectonic accretion and the origin of the two major metamorphic and plutonic welts in the Canadian Cordillera. Geology, 10, 70-75.

Nesse, W.D. (2004) Introduction to Optical Mineralogy (third edition), 348 p. Oxford University Press, New York, New York.

O'Nions, R.K., Hamilton, P.J. and Evensen, N.M. (1977) Variations in 143Nd/144Nd and $^{87}Sr/^{86}Sr$ in oceanic basalts, Earth and Science Planetary Letters, 34, 13-22.

Passchier, C.W. and Trouw, R.A.J (1998) Microtectonics, 289 p. Springer, New York, N.Y.

Paterson, S.R. and Miller, R. B. (1998a) Magma emplacement during arc-perpendicular shortening; an example from the Cascades crystalline core, Washington. Tectonics, 17 (4), 571-586.

Paterson, S.R. and Miller, R. B. (1998b) Mid-crustal magmatic sheets in the Cascades Mountains, Washington: Implications for magma ascent. Journal of Structural Geology, 20, 1345-1363.

Paterson, S.R. and Miller, R. B. (1998c) Regional tilt of the Mount Stuart batholith, Washington, determined using aluminum-in-hornblende barometry: Implications for northward translation of Baja British Columbia: Discussion and Reply. Geological Society of America Bulletin, 110, 685-690.

Paterson, S.R., Miller, R.B., Alsleben, H., Whitney, D.L., Valley, P.M., and Hurlow, H. (2004) Driving mechanisms for >40 km of exhumation during contraction and extension in a continental arc, Cascades core, Washington. Tectonics, 23, TC3005, 1-30.

Paterson, S.R., Miller, R.B., Anderson, J.L., Lund, S., Bendixen, J., Taylor, N., and Fink, T. (1994) Emplacement and evolution of the Mt. Stuart batholith. In D.A. Swanson, and Haugerud, R.A., Eds., Geologic Field trips in the Pacific northwest, 2, Chapter 2F, Annual Meeting of the Geological Society of America, 47 p. Department of Geological Sciences, University of Washington in conjunction with the Geological Society of America.

Pattison, D.R.M. (2001) Instability of Al_2SiO_5 'triple point' assemblages in muscovite+biotite+quartz-bearing metapelites, with implications. American Mineralogist, 86, 1414-1422.

Pearce, J. A., Harris, N.W., and Tindle, A.G. (1984) Trace element discrimination diagrams for the tectonic interpretation of granitic rocks. Journal of Petrology, 25, 956-983.

Plummer, C.C. (1980) Dynamothermal contact metamorphism superposed on regional metamorphism in the pelitic rocks of the Chiwaukum Mountains area, Washington Cascades. Geological Society of America Bulletin, 91(II), 1627-1668.

Rubin, C.M., Saleeby, J.B., Cowan, D.S., Brandon, M.T., and McGroder, M.F. (1990) Regionally extensive west-vergent thrust system in the northwestern Cordillera: Implications for continent-margin tectonism. Geology, 18, 276-280.

Scherer, E.E., Cameron, K.L., and Blichert-Toft, J. (2000) Lu-Hf garnet geochronology: Closure temperature relative to Sm-Nd system and the effects of trace mineral inclusions. Geochemica et Cosmochimica Acta, 64, 3413-3432.

Stacey, J.S. and Kramers, J.D. (1975) Approximation of terrestrial lead isotope evolution by a two-stage model. Earth and Planetary Science Letters, 26, 207-221.

Stowell, H.H., Bulman, G.R., Zuluaga, C.Z., Tinkham, D.K., Miller, R.B., and Stein, E., (accepted), Mid-crustal Late Cretaceous metamorphism in the Nason terrane, Cascades crystalline core, Washington, USA: Implications for tectonic models. In R. Hatcher, Ed., Proceedings of the International Basement Tectonics Association 2004 Meeting, Geological Society of America.

Stowell, H.H. and Goldberg, S.A. (1997) Sm-Nd garnet dating of polyphase metamorphism: northern Coast Mountains, south-eastern Alaska, USA. Journal of Metamorphic Geology, 15, 439-450.

Stowell, H.H., Stein, E. (2005) The significance of plagioclase-dominant coronas on garnet, Wenatchee block, northern Cascades, Washington, U.S.A.. Canadian Mineralogist, 43, 367-385.

Stowell, H.H., Taylor, D.L., Tinkham, D.K., Goldberg, S.A., and Ouderkirk, K.A. (2001) Contact metamorphic P-T-t Paths from Sm-Nd Garnet Ages, Phase Equilibria Modeling, and Thermobarometry: Garnet Ledge, Southeastern Alaska. Journal of Metamorphic Geology, 19, 645-660.

Stowell, H.H. and Tinkham, D.K. (2003) Integration of Phase Equilibria Modeling and Garnet Sm-Nd Chronology for Construction of P-T-t Paths: Examples from the Cordilleran Coast Plutonic Complex, USA. In D. Vance, Muller, W., and Villa, I., Eds., Geochronology: Linking the isotopic record with petrology and textures. Geological Society Special Publication, 220, 119-145.

Sun, S.S. and McDonough, W.F. (1989) Chemical and isotopic systematics of oceanic basalts: implications for mantle composition and processes. In A.D. Saunders and Norry, M., Eds., Magmatism in Ocean Basins. Geological Society of London Special Publication, 313-345.

Tabor, R.W., Booth, D.B., Vance, J.A., and Ford, A.B. (2002) Geologic map of the Sauk River 30- by 60-minute quadrangle, Washington, 76 p. U.S. Geological Survey Map I-2592.

Tabor, R.W., Frizzell, V.A., Jr., Booth, D.B., Waitt, R.B., Whetten, J.T. and Zartman, R.E. (1993) Geologic map of the Skykomish River 30- by 60-minute Quadrangle, Washington, 42p. U. S. Geological Survey Map I-1963.

Tabor, R.W., Frizzell, V.A., Jr., Whetten, J.T., Waitt, R.B., Jr., Swanson, D.A., Byerly, G.R., Booth, D.B., Hetherington, M.J. and Zartman, R.E. (1987) Geologic map of the Chelan 30' by 60' Quadrangle, Washington, 29 p. U. S. Geological Survey Map I-1661.

Thirwall, M.F. (1991) Long term reproducibility of multicollector Sr and Nd isotope ratio analyses. Chemical Geology, 94, 85–104.

Thompson, A.B. and England, P.C. (1984) Pressure-temperature-time paths of regional metamorphism II. Their inference and interpretation using mineral assemblages in metamorphic rocks. Journal of Petrology, 25 (4), 929-955.

Thöni, M. (2002) Sm-Nd isotope systematics in garnet from different lithologies (Eastern Alps): Age results, and an evaluation of potential problems for garnet Sm-Nd chronometry. Chemical Geology, 185, 255-281.

Tinkham, D.K. (2002) MnNCKFMASH Phase equilibria, garnet activity modeling, and garnet samarium-neodymium chronology: Applications to the Waterville Formation, Maine, and south-central Nason terrane, Washington, Ph.D. thesis, 176 p. Tuscaloosa, Alabama, The University of Alabama.

Tomaschek, F., Kennedy, A.K., Villa, I.M., Lagos, M., and Ballhaus, C. (2003) Zircons from Syros, Cyclades, Greece—recrystallization and mobilization of zircon during high-pressure metamorphism. Journal of Petrology, 44 (11), 1977-2002.

Umhoefer, P. J. and Miller, R. B., 1996, Mid-Cretaceous thrusting in the southern Coast Belt, British Columbia and Washington, after strike-slip fault reconstruction. Tectonics, v. 15, p. 545-565.

Valley, P.M., Whitney, D.L., Paterson, S.R., Miller, R.B., and Alsleben, H. (2003) Metamorphism of the deepest exposed arc rocks in the Cretaceous to Paleogene Cascades belt, Washington: Evidence for large-scale vertical motion in a continental arc. Journal of Metamorphic Geology, 21, 203-220.

Vance, D., Muller, W., and Villa, M. (2003) Geochronology: Linking the isotopic record with petrology and textures—an introduction. In D. Vance, Muller, W., and Villa, I., Eds., Geochronology: Linking the isotopic record with petrology and textures. Geological Society Special Publication, 220, 119-145.

Vance, D. and O'Nions, R.K. (1990) Isotopic chronometry of zoned garnets: Growth kinetics and metamorphic histories. Earth and Planetary Science Letters, 97, 227-240.

Van Diver, B. (1968) Origin of Jove Peak Orbiculite in Wenatchee Ridge Area, Northern Cascades, Washington. American Journal of Science, 266, 110-123.

Walker, N.W. and Brown, E.H. (1991) Is the southeast Coast Plutonic Complex the consequence of the accretion of the Insular superterrane? Evidence from U-Pb zircon geochronometry in the northern Washington Cascades. Geology, 19, 714-717.

Wasserburg, G.J., Jacobsen, S.B., DePaolo, D.J., and McCulloch, M.T. (1981) Precise determination of Sm/Nd ratios, Sm and Nd isotopic abundances in standard solutions. Geochemica et Cosmochimica Acta, 45, 2311-2323.

Weaver, B.L. and Tarney, J. (1984) Major and trace element composition of the continental lithosphere. In Structure and Evolution of the Continental Lithosphere, H.N. Pollack and V.R. Murthy, Eds., Pergamon. New York, New York, 39-68.

Whitney, D.L. and McGroder, M.F. (1989) Cretaceous crustal section through the proposed Insular-Intermontane suture, North Cascades, Washington. Geology, 17, 555-558.

Whitney, D. L., Miller, R. B., and Paterson, S. R. (1999) P-T-t evidence for mechanisms of vertical tectonic motion in a contractional orogen; north-western US and Canadian Cordillera. Journal of Metamorphic Geology, 17 (1), 75-90.

Williams, I.S. and Claesson, S. (1987) Isotopic evidence for the Precambrian provenance and Caledonian metamorphism of high grade paragneisses from the Seve Nappes, Scandinavian Caledonides. Contributions to Mineralogy and Petrology, 97, 204-217.

Wyld, S.J., Umhoefer, P., and Wright, J.E. (in press) Paleogeography of Western North America: Constraints on latitudinal displacements. Geological Association of Canada Special Paper.

York, D. (1969) Least-squares fitting of a straight line, Earth and Planetary Letters, 5, 320-324.

Zen, E-an (1988) Tectonic significance of high-pressure plutonic rocks in the western Cordillera. In W.G. Ernst, Ed., Metamorphism and crustal evolution of the Western United States, Rubey Volume VII, New Jersey, Prentice Hall, 41-68.

Zhou, B. and Hensen, B. (1995) Inherited Sm/Nd isotope components preserved in monazite inclusions within garnets in leucogneiss from East Antartica and implications for closure temperature studies. Chemical Geology, 121, 317-326.

Zuluaga, C.A. (2004) Thermodynamic modeling applied to metamorphic processes in migmatites: An example form the Nason Ridge Migmatitic Gneiss (Cascades Core, WA), Ph.D. thesis, 176 p. Tuscaloosa, Alabama, The University of Alabama.

APPENDIX A
STRUCTURAL DATA AND STATION LOCATIONS

Latitude and Longitude are given in decimal degrees for the NAD 27 coordinate system. This is a summary table with representative or locally averaged map-scale data; additional data accompany stereonet plots and outcrop-scale data tables. Structural-lithologic domains: (1) a. Mount Stuart batholith b. Chiwaukum schist blocks/rafts in MS batholith c. orbiculite; (2) Chiwaukum schist; (3) granodiorite intrusive bodies, Kbgg; (4) Nason Ridge Migmatitic Gneiss; (5) Schist blocks/rafts in Kbgg bodies. Planar type: Fault, Fracture, Vein, Impregnated Fracture, Contact, Dike, Sill, Schistosity, Gneissosity, Axial Surface. Linear type: Mineral, Slickenside, Fold Axis. Azimuth refers to strike or trend. Angle refers to dip or plunge. Strike and dip measurements use right-hand-rule convention.

Location	Longitude	Latitude	Structural-Lithologic Zone	Linear or Planar?	Type	Azimuth	Angle	Direction
03NCGB124	-121.03752	47.85022	3	P	Gneissosity	315	36	NE
03NCGB124	-121.03752	47.85022	5	P	Contact	315	36	NE
03NCGB124	-121.03752	47.85022	5	P	Dike	300	75	NE
03NCGB124	-121.03752	47.85022	5	P	Schistosity	120	84	SW
03NCGB125	-121.03750	47.85013	3	P	Dike	308	49	NE
03NCGB125	-121.03750	47.85013	5	P	Contact	308	49	NE
03NCGB125	-121.03750	47.85013	5	P	Schistosity	126	55	SW
03NCGB126	-121.03995	47.85118	5	P	Schistosity	120	80	SW
03NCGB128	-121.04022	47.85272	3	P	Dike	55	66	SE
03NCGB130	-121.03803	47.84242	5	P	Gneissosity	115	15	SW
03NCGB130	-121.03803	47.84242	5	L	Mineral	133	0	SE
03NCGB130	-121.03803	47.84242	5	P	Schistosity	115	15	SW
03NCGB131	-121.03842	47.84235	5	P	Schistosity	135	90	V
03NCGB132	-121.03972	47.84233	5	P	Contact	138	61	SW
03NCGB132	-121.03972	47.84233	5	P	Schistosity	138	61	SW
03NCGB133	-121.04068	47.84317	3	P	Gneissosity	145	78	SW
03NCGB134	-121.04207	47.84420	5	P	Dike	140	50	SW
03NCGB134	-121.04207	47.84420	5	P	Schistosity	132	66	SW
03NCGB136	-121.03927	47.84227	5	L	Mineral	185	20	S
03NCGB136	-121.03927	47.84227	5	P	Schistosity	150	31	SW

Location	Longitude	Latitude	Structural-Lithologic Zone	Linear or Planar?	Type	Azimuth	Angle	Direction
03NCGB137	-121.04283	47.84350	5	P	Contact	120	83	SW
03NCGB138	-121.04382	47.84350	5	P	Gneissosity	310	87	NE
03NCGB138	-121.04382	47.84350	5	P	Gneissosity	130	76	SW
03NCGB138	-121.04382	47.84350	5	L	Mineral	125	8	SE
03NCGB138	-121.04382	47.84350	5	L	Mineral	130	5	SE
03NCGB138	-121.04382	47.84350	5	P	Schistosity	130	76	SW
03NCGB138	-121.04382	47.84350	5	P	Schistosity	310	87	NE
03NCGB140	-121.05623	47.84182	5	P	Gneissosity	130	90	V
03NCGB140	-121.05623	47.84182	5	P	Schistosity	130	90	V
03NCGB141	-121.04804	47.84123	4	P	Axial Surface	144	78	SW
03NCGB141	-121.04804	47.84123	4	L	Fold Axis	320	3	NW
03NCGB141	-121.04804	47.84123	4	P	Gneissosity	144	78	SW
03NCGB141	-121.04804	47.84123	4	P	Schistosity	144	78	SW
03NCGB142	-121.04728	47.84150	4	P	Schistosity	130	90	V
03NCGB143	-121.04605	47.84261	4	P	Schistosity	310	90	V
03NCGB146	-121.06183	47.83668	5	P	Gneissosity	315	85	NE
03NCGB146	-121.06183	47.83668	5	P	Schistosity	315	85	NE
03NCGB148	-121.06372	47.83567	2	P	Gneissosity	310	86	NE
03NCGB148	-121.06372	47.83567	2	P	Schistosity	310	86	NE
03NCGB149	-121.06460	47.83440	2	L	Mineral	87	86	E
03NCGB149	-121.06460	47.83440	2	P	Schistosity	312	88	NE

Location	Longitude	Latitude	Structural-Lithologic Zone	Linear or Planar?	Type	Azimuth	Angle	Direction
03NCGB150	-121.06707	47.83138	2	P	Schistosity	135	71	SW
03NCGB151	-121.06888	47.83032	2	P	Gneissosity	161	49	SW
03NCGB151	-121.06888	47.83032	2	P	Gneissosity	264	30	N
03NCGB151	-121.06888	47.83032	2	P	Schistosity	264	30	N
03NCGB151	-121.06888	47.83032	2	P	Schistosity	161	49	SW
03NCGB153	-121.07105	47.82571	2	P	Schistosity	330	90	V
03NCGB154	-121.07262	47.82490	2	P	Contact	315	67	NE
03NCGB155	-121.07295	47.82403	1b	P	Gneissosity	341	84	NE
03NCGB156	-121.04664	47.84220	4	P	Gneissosity	308	85	NE
03NCGB156	-121.04664	47.84220	4	P	Schistosity	308	85	NE
03NCGB157	-121.04086	47.85043	5	P	Axial Surface	115	78	SW
03NCGB157	-121.04086	47.85043	5	L	Fold Axis	300	11	NW
03NCGB157	-121.04086	47.85043	5	P	Gneissosity	125	66	SW
03NCGB157	-121.04086	47.85043	5	P	Schistosity	304	90	NE
03NCGB157	-121.04086	47.85043	5	P	Schistosity	125	66	SW
03NCGB158	-121.04070	47.85000	5	P	Gneissosity	307	73	NE
03NCGB158	-121.04070	47.85000	5	P	Schistosity	307	73	NE
03NCGB159	-121.04027	47.85205	3	P	Dike	138	8	SW
03NCGB159	-121.04027	47.85205	3	P	Dike	79	77	SE
03NCGB159	-121.04027	47.85205	3	P	Fracture	202	50	NW

Location	Longitude	Latitude	Structural-Lithologic Zone	Linear or Planar?	Type	Azimuth	Angle	Direction
04NCGB001	-121.04014	47.85337	5	P	Contact	280	75	NE
04NCGB001	-121.04014	47.85337	5	L	Fold Axis	114	2	SE
04NCGB001	-121.04014	47.85337	5	P	Gneissosity	110	38	SW
04NCGB001	-121.04014	47.85337	5	P	Schistosity	110	38	SW
04NCGB002	-121.02475	47.84309	5	P	Contact	132	38	SW
04NCGB002	-121.02475	47.84309	5	L	Fold Axis	323	27	NW
04NCGB002	-121.02475	47.84309	5	P	Gneissosity	132	38	SW
04NCGB002	-121.02475	47.84309	5	P	Schistosity	132	38	SW
04NCGB003	-121.02335	47.84760	3	P	Gneissosity	151	35	SW
04NCGB003	-121.02335	47.84760	5	L	Fold Axis	296	3	NW
04NCGB003	-121.02335	47.84760	5	P	Schistosity	167	58	SW
04NCGB004	-121.07301	47.82244	1b	P	Gneissosity	308	29	NE
04NCGB004	-121.07301	47.82244	1b	P	Gneissosity	356	32	E
04NCGB005	-121.07298	47.82416	1b	P	Contact	312	75	NE
04NCGB005	-121.07298	47.82416	1b	P	Gneissosity	312	75	NE
04NCGB005	-121.07298	47.82416	1c	P	Gneissosity	330	61	NE
04NCGB005	-121.07298	47.82416	1c	P	Vein	128	62	SW
04NCGB005	-121.07298	47.82416	1c	P	Vein	221	75	NW
04NCGB005	-121.07298	47.82416	1c	P	Vein	221	75	NW
04NCGB005	-121.07298	47.82416	1c	P	Vein	129	61	SW

Location	Longitude	Latitude	Structural-Lithologic Zone	Linear or Planar?	Type	Azimuth	Angle	Direction
04NCGB006	-121.07281	47.82491	2	P	Dike	12	61	E
04NCGB006	-121.07281	47.82491	2	P	Gneissosity	328	72	NE
04NCGB007	-121.07102	47.82588	2	P	Schistosity	314	70	NE
04NCGB008	-121.07146	47.82574	2	P	Contact	296	62	NE
04NCGB009	-121.06937	47.82590	2	P	Gneissosity	304	38	NE
04NCGB009	-121.06937	47.82590	2	P	Schistosity	304	38	NE
04NCGB010	-121.07026	47.82588	2	P	Gneissosity	306	33	NE
04NCGB010	-121.07026	47.82588	2	P	Schistosity	306	33	NE
04NCGB011	-121.06935	47.83068	2	L	Fold Axis	330	11	NW
04NCGB011	-121.06935	47.83068	2	P	Fracture	244	43	NW
04NCGB011	-121.06935	47.83068	2	P	Fracture	108	58	SW
04NCGB011	-121.06935	47.83068	2	P	Gneissosity	161	48	SW
04NCGB011	-121.06935	47.83068	2	P	Gneissosity	335	29	NE
04NCGB011	-121.06935	47.83068	2	P	Schistosity	335	29	NE
04NCGB011	-121.06935	47.83068	2	P	Schistosity	161	48	SW
04NCGB012	-121.06892	47.83001	2	L	Fold Axis	324	25	NW
04NCGB012	-121.06892	47.83001	2	L	Fold Axis	320	11	NW
04NCGB012	-121.06892	47.83001	2	P	Gneissosity	145	63	SW
04NCGB012	-121.06892	47.83001	2	P	Gneissosity	292	23	NE
04NCGB012	-121.06892	47.83001	2	P	Schistosity	145	63	SW

Location	Longitude	Latitude	Structural-Lithologic Zone	Linear or Planar?	Type	Azimuth	Angle	Direction
04NCGB012	-121.06892	47.83001	2	P	Schistosity	292	23	NE
04NCGB013	-121.06894	47.82933	2	P	Gneissosity	295	46	NE
04NCGB013	-121.06894	47.82933	2	P	Schistosity	295	46	NE
04NCGB014	-121.06891	47.82879	2	P	Axial Surface	298	50	NE
04NCGB014	-121.06891	47.82879	2	L	Fold Axis	311	10	NW
04NCGB014	-121.06891	47.82879	2	P	Gneissosity	310	54	NE
04NCGB014	-121.06891	47.82879	2	P	Schistosity	310	54	NE
04NCGB015	-121.06905	47.82773	2	L	Fold Axis	320	11	NW
04NCGB015	-121.06905	47.82773	2	P	Gneissosity	321	36	NE
04NCGB015	-121.06905	47.82773	2	P	Schistosity	321	36	NE
04NCGB016	-121.06189	47.82290	1b	P	Contact	313	58	NE
04NCGB016	-121.06189	47.82290	1b	P	Gneissosity	313	58	NE
04NCGB016	-121.06189	47.82290	1b	P	Schistosity	313	58	NE
04NCGB017	-121.06145	47.82294	2	P	Contact	310	45	NE
04NCGB017	-121.06145	47.82294	1a	P	Fracture	70	73	SE
04NCGB017	-121.06145	47.82294	1a	P	Vein	7	82	E
04NCGB017	-121.06145	47.82294	1a	P	Vein	342	86	NE
04NCGB017	-121.06145	47.82294	1a	P	Vein	283	59	NE
04NCGB017	-121.06145	47.82294	1b	P	Gneissosity	310	45	NE
04NCGB018	-121.05325	47.82573	2	P	Sill	156	75	SW

Location	Longitude	Latitude	Structural-Lithologic Zone	Linear or Planar?	Type	Azimuth	Angle	Direction
04NCGB018	-121.05325	47.82573	2	P	Gneissosity	325	82	NE
04NCGB018	-121.05325	47.82573	2	P	Schistosity	325	82	NE
04NCGB019	-121.05438	47.82538	2	P	Gneissosity	310	79	NE
04NCGB020	-121.05668	47.82465	2	P	Gneissosity	320	72	NE
04NCGB021	-121.06252	47.82279	1a	P	Fracture	38	79	SE
04NCGB021	-121.06252	47.82279	1a	P	Fracture	51	72	SE
04NCGB021	-121.06252	47.82279	1a	P	Fracture	298	75	NE
04NCGB021	-121.06252	47.82279	1a	P	Fracture	329	68	NE
04NCGB021	-121.06252	47.82279	1a	P	Vein	5	90	V
04NCGB021	-121.06252	47.82279	1a	P	Vein	345	79	NE
04NCGB022	-121.06794	47.82183	1b	P	Contact	326	85	NE
04NCGB022	-121.06794	47.82183	1b	P	Gneissosity	326	85	NE
04NCGB023	-121.06744	47.82183	1b	P	Contact	335	70	NE
04NCGB024	-121.07125	47.82245	1c	P	Fracture	331	90	V
04NCGB024	-121.07125	47.82245	1c	P	Vein	156	73	SW
04NCGB025	-121.05885	47.84404	4	P	Contact	130	72	SW
04NCGB025	-121.05885	47.84404	4	P	Dike	219	48	NW
04NCGB025	-121.05885	47.84404	4	L	Fold Axis	128	2	SE
04NCGB025	-121.05885	47.84404	4	P	Gneissosity	130	72	SW
04NCGB026	-121.03750	47.85013	4	P	Gneissosity	142	65	SW

Location	Longitude	Latitude	Structural-Lithologic Zone	Linear or Planar?	Type	Azimuth	Angle	Direction
04NCGB026	-121.03750	47.85013	4	P	Sill	118	90	V
04NCGB026	-121.03750	47.85013	4	P	Sill	142	65	SW
04NCGB026	-121.03750	47.85013	4	P	Vein	285	55	NE
04NCGB027	-121.03981	47.85123	4	P	Dike	52	70	SE
04NCGB027	-121.03981	47.85123	4	P	Dike	258	49	NW
04NCGB027	-121.03981	47.85123	5	P	Contact	121	76	SW
04NCGB027	-121.03981	47.85123	5	L	Fold Axis	118	8	SE
04NCGB027	-121.03981	47.85123	5	P	Gneissosity	121	76	SW
04NCGB028	-121.03943	47.85071	3	P	Dike	265	45	N
04NCGB028	-121.03943	47.85071	3	P	Dike	153	45	SW
04NCGB028	-121.03943	47.85071	5	P	Contact	135	54	SW
04NCGB028	-121.03943	47.85071	5	L	Fold Axis	329	14	NW
04NCGB028	-121.03943	47.85071	5	P	Gneissosity	154	61	SW
04NCGB029	-121.04121	47.85335	5	P	Contact	125	41	SW
04NCGB029	-121.04121	47.85335	5	P	Gneissosity	125	41	SW
04NCGB035	-121.04637	47.84241	4	P	Dike	331	90	V
04NCGB035	-121.04637	47.84241	4	L	Fold Axis	310	70	NW
04NCGB035	-121.04637	47.84241	4	P	Schistosity	133	72	SW
04NCGB035	-121.04637	47.84241	4	P	Schistosity	310	90	V
04NCGB035	-121.04637	47.84241	4	P	Sill	133	72	SW

Location	Longitude	Latitude	Structural-Lithologic Zone	Linear or Planar?	Type	Azimuth	Angle	Direction
04NCGB035	-121.04637	47.84241	4	P	Sill	320	73	NE
04NCGB035	-121.04637	47.84241	4	P	Sill	127	77	SW
04NCGB036	-121.04683	47.84209	4	P	Dike	330	86	NE
04NCGB036	-121.04683	47.84209	4	P	Dike	285	46	NE
04NCGB036	-121.04683	47.84209	4	L	Fold Axis	294	57	NW
04NCGB036	-121.04683	47.84209	4	L	Fold Axis	314	2	NW
04NCGB036	-121.04683	47.84209	4	L	Fold Axis	330	90	V
04NCGB036	-121.04683	47.84209	4	P	Gneissosity	125	81	SW
04NCGB036	-121.04683	47.84209	4	P	Gneissosity	311	90	NE
04NCGB036	-121.04683	47.84209	4	P	Schistosity	125	81	SW
04NCGB036	-121.04683	47.84209	4	P	Sill	129	84	SW
04NCGB036	-121.04683	47.84209	4	P	Sill	136	85	SW
04NCGB037	-121.04724	47.84183	4	P	Dike	184	57	W
04NCGB037	-121.04724	47.84183	4	P	Dike	115	81	SW
04NCGB037	-121.04724	47.84183	4	P	Gneissosity	147	73	SW
04NCGB037	-121.04724	47.84183	4	P	Gneissosity	149	76	SW
04NCGB037	-121.04724	47.84183	4	P	Gneissosity	330	81	NE
04NCGB038	-121.04182	47.84418	5	P	Contact	110	72	SW
04NCGB038	-121.04182	47.84418	5	P	Dike	75	80	SE
04NCGB038	-121.04182	47.84418	5	P	Gneissosity	110	72	SW

Location	Longitude	Latitude	Structural-Lithologic Zone	Linear or Planar?	Type	Azimuth	Angle	Direction
04NCGB039	-121.04224	47.84398	3	P	Contact	150	57	SW
04NCGB040	-121.04300	47.84370	4	P	Contact	150	57	SW
04NCGB040	-121.04300	47.84370	4	P	Gneissosity	150	57	SW
04NCGB041	-121.04355	47.84353	4	P	Gneissosity	310	80	NE
04NCGB041	-121.04355	47.84353	4	P	Schistosity	310	80	NE
04NCGB042	-121.04412	47.84326	4	P	Gneissosity	123	62	SW
04NCGB042	-121.04412	47.84326	4	P	Schistosity	123	62	SW
04NCGB043	-121.04473	47.84300	4	P	Gneissosity	126	80	SW
04NCGB043	-121.04473	47.84300	4	P	Schistosity	126	80	SW
04NCGB044	-121.04545	47.84275	4	P	Fault	328	88	NE
04NCGB044	-121.04545	47.84275	4	P	Fault	163	84	SW
04NCGB044	-121.04545	47.84275	4	P	Fault	155	83	SW
04NCGB044	-121.04545	47.84275	4	P	Fault	308	84	NE
04NCGB044	-121.04545	47.84275	4	P	Fault	325	68	NE
04NCGB044	-121.04545	47.84275	4	P	Gneissosity	145	66	SW
04NCGB044	-121.04545	47.84275	4	L	Slickensides	328	18	NW
04NCGB044	-121.04545	47.84275	4	L	Slickensides	146	5	SE
04NCGB044	-121.04545	47.84275	4	L	Slickensides	124	31	SE
04NCGB044	-121.04545	47.84275	4	L	Slickensides	314	11	NW
04NCGB044	-121.04545	47.84275	4	L	Slickensides	128	40	SE

Location	Longitude	Latitude	Structural-Lithologic Zone	Linear or Planar?	Type	Azimuth	Angle	Direction
04NCGB045	-121.05168	47.84130	4	P	Gneissosity	310	56	NE
04NCGB045	-121.05168	47.84130	4	P	Schistosity	310	56	NE
04NCGB046	-121.05376	47.84176	4	P	Contact	309	73	NE
04NCGB046	-121.05376	47.84176	4	P	Gneissosity	309	73	NE
04NCGB047	-121.05521	47.84206	4	P	Contact	320	80	NE
04NCGB048	-121.04754	47.84161	4	P	Dike	326	90	V
04NCGB048	-121.04754	47.84161	4	P	Fold Axis	315	4	NW
04NCGB048	-121.04754	47.84161	4	P	Gneissosity	125	87	SW
04NCGB048	-121.04754	47.84161	4	P	Gneissosity	136	89	SW
04NCGB048	-121.04754	47.84161	4	P	Schistosity	125	87	SW
04NCGB048	-121.04754	47.84161	4	P	Schistosity	136	89	SW
04NCGB048	-121.04754	47.84161	4	P	Sill	121	78	SW
04NCGB049	-121.04500	47.84290	4	P	Contact	145	65	SW
04NCGB050	-121.04572	47.84274	4	P	Contact	129	88	SW
04NCGB051	-121.04206	47.85299	3	P	Dike	275	55	NE
04NCGB051	-121.04206	47.85299	3	P	Dike	105	77	SW
04NCGB051	-121.04206	47.85299	3	P	Impregnated Fracture	204	55	NW
04NCGB051	-121.04206	47.85299	3	P	Impregnated Fracture	211	35	NW
04NCGB052	-121.04221	47.85216	3	P	Dike	195	46	SW
04NCGB052	-121.04221	47.85216	3	P	Dike	305	75	NE

Location	Longitude	Latitude	Structural-Lithologic Zone	Linear or Planar?	Type	Azimuth	Angle	Direction
04NCGB052	-121.04221	47.85216	3	P	Dike	114	83	SW
04NCGB052	-121.04221	47.85216	3	P	Impregnated Fracture	220	63	NW
04NCGB052	-121.04221	47.85216	5	P	Contact	285	82	NE
04NCGB052	-121.04221	47.85216	5	P	Gneissosity	285	82	NE
04NCGB053	-121.04196	47.85138	3	P	Dike	189	68	W
04NCGB053	-121.04196	47.85138	3	P	Dike	40	70	SE
04NCGB053	-121.04196	47.85138	3	P	Fault	256	57	NW
04NCGB053	-121.04196	47.85138	3	L	Slickensides	36	26	NE
04NCGB054	-121.04164	47.85077	3	P	Dike	67	70	SW
04NCGB054	-121.04164	47.85077	5	P	Axial Surface	129	66	SW
04NCGB054	-121.04164	47.85077	5	P	Contact	121	75	SW
04NCGB054	-121.04164	47.85077	5	P	Contact	297	66	NE
04NCGB054	-121.04164	47.85077	5	L	Fold Axis	315	20	NW
04NCGB054	-121.04164	47.85077	5	P	Gneissosity	299	90	V
04NCGB054	-121.04164	47.85077	5	P	Gneissosity	116	74	SW
04NCGB054	-121.04164	47.85077	5	P	Schistosity	299	90	V
04NCGB054	-121.04164	47.85077	5	P	Schistosity	116	74	SW
04NCGB055	-121.04169	47.85034	5	P	Dike	316	80	NE
04NCGB055	-121.04169	47.85034	5	L	Fold Axis	302	29	NW
04NCGB055	-121.04169	47.85034	5	P	Gneissosity	128	60	SW

Location	Longitude	Latitude	Structural-Lithologic Zone	Linear or Planar?	Type	Azimuth	Angle	Direction
04NCGB055	-121.04169	47.85034	5	P	Schistosity	128	60	SW
04NCGB056	-121.04142	47.84986	3	P	Dike	120	65	SW
04NCGB056	-121.04142	47.84986	3	P	Fault	105	74	SW
04NCGB056	-121.04142	47.84986	3	P	Fault	131	74	SW
04NCGB056	-121.04142	47.84986	3	P	Fracture	200	52	W
04NCGB056	-121.04142	47.84986	3	L	Slickensides	109	4	SE
04NCGB056	-121.04142	47.84986	5	P	Contact	120	65	SW
04NCGB057	-121.04187	47.84885	5	P	Contact	357	26	E
04NCGB057	-121.04187	47.84885	5	P	Contact	83	86	S
04NCGB057	-121.04187	47.84885	5	P	Fault	357	26	E
04NCGB057	-121.04187	47.84885	5	P	Fault	83	36	S
04NCGB057	-121.04187	47.84885	5	L	Fold Axis	120	6	SE
04NCGB057	-121.04187	47.84885	5	P	Schistosity	108	15	SW
04NCGB057	-121.04187	47.84885	5	L	Slickensides	126	13	SE
04NCGB057	-121.04187	47.84885	5	L	Slickensides	119	21	SE
04NCGB058	-121.04133	47.84794	5	P	Contact	112	50	SW
04NCGB058	-121.04133	47.84794	5	P	Fault	180	32	W
04NCGB058	-121.04133	47.84794	5	P	Fault	305	74	NE
04NCGB058	-121.04133	47.84794	5	L	Slickensides	320	12	NW
04NCGB058	-121.04133	47.84794	5	L	Slickensides	290	30	W

Location	Longitude	Latitude	Structural-Lithologic Zone	Linear or Planar?	Type	Azimuth	Angle	Direction
04NCGB059	-121.04146	47.84722	3	P	Fault			
04NCGB059	-121.04146	47.84722	5	P	Contact	128	72	SW
04NCGB059	-121.04146	47.84722	5	P	Gneissosity	128	72	SW
04NCGB059	-121.04146	47.84722	5	P	Schistosity	128	72	SW
04NCGB060	-121.04187	47.84545	5	L	Fold Axis	129	10	SE
04NCGB060	-121.04187	47.84545	5	P	Gneissosity	100	31	SW
04NCGB060	-121.04187	47.84545	5	P	Gneissosity	129	90	V
04NCGB060	-121.04187	47.84545	5	P	Gneissosity	75	7	SE
04NCGB060	-121.04187	47.84545	5	P	Schistosity	129	90	V
04NCGB060	-121.04187	47.84545	5	P	Schistosity	75	7	SE
04NCGB060	-121.04187	47.84545	5	P	Schistosity	100	31	SW
04NCGB061	-121.04200	47.84473	5	P	Contact	310	53	NE
04NCGB061	-121.04200	47.84473	5	P	Schistosity	310	53	NE
04NCGB062	-121.04202	47.84462	3	P	Dike	53	90	V
04NCGB062	-121.04202	47.84462	5	P	Gneissosity	167	48	SW
04NCGB062	-121.04202	47.84462	5	P	Schistosity	167	48	SW
04NCGB063	-121.03952	47.85371	5	P	Contact	115	56	SW
04NCGB063	-121.03952	47.85371	5	P	Schistosity	115	56	SW
04NCGB064	-121.07035	47.82593	2	P	Gneissosity	330	70	NE
04NCGB064	-121.07035	47.82593	2	P	Schistosity	330	70	NE

Location	Longitude	Latitude	Structural-Lithologic Zone	Linear or Planar?	Type	Azimuth	Angle	Direction
04NCGB065	-121.03993	47.85112	3	P	Dike	74	49	SE
04NCGB065	-121.03993	47.85112	3	P	Dike	117	57	SW
04NCGB065	-121.03993	47.85112	3	P	Gneissosity	140	72	SW
04NCGB065	-121.03993	47.85112	5	P	Contact	126	83	SW
04NCGB065	-121.03993	47.85112	5	L	Fold Axis	139	6	SE
04NCGB065	-121.03993	47.85112	5	P	Schistosity	130	90	V
04NCGB066	-121.04196	47.84447	5	P	Contact	116	65	SW
04NCGB066	-121.04196	47.84447	5	P	Gneissosity	116	65	SW
04NCGB066	-121.04196	47.84447	5	P	Schistosity	116	65	SW
92GD611	-121.03762	47.82534	3	P	Gneissosity	319	77	NE
92GD613	-121.02038	47.82424	4	P	Axial Surface	123	88	SW
92GD613	-121.02038	47.82424	4	L	Fold Axis	123	2	SE
92GD613	-121.02038	47.82424	4	P	Schistosity	128	78	SW
92GD614	-121.01525	47.82273	3	P	Gneissosity	290	55	NE
92GD617	-121.06222	47.83140	2	P	Axial Surface	313	84	NE
92GD617	-121.06222	47.83140	2	P	Schistosity	313	84	NE
92GD617	-121.06222	47.83140	3	P	Gneissosity	320	88	NE
92GD618	-121.06295	47.83059	2	P	Schistosity	300	85	NE
92GD620	-121.06782	47.82982	2	P	Schistosity	321	84	NE
92GD621	-121.06545	47.82788	2	P	Schistosity	288	36	NE

Location	Longitude	Latitude	Structural-Lithologic Zone	Linear or Planar?	Type	Azimuth	Angle	Direction
92GD625	-121.06109	47.82310	1b	P	Schistosity	335	30	NE
92GD626	-121.05778	47.82413	2	P	Schistosity	355	48	E
92GD627	-121.05588	47.82481	2	P	Schistosity	320	70	NE
92GD628	-121.05441	47.82528	2	P	Schistosity	320	74	NE
92GD629	-121.05023	47.82687	2	P	Schistosity	298	75	NE
92GD632	-121.03281	47.83639	4	P	Gneissosity	140	47	SW
92GD632	-121.03281	47.83639	4	P	Gneissosity	135	73	SW
92GD632	-121.03281	47.83639	4	P	Schistosity	140	47	SW
92GD632	-121.03281	47.83639	4	P	Schistosity	135	73	SW
92GD633	-121.03677	47.84581	3	P	Gneissosity	306	67	NE
92GD634	-121.03544	47.84502	3	P	Gneissosity	105	17	SW
92GD635	-121.03551	47.84700	5	L	Fold Axis	305	5	NW
92GD635	-121.03551	47.84700	5	P	Schistosity	307	77	NE
92GD636	-121.03607	47.84820	3	P	Gneissosity	131	45	SW
92GD637	-121.03646	47.85025	3	P	Gneissosity	310	84	NE
92GD637	-121.03646	47.85025	5	P	Schistosity	127	74	SW
92GD638	-121.03927	47.85102	3	P	Gneissosity	304	83	NE
92GD639	-121.04158	47.85211	3	P	Gneissosity	130	69	SW
92GD639	-121.04158	47.85211	5	L	Fold Axis	304	3	NW
92GD639	-121.04158	47.85211	5	P	Schistosity	110	32	SW

Location	Longitude	Latitude	Structural-Lithologic Zone	Linear or Planar?	Type	Azimuth	Angle	Direction
92GD640	-121.04185	47.85342	3	P	Gneissosity	128	67	SW
93GD787	-121.06835	47.81974	1a	P	Gneissosity	335	63	NE
93GD788	-121.07202	47.82234	1b	P	Schistosity	313	73	NE
93GD789	-121.07275	47.82300	1b	P	Schistosity	320	45	NE
93GD790	-121.07263	47.82445	1b	P	Schistosity	310	40	NE
93GD792	-121.07104	47.82519	2	P	Schistosity	313	56	NE
93GD793	-121.06889	47.82635	2	P	Axial Surface	338	60	NE
93GD793	-121.06889	47.82635	2	P	Schistosity	338	60	NE
93GD794	-121.06900	47.82891	2	P	Schistosity	305	38	NE
93GD795	-121.06891	47.83061	2	P	Schistosity	302	30	NE
93GD825	-121.07024	47.82596	2	P	Axial Surface	335	64	NE
93GD825	-121.07024	47.82596	2	L	Fold Axis	345	35	NW
93GD825	-121.07024	47.82596	2	P	Schistosity	310	56	NE
93GD826	-121.06918	47.82744	2	P	Axial Surface	323	44	NE
93GD826	-121.06918	47.82744	2	L	Fold Axis	346	25	NW
93GD826	-121.06918	47.82744	2	P	Schistosity	323	44	NE
93GD828	-121.06889	47.83026	2	P	Schistosity	155	41	SW
93GD829	-121.06818	47.83070	2	P	Schistosity	337	88	NE

APPENDIX B
PETROGRAPHY

Sample	Structural-Lith. Zone	Number of T-Sections	Qtz	Pl	Kfs	Bt	Ms	Chl	Grt	St	And	Ky	Sil	Fib	Amp	Gr	Ilm	Rt	Other
92GD625A	2	1	X	X		X	X		X	X			X	X		X	X		And pseudomorph
92GD627A	2	1	X	X		X	X	X		X		X	X	X		X	X		And pseudomorph
92GD628A	2	1	X	X		X	X	X	X	X						X	X	X	
92GD635A	5	1	X	X		X	X		X	X		X				X	X	X	
92GD639A	5	1	X	X		X	X		X	X		X				X	X		
03NCGB124a	5	1	X	X		X	X												
03NCGB124b	5	1	X	X	X	X	X												<1% opaques
03NCGB126	3	2	X	X	X	X	X												Ap, Zr
03NCGB130b	3	2	X	X		X		X	X						X				
03NCGB133	3	1	X	X		X													
03NCGB134	5	1	X	X		X		X	X										
03NCGB138c	4	1	X	X		X	X		X	X				X					
03NCGB138b	4	1	X	X		X			X	X		X		X			X		
03NCGB138a	4	2	X	X		X			X	X							X		Talc (< 1%)

Sample	Structural-Lith. Zone	Number of T-Sections	Qtz	Pl	Kfs	Bt	Ms	Chl	Grt	St	And	Ky	Sil	Fib	Amp	Gr	Ilm	Rt	Other
03NCGB142	4	1	X	X		X	X	X											
03NCGB143	4		X	X		X			X										
03NCGB144	5	2	X	X		X			X										
03NCGB147	2	2	X	X		X	X		X	X				X					
03NCGB148	2	2	X	X		X			X	X				X					
03NCGB149	2	1	X	X		X		X	X										
03NCGB151	2	3	X	X		X	X	X	X	X				X					
03NCGB152	2	3	X	X		X	X		X	X				X		X	X		And pseudomorph
03NCGB156	4	1	X	X		X													
03NCGB158	5	2	X	X		X	X		X	X		X					?		Tourmaline
03NCHS19a	5	1	X	X		X	X		X	X		X		X					
03NCHS20	5	1	X	X		X			X										
04NCGB003A	5	1	X	X		X									X				Ferroactinolite
04NCGB013	2	1	X	X		X				X			X	X					

Sample	Structural-Lith. Zone	Number of T-Sections	Qtz	Pl	Kfs	Bt	Ms	Chl	Grt	St	And	Ky	Sil	Fib	Amp	Gr	Ilm	Rt	Other
04NCGB018A	2	1	X	X		X			X										
04NCGB023	1b	2	X	X		X			X				X						
04NCGB030A	3	1	X	X	X	X													Zr, Ap
04NCGB035B	4	1	X	X	X	X	X	X	X								X		epidote, apatite
04NCGB036B	4	1	X	X		X	X												
04NCGB036A	4	1	X	X		X	X	X											
04NCGB037(5)	4	1	X	X		X	X	X											

Sample	Structural-Lith. Zone	Number of T-Sections	Qtz	Pl	Kfs	Bt	Ms	Chl	Grt	St	And	Ky	Sil	Fib	Amp	Gr	Ilm	Rt	Other
04NCGB044A	4	1	X	X		X			X										
04NCGB044B	4	1	X	X		X			X										
04NCGB044C	4	1	X	X		X		X	X										
04NCGB044D	4	1	X	X		X			X										
04NCGB044E1	4	1	X	X															pseudotachylyte
04NCGB044E2	4	1	X	X															pseudotachylyte
04NCGB044F	4	1	X	X		X		X	X			X							epidote
04NCGB044G	4	1	X	X															hematite; gouge
04NCGB044H	4	1	X	X		X		X									X		
04NCGB048	4	1	X	X		X													1-2% opaques
04NCGB049	4	2	X	X		X													Zircon (abundant)

Sample	Textures
03NCGB124a	Weak foliation defined by mica. Ms appears primary. Medium grained.
03NCGB124b	Medium-grained equigranular phenocrysts. Bt is primary, but Ms appears secondary. Contains interstitial myrmekite and granophyre. Looks like main phase of Kbgg.
03NCGB126	Labyrinth Mountain granodiorite. Preserves abundant granophyre, myrmekite and complexly zoned Pl cystals. Ms is minor and is likely secondary: common around the margins of Bt grains.
03NCGB130b	Amphibolite. Evidence for inclusions in garnet at acute angle to external foliation defined by hornblende; foliation deflected around garnet porphyroblasts.
03NCGB133	Granodiorite near SW margin of Labyrinth pluton. Characterized by large, lobate Qtz crystals with visible subgrains and sweeping extinction, smaller euhedral to subhedral Pl crystals, less common Kfs, interstitial myrmekite and granophyre and biotite with apatite and zirocn inclusions.
03NCGB134	Coarse grained. Insterstitial granophyre is common.
03NCGB138c	NRMG schist. Minor Ms associated with Bt.
03NCGB138b	Schist NRMG. Polished for microprobe analyses (spatially between Kbgg and sample 03NC143, which contains garnets with Ca sector zoning). Ky, St and Grt are subhedral; St is far more abundant than Ky. Fibrolite appears syn- to post- foliation development. Grt porphyroblasts are relatively unincluded; foliation defined by biotite is deflected around Grt porphyroblasts; Qtz-Pl strain shadows lie on the low-stress sides of the porphyroblasts. Ky and St lie within the dominant foliation.
03NCGB138a	NRMG schist. Abundant euhedral 1-5 mm St with twinned pairs. Bt foliation deflected around St porphyroblasts, which are roughly aligned with foliation. Euhedral 5 mm Grt porphyroblasts. Grt both overgrows foliated Bt band along central axis and deflects parallel Bt layers along edges: syn-tectonic.

Sample	Textures
03NCGB142	NRMG intrusive dike/sill. Weakly foliated Bt + Ms + Chl. Chl replacing Bt.
03NCGB143	Schist NRMG. Grt Sm-Nd geochronology sample. Mineralogy appears fairly simple--few phases. Structure is significant: 5-7 mm euhedral-subhedral deep red/purple garnet porphyroblasts are characterized by Bt strain caps and Qtz strain shadows. Internal inclusion-defined foliation in almost perpendicular to external foliation in many garnets. Internal Grt textures show no discontinuity in core-rim growth. Neither is there obvious evidence for rotation during garnet growth; thus, fabric development postdates most, if not all, garnet growth.
03NCGB144	Chiwaukum Schist raft in Kbgg pluton (SE body). Bt-defined mm-scale gneissic folding. Small 1-2 mm Grt porphyroblasts are included and preserve some earlier foliation: pre- to syn-tectonic Grt growth. Looks like CS folding, partial tranposition and grain size. Is this style armored by crystallized Kbgg, so as not to experience the late-stage intense fabric development of neighboring NRMG?
03NCGB147	Chiwaukum Schist. This sample preserves a more pervasive schistosity with no evident folding and a coarser grain size. Grt and St both largely predate development of this pervasive Bt defined foliation: Strain caps and shadows accompany large 1-3 mm St porphyroblasts, which are oriented both parallel to and nearly perpendicular to the foliation. One such St porphyroblast is almost entirely included within a 4 mm Grt and is perpendicular to the foliation.
03NCGB148	Chiwaukum Schist. Abundant St, pre- to syn-kinematic. Strongly developed coarse foliation.
03NCGB149	Chiwaukum Schist. Alternating millimeter-scale Qtz-Pl bands and Bt-rich bands (S1) are isoclinally folded. Bt cleavage is axial planar and defines S2. 1-2 mm Grt porphyroblasts preserve S1 inclusion patterns, nearly perpendicular to S2 cleavage, which is deflected around Grt porphyroblasts. These observations corroborate hand-sample field observations suggesting that the finer-grained CS is only partially transposed into the most recent ductile fabric. Compare to NRMG sample 03NC143.

Sample	Textures
03NCGB151	Chiwaukum Schist. Small 1-2 mm Grt porphyroblasts are euhedral and syn- to post- tectonic. Large 10+ mm St porphyroblasts and St aggregates oriented roughly axial-planar parallel to mm-scale gneissic folding appear to be in disequilibrium, with large portions replaced by Bt+Qtz+Pl+Ms. Several areas contain abundant fibrolite.
03NCGB152	Chiwaukum schist with large 5-8 mm pseudomorphs of St+Ky+Bt+Ms+Fib+Qtz after And. Chiastolite cross visible. 0.5 mm Grt porphyroblasts are found in matrix; Ky is found as radial blades in And pseudomorph; Fib overgrows Bt and Qtz outside of pseudomorph.
03NCGB156	Coarser Qtz +Pl+Ms non-foliated dike cross-cuts foliated Bt schist.
03NCGB158	Schist raft. Tourmaline inclusions in Grt. Ky appears as inclusion in Grt rims but is absent in cores. Grt porphyroblasts > 10 mm. Large >2 mm Ky is less well foliated than Bt.
03NCHS19a	Schist raft. Foliation defined by strongly aligned Bt and aligned Ky. Bt foliation wraps around Grt porphyroblasts, indicating at least some foliation development post-dated Grt growth. Strain shadows are composed predominantly of quartz. Non-foliated thicker bands of equigranular-interlobate quartz divide foliated finer-grained Bt-Qtz bands. Larger quartz shows subgrain boundaries. St in association with Grt and Bt indicates stability in peak assemblage. Grt chosen for Sm-Nd geochronology is 6-8 mm, glassy pink, subhedral, and contains up to 20% inclusions. In thin section, these inclusions are anhedral and acicular Qtz (75%), subhedral Ky, St, opaques, with very minor Bt and Ms.
03NCHS20	Schist raft. Smaller 1-2 mm Grt porphyroblasts are variably subhedral to anhedral. Bt wrapping quartz and anhedral Grt suggest resorption at some stage during petrogenesis. No aluminumsilicates visible.
04NCGB003A	Amphibolite in schist raft. Ferroactinolite (pale and elongate)
04NCGB013	Chiwaukum Schist. Contains fibrolite mantled prismatic Sil in gneissic folds with St porphyroblasts.

Sample	Textures
04NCGB018B	Amphibolite layer in Chiwaukum Schist.
04NCGB018A	Garnet coronas in layer (sill?) of foliated Qtz+Pl+Bt. Abundant Pl surrounding very included small 1-2 mm Grt porphyroblasts.
04NCGB023	Garnetite in CS raft in MS. Almost exclusively large Grt and large prismatic Sil. Very little Qtz.
04NCGB030A	Granodiorite, Labyrinth Mountain pluton. Characterized by large, lobate Qtz crystals with visible subgrains and sweeping extinction, smaller euhedral to subhedral Pl crystals, less common Kfs, interstitial myrmekite and granophyre and biotite with inclusions of Zr and Ap.
04NCGB035B	0.2-0.4 mm brittle fractures are filled with epidote, Qtz and Pl and cross-cut both Bt-rich foliated zone and Qtz-Pl nonfoliated zone at high angles. Abundant < 1 mm garnets have subhedral rims and absent or heavily included cores.

Sample	Textures
04NCGB044A	Grt Bt schist, strongly foliated Bt. Pre- to syn- tectonic Grt porphyroblast growth.
04NCGB044B	Grt Bt schist, strongly foliated Bt. Pre- to syn- tectonic Grt porphyroblast growth.
04NCGB044C	Schist in Minotaur Lake FZ. Strongly foliated; microfaults offset Bt foliation; microfaults show reduced Qtz grain size and Chl.
04NCGB044D	Schist in Minotaur Lake FZ. Strongly foliated. 3 mm Grt porphyroblast contains oblique inclusion alignment (Si), while Se forms strain cap and shadow.
04NCGB044E1	Pseudotachylyte with angular Qtz, Pl and epidote alteration mineral fragments.
04NCGB044E2	Pseudotachylyte with angular Qtz, Pl and epidote alteration mineral fragments.
04NCGB044F	Strongly foliated thin bands of deformed Epidote+Chl and fragmented small Grt alternating with apparently recystallized layers of inequigranular interlobate Qtz+Pl. Subgrains visible in Qtz; grains are elongate parallel to foliation. 1-2 mm fault zones containing randomly oriented epidote (85%) +Qtz +Pl crosscut and offset foliation.
04NCGB044G	Discrete cataclastic fault gouge bands; some offset by microfaults.
04NCGB044H	Strongly foliated thin layers of epidote+Bt+Chl between thicker bands of polygonal to interlobate Qtz+Pl.
04NCGB048	Discrete foliated biotite-rich domains alternate with more coarse-grained Qtz bands. Biotite alignment is oblique to gneissosity.
04NCGB049	Bt schist in NRMG just NE of Minotaur Lake Fault. Strongly foliated. No kinematic indicators. Abundant zircon.

EPILOGUE

As a simple ball of twine led Theseus out of the labyrinth after slaying the Minotaur, so with the record of rocks and minerals we retrace the tectonic history of Labyrinth Mountain under the watchful eye of Jove Peak. Aegeus need not throw himself into the sea today, however, for we have remembered to fly the white flag.

G.R.B.